UNIVERSITÄT OSNABRÜCK

Repairing the Breach:

Uncovering ER-dependent Membrane Repair during Mycobacterial Infection

Dissertation

submitted to the Department of Biology/Chemistry of the
University of Osnabrück, Germany

to obtain the degree '*Doctor Rerum Naturalium*' (Dr. rer. nat.)

presented by

Aby Anand

Born in Thiruvananthapuram, India

Osnabrück, September 2023

Referees:

Main examiner: **Prof. Dr. Caroline Barisch**

Head of the Host-Microbe Interactome Division
Research Center Borstel (FZB)
Centre for Structural Systems Biology (CSSB), Hamburg

Second examiner: **Prof. Dr. Michael Hensel**

University of Osnabrück
Department of Biology/Chemistry
Microbiology Division
CellNanOs - Center of Cellular Nanoanalytics Osnabrück

Other members of
the thesis committee: **Prof. Dr. Christian Kost**

University of Osnabrück
Department of Biology/Chemistry
Ecology Division

Dr. Rainer Kurre

University of Osnabrück
Department of Biology/Chemistry
iBiOs - Integrated Bioimaging Facility Osnabrück
CellNanOs - Center of Cellular Nanoanalytics Osnabrück

To my mom............

TABLE OF CONTENTS

LIST OF PUBLICATIONS AND MANUSCRIPTS

This cumulative thesis contains the following publications and manuscripts.

FRANZKOCH, R., **ANAND, A.**, BREITSPRECHER, L., PSATHAKI, O. E. & BARISCH, C. 2023. Resolving exit strategies of mycobacteria by combining high-pressure freezing with 3D-correlative light and electron microscopy. *bioRxiv*, 2023.04.24.538041. (under revision @*Mol Micro*)

ANAND, A., MAZUR, A.-C., ROSELL-AREVALO, P., FRANZKOCH, R., BREITSPRECHER, L., LISTIAN, S. A., HÜTTEL, S. V., MÜLLER, D., SCHÄFER, D. G., VORMITTAG, S., HILBI, H., MANIAK, M., GUTIERREZ, M. G. & BARISCH, C. 2023. ER-dependent membrane repair of mycobacteria-induced vacuole damage. *bioRxiv*, 2023.04.17.537276. (in press @*mbio*)

ZUSAMMENFASSUNG

Tuberkulose ist eine der tödlichsten Infektionskrankheiten. Der Erreger, *Mykobacterium tuberculosis*, hat verschiedene Strategien entwickelt, um im Inneren von Makrophagen zu überleben. Beispielsweise beschädigt *M. tuberculosis* die Membranen der Wirtszelle, um die Toxizität im endolysosomalen Raum zu verringern und die *Mykobacterium*-enthaltende Vakuole („*Mycobacterium-containing vacuole*"; MCV) zu verlassen. Läsionen an der MCV Membran rufen Reparaturmechanismen der Wirtsmembran hervor, um lysosomale und proteolytische Funktionen wiederherzustellen und das Ausbrechen der Bakterien ins Zytosol zu verhindern. Kürzlich wurde ein ER-abhängiger Reparaturmechanismus für beschädigte Lysosomen beschrieben, der durch Lipid-Transfer Proteine der Familie der Oxysterol bindenden Proteine (OSBP) realisiert wird. Um die zugrundeliegenden molekularen Mechanismen während Mykobakterieninfektionen aufzudecken, habe ich das *Dictyostelium discoideum*/ *M. marinum* System verwendet. Zusammen mit der Elektronenmikroskopieeinrichtung etablierte ich im ersten Teil dieser Arbeit die Wechselwirkungen zwischen Zellorganellen und der zytosolischen Translokation von Mykobakterien in *D. discoideum* eine 3D-HPF/FS-CLEM *Pipeline*. Diese Technik ist sehr aussagekräftig, konserviert Membranen in nahezu nativem Zustand und bietet eine fast atomare axiale Auflösung. Der zweite Teil dieser Arbeit beschäftigt sich mit der Bildung und Funktion des ER-abhängigen Reparaturweges während Mykobakterieninfektionen. Hierbei fand ich heraus, dass das ER-Golgi-Protein OSBP8 sowohl an der MCV als auch an zytosolischen Mykobakterien relokalisiert. Interessanterweise ist dieser Vorgang abhängig vom mykobakteriellen Typ-VII Sekretionssystem ESX-1 und möglicherweise auch von MCV-Membranschäden. Durch fortschrittliche, bildgebende Verfahren wurde festgestellt, dass gerissene MCV Membranen ER-Tubuli rekrutieren, auf denen OSBP8 lokalisiert ist. Durch die Untersuchung der funktionellen Auswirkungen dieser ER-MCV-Kontaktpunkte stellte sich herauswurde festgestellt, dass der Verlust von OSBP8 zu einer Hyperakkumulation von phosphatidylinositol 4-phosphat (PI4P) auf der MCV und Lysosomen führt, während die Sterin-Akkumulation leicht reduziert ist. Es wurde auch eine verringerte lysosomale Ansäuerung und proteolytische Aktivität in OSBP8-Knockout-Zellen beobachtet, was vermutlich das Wachstum der Mykobakterien fördert. In Kollaboration, wurde bei Infektionen mit *M. tuberculosis* beobachtet, dass das ER-Golgi-Protein OSBP in menschlichen Makrophagen in einer ESX-1-abhängigen Weise an intrazelluläre Mykobakterien relokalisiert. Zusammenfassend zeigen diese Ergebnisse, dass die ER-abhängige Membranreparatur zur Wirtsresistenz gegen intrazelluläre Krankheitserreger wie *M. tuberculosis* beiträgt.

SUMMARY

Tuberculosis is one of the top deadliest infectious diseases. Its causative agent, *Mycobacterium tuberculosis*, employs numerous strategies to survive and persist in macrophages. It induces membrane damage to reduce the endolysosomal toxicity and to exit the *Mycobacterium*-containing vacuole (MCV). Lesions in the MCV trigger host membrane repair machineries that restore its function and prevent the escape of bacteria. Recently, an ER-dependent repair of damaged lysosomes that is fostered by lipid transfer proteins of the oxysterol binding protein (OSBP) family was described. However, these membrane damage-repair events and especially the role of this pathway during *M. tuberculosis* infection are largely unexplored. To reveal the underlying molecular mechanisms, I employed the *Dictyostelium discoideum*/ *M. marinum* system. In the first part of this thesis, I established 3D-HPF/FS-CLEM together with the electron microscopy facility. This technique is robust, preserves membranes in their utmost native state and provides near-atomic axial resolution. Importantly, it allows envisioning organelle interactions and exit events of mycobacteria in *D. discoideum*. In the second part of this thesis, I uncovered the formation and function of ER-dependent repair pathway during mycobacterial infection. I found that the ER-Golgi protein OSBP8 re-localizes to the MCV as well as to cytosolic mycobacteria. Strikingly, the mobilisation of OSBP8 is dependent on the presence of the mycobacterial type VII secretion system ESX-1 and presumably on MCV damage. Using 3D-HPF/FS-CLEM and other advanced imaging approaches, I observed that ruptured MCVs recruit ER-tubules containing OSBP8 in its close proximity. Exploring the functional implications of ER-MCV contact sites revealed that depletion of OSBP8 leads to hyperaccumulation of phosphatidylinositol 4-phosphate PI4P on the MCV/lysosomes suggesting OSBP8 balances PI4P on damaged membranes. In addition to this, sterol accumulation in the MCV was slightly reduced. Next, by employing fluorescent probes I observed decreased lysosomal acidification and proteolytic activity in the OSBP8 knockout cells, which promoted mycobacterial growth. Conversely, I observed a growth restriction of mycobacteria in cells overexpressing OSBP8. Next, the conservation of the ER-dependent repair pathway in *M. tuberculosis* infected macrophages was tested. Remarkably, in agreement to OSBP8 mobilisation, the ER-Golgi protein OSBP re-localized to intracellular mycobacteria in human macrophages in an ESX-1-dependent manner. Taken together, these findings provide the evidence the ER-dependent membrane repair contributes to host resistance against intracellular pathogens including *M. tuberculosis*.

1. INTRODUCTION

1.1. How *Mycobacterium tuberculosis* manipulates the endolysosomal system in professional phagocytes

The human body is continuously exposed to microbes. They are eliminated among others by a fine-tuned mechanism called phagocytosis. It is a form of endocytosis that mediates the uptake of particles ≥ 500 nm in diameter (Pauwels et al., 2017). Macrophages, dendritic cells, monocytes and neutrophils are categorized as professional phagocytes, being critical for the innate immune responses (Uribe-Querol and Rosales, 2017, Ravichandran and Lorenz, 2007, Nguyen and Yates, 2021). For the efficient detection and killing of invading pathogens, these cells are equipped with a repertoire of phagocytic receptors. They carry pattern-recognition receptors, opsonic receptors and receptors for apoptotic cells on their surfaces that function in a coordinated fashion (Lee et al., 2020). In addition, phagocytosis bridges innate immunity to adaptive immunity through the antigen presentation ability of these specialized cells.

Phagocytosis is tightly regulated in a spatiotemporal manner. It has three distinct stages: (i) initiation, (ii) maturation and (iii) fusion with lysosomes (Fig. 1.1). Phosphoinositide phospholipids confer identity to the phagosomes at different stages. Briefly, following detection of the microbe, pseudopods that are rich in phosphatidylinositol 4,5-biphosphate ($PI(4,5)P_2$) are formed for engulfment (Saharan and Kamat, 2023). This involves remodeling and rearrangement of the actin cytoskeleton. Subsequently, $PI(4,5)P_2$ is turned over to phosphatidylinositol 3,4,5-triphosphate ($PI(3,4,5)P_3$) promoting scission of the phagosomes from the plasma membrane (Schlam et al., 2015). The nascent phagosomes immediately undergo progressive maturation. This is achieved through transient fusion-fission events with early and late endocytic organelles referred to as the 'kiss and run mechanism' (Fountain et al., 2021, Desjardins, 1995). The immediate fusion of the nascent phagosomes with early endosomes acquires Rab5 that recruits the class III PI3-kinase vacuolar protein-sorting 34 (Vps34). When Vps34 generates phosphatidylinositol 3-phosphate (PI3P) on early phagosomes (Marcelić et al., 2022), PI3P and Rab5 are required for the recruitment of early endosome antigen 1 (EEA1) that mediates the subsequent fusion events. In addition, the vacuolar H^+-ATPase is recruited to early phagosomes to acidify its lumen (Flannagan et al., 2012). Eventually, early phagosomes fuse with phosphatidylinositol 4-phosphate (PI4P)-enriched late endosomes to form late phagosomes (Fig. 1.1). PI4P is generated by PI4-kinase 2a (PI4K2A) (Henmi et al., 2016) and it plays a role in homotypic fusion and vacuole sorting (HOPS) complex recruitment (Bröcker et al., 2012). Besides PI4P, late phagosomes accumulate phosphatidylinositol 3,5-biphosphate ($PI(3,5)P_2$) that is synthesized by the 1-PI3P-5-kinase (PIKfyve) (Kim et al., 2014, Vines et al., 2023). Subsequently, Rab7 replaces

Rab5 and recruits lysosome-associated membrane proteins 1 and 2 (LAMP1 and LAMP2) (Huynh et al., 2007). Rab7 is critical for the fusion of lysosomes with late phagosomes to produce phagolysosomes. Lysosomes contain several acid hydrolases that degrade proteins, lipids and carbohydrates. These fusion events lead to an increasingly acidic (from pH 6.5 to 4.5) environment due to the progressive enrichment of vacuolar H^+-ATPase. Consequently, phagolysosomes have full microbicidal capacity (Fig. 1.1).
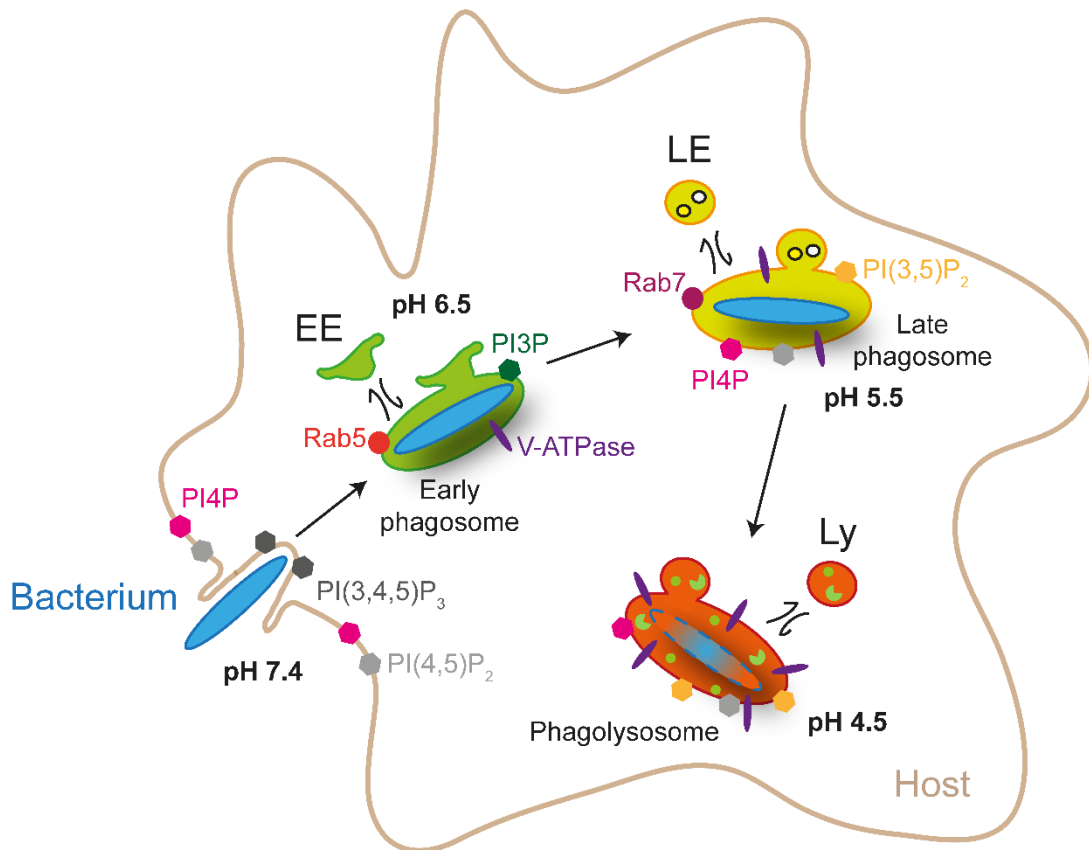
FIG 1.1 The phagocytic pathway in macrophages. Upon uptake, the bacterium resides in a phagosome. The phagosome matures progressively by fusion and fission events with early (EE) and late (LE) endosomes. Maturation involves a specific PIP signature and recruitment of Rab5 and Rab7. Finally, lysosomes (Ly) merge with late phagosome to generate the degradative compartment called the phagolysosome. Green Pac-Men and circles indicate lysosomal enzymes and ions, respectively. PIP: phosphatidylinositol phosphate.

The phagocytic pathway is a prerequisite in macrophages to function as the first line of defense against pathogens. However, certain bacterial pathogens, including *Mycobacterium tuberculosis*, developed a master plan to counteract with different stages of phagosomal maturation.

M. tuberculosis is an obligate intracellular pathogen that causes tuberculosis, one of the top infectious diseases with 1.6 million deaths in 2021 worldwide (Global Tuberculosis Report 2022, WHO). The air-borne pathogen infects alveolar macrophages in the lungs and is remarkably successful in suppressing innate immune responses (Chandra et al., 2022). Shortly after phagocytosis, *M. tuberculosis* resides in an intracellular niche termed *Mycobacterium*-containing vacuole (MCV). In the MCV, *M. tuberculosis* employs multiple virulence factors to rewire the endolysosomal route (Fig. 1.2). Fratti *et al.* and Vergne *et al.* showed that *M. tuberculosis* arrests MCV maturation by accumulating Rab5 and inhibiting Rab7 recruitment (Fratti et al., 2001, Vergne et al., 2004). On the contrary, recently it was shown that the MCV acquires late endosomal markers and initially follows a conventional maturation pathway, including the Rab5 to Rab7 transition (Schnettger et al., 2017).
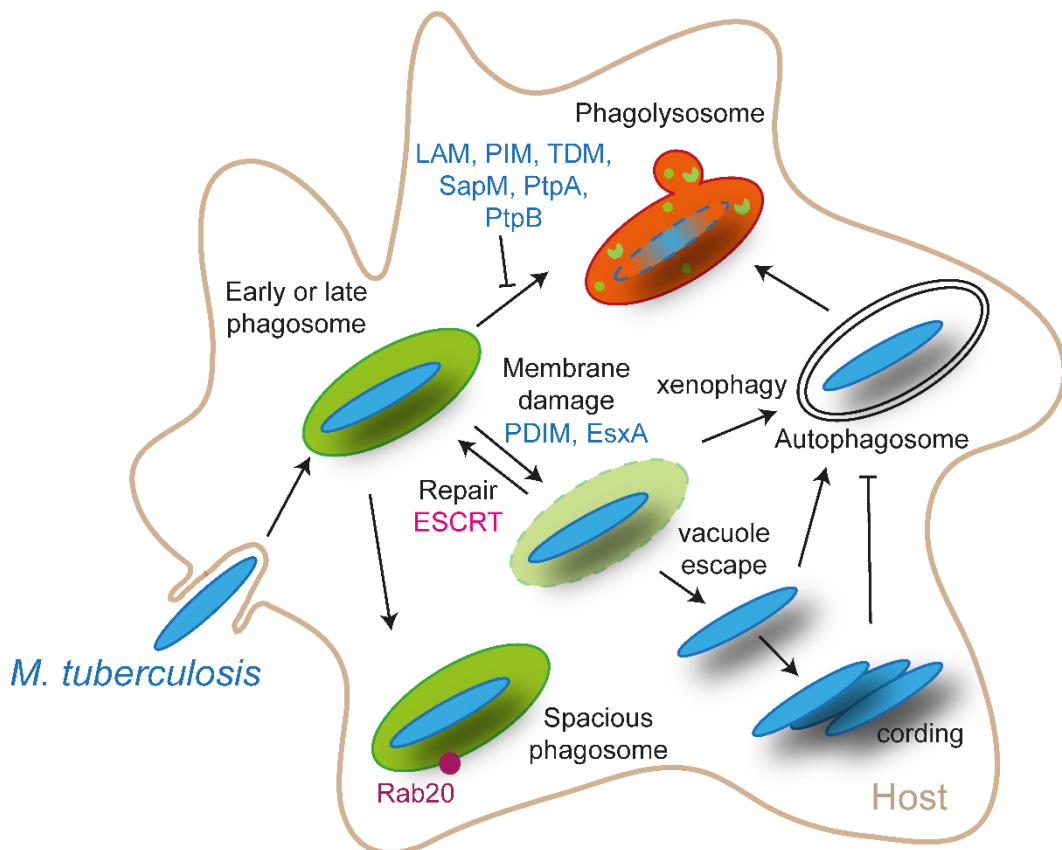
FIG 1.2 Rewiring of the phagocytic pathway by *M. tuberculosis.* Mycobacterial cell wall lipids and secreted phosphatases block phagosome maturation by inhibiting lysosomal fusion. Alternatively, *M. tuberculosis* transforms the phagosome into a spacious compartment or induce membrane damage. PDIM promotes the membranolytic activity of EsxA to gain access to the cytosol. Membrane damage triggers repair pathways. Cytosolic *M. tuberculosis* is detected by xenophagy that fuses with lysosomes. To evade xenophagy, *M. tuberculosis* exhibits cording. Mycobacterial effectors are indicated in blue and host components in magenta.

Alternatively, it recruits Rab20 to transform the MCV into a spacious phagosome (Schnettger et al., 2017). In addition, the mycobacterial secreted phosphatases interfere with MCV maturation by disrupting the PIP pattern and modulate MCV-lysosomal fusion (Koliwer-Brandl et al., 2019, Vaughn and Abu Kwaik, 2021). There are three known phosphatases, protein tyrosine phosphatase A (PtpA), PtpB and secreted acid phosphatase (SapM). Besides inhibiting MCV acidification by binding to subunit H of the vacuolar H^+-ATPase (Wong et al., 2011), PtpA binds to Vps33B to block endo-lysosome fusion (Galmes et al., 2015). PtpB exhibits multi-specific phosphatase activity, however, its *in vivo* function remains unclear (Beresford et al., 2007, Chatterjee, 2023). SapM blocks the MCV fusion with late endosomes by hydrolyzing PI3P (Vaughn and Abu Kwaik, 2021, Vergne et al., 2005).

Besides phosphatases, few mycobacterial lipids such as phosphatidylinositol mannoside (PIM), lipoarabinomannan (LAM) and trehalose-6, 6- dimycolate (TDM) also play a role in blocking MCV maturation (Fig. 1.2). While PIM and TDM blocks fusion events (Vergne et al., 2004, Indrigo et al., 2003), LAM inhibits the recruitment of EEA1 (Fratti et al., 2001). In addition to these factors, *M. tuberculosis* inflicts MCV membrane damage to escape killing and for the transition into the cytosol.

1.2. How *M. tuberculosis* escapes its vacuole and the consequences of infection

For decades, it was believed that the MCV is the exclusive niche for *M. tuberculosis* (Armstrong and Hart, 1971). However, subsequent studies based on electron microscopy (Myrvik et al., 1984) as well as tomographic reconstructions (van der Wel et al., 2007) provided the evidence that *M. tuberculosis* escapes from the MCV to the cytosol. To this end, *M. tuberculosis* has five type VII secretion systems (T7SS) called ESX1-5. Among them, ESX-1, ESX-3 and ESX-5 play a role in pathogenesis. ESX-3 is essential for acquiring zinc and iron (Serafini et al., 2013, Serafini et al., 2009, Siegrist et al., 2014) whereas ESX-5 secretes virulence proteins from the PE and PEE family (Bottai et al., 2012). Notably, ESX-1 is the first and extensively studied secretion system. Pioneering works from Simone *et al.* demonstrated that ESX-1 is required for the cytosolic translocation of *M. tuberculosis* (Simeone et al., 2012, Simeone et al., 2015). It is encoded by the region of difference 1 (RD1) locus which includes also the genes for the peptides early secreted antigenic target 1 (EsxA, 6 kDa) and culture filtrate protein 10 (EsxB, 10 kDa) (Sørensen et al., 1995). Although they are secreted as a heterodimer (Renshaw et al., 2005), EsxA dissociates from EsxB and incorporates into membranes at low pH (de Jonge et al., 2007). Despite studies on liposomes suggesting a pore forming activity, its biological relevance remains elusive (Augenstreich and Briken, 2020). However, EsxA is believed to be the key player for membrane damage and MCV exit of

M. tuberculosis (van der Wel et al., 2007). In line with that, deletion of RD1 leads to attenuated intracellular *M. tuberculosis* suggesting its requirement for virulence and dissemination (Gao et al., 2004). Recently, the mycobacterial lipid, phthiocerol dimycoserosate (PDIM), was identified to enhance the efficiency of EsxA (Fig. 1.2) (Augenstreich et al., 2017, Lerner et al., 2018). Following its insertion into the host membrane, PDIM forms a conical shape within the membrane bilayer. This affects the organization of the membrane and may lead to membrane curvatures that enhance the membanolytic activity of EsxA (Augenstreich et al., 2019, Cooke and Deserno, 2006, Augenstreich et al., 2020). Besides facilitating the cytosolic localization of the bacteria, MCV damage causes leakage of ion gradients and a rise in pH (Bussi and Gutierrez, 2019).

To keep the bacteria inside the MCV and to restore the gradients, the host recruits repair machineries. However, the dynamic processes of vacuole rupture and host repair during *M. tuberculosis* infection are poorly characterized (Bussi and Gutierrez, 2019).

Once exposed to the cytosol, *M. tuberculosis* is recognized by host defense mechanisms such as the xenophagy, a selective form of autophagy against pathogens (Fig. 1.2). Xenophagy restricts intracellular growth of *M. tuberculosis* (Aylan et al., 2023, Gutierrez et al., 2004). However, *M. tuberculosis* employs PE-PGRS proteins (Strong et al., 2020, Saini et al., 2016) and eventually induces a cording phenotype (Lerner et al., 2020) to protect the bacteria from autophagy recognition in the cytosol (Fig. 1.2). Additionally, the bacteria induce cell death and exit the host to disseminate into neighboring cells (Sun et al., 2015, Amaral et al., 2019, Quigley et al., 2017, Srinivasan et al., 2016).

Although direct studies of *M. tuberculosis* are critical to understand the underlying molecular mechanisms during infection, work with *M. tuberculosis* is challenging and has risk. For these reasons, model systems have gained importance to study the virulence and pathogenesis of *M. tuberculosis*.

1.3. *Dictyostelium discoideum*/ *M. marinum* system as a model system to study *M. tuberculosis* pathogenicity

D. discoideum is a soil dwelling amoeba that feeds on bacteria by phagocytosis. Its 34 Mb haploid genome has been fully sequenced (Eichinger et al., 2005, Chisholm et al., 2006) and annotated (http://www.dictybase.org). However, axenic (AX) strains of *D. discoideum* are isolates that grow in liquid medium (Watts and Ashworth, 1970), allowing easy cultivation in a laboratory environment. In addition, genetic manipulations such as the expression of reporter plasmids or generation of knockins or knockouts by homologous recombination are relatively

easy in *D. discoideum* (Veltman et al., 2009a, Veltman et al., 2009b, Paschke et al., 2018, Paschke et al., 2019, Wiegand et al., 2011, Mukai et al., 2016). Importantly, many cell-autonomous defense mechanisms, including the phagocytic pathway and xenophagy, are well conserved between *D. discoideum* and macrophages (Boulais et al., 2010, Gotthardt et al., 2002, Tábara and Escalante, 2016). The maturation of phagosomes in *D. discoideum* follows a similar route like in macrophages (Fig. 1.1). Additionally, its doubling time (8 - 12 hrs) is shorter compared to macrophages (~ 20 hrs). For these reasons, *D. discoideum* is a versatile surrogate for macrophages to study the pathogenesis of various intracellular bacterial pathogens such as *Salmonella*, *Legionella* and mycobacteria such as *M. marinum* (Steinert, 2011, Cardenal-Muñoz et al., 2017b, Weber et al., 2014, Jia et al., 2009).

M. marinum is typically found in aquatic environments and infects aquatic vertebrates (Decostere et al., 2004). Although humans are not its natural host, it causes superficial skin infections. *M. marinum* generates granuloma-like lesions in its host similar to those induced by *M. tuberculosis* in humans. Additionally, *M. marinum* is a close relative of *M. tuberculosis,* both phylogenetically and genetically, sharing 85 % nucleotide identity (Stinear et al., 2008). Importantly, many virulence factors are conserved, such as the T7SSs. Even though closely related, *M. marinum* belongs to biosafety level (BSL) 2 whereas *M. tuberculosis* is BSL 3. In addition, it has a shorter doubling time (6 - 8 hrs) in contrast to *M. tuberculosis* (20 - 24 hrs). These advantages serve *M. marinum* as a model pathogen for *M. tuberculosis*.

The establishment of the *D. discoideum/ M. marinum* system has provided many insights into the molecular mechanisms involved in *M. tuberculosis* pathogenesis (Hagedorn and Soldati, 2007, Solomon et al., 2003). The infection course of *M. marinum* in *D. discoideum* is similar to *M. tuberculosis* in macrophages (illustrated below)*.* Shortly after uptake, *M. marinum* resides in the MCV that is permissive for replication (Hagedorn and Soldati, 2007). The secreted phosphatases (PtpA, PtpB and SapM) modify the PIP pattern of the MCV and inhibit phagosome maturation (Koliwer-Brandl et al., 2019). In addition, *M. marinum* blocks the recruitment of vacuolar H^+-ATPase at later infection stages (Hagedorn and Soldati, 2007). The MCV of *M. marinum* accumulates post-lysosomal markers for example, the copper transporter p80 and the ammonium transporter AmtA (Kirsten et al., 2008, Hagedorn and Soldati, 2007). Moreover, *M. marinum* also induces ESX-1-dependent MCV damage to lower ion gradients (Hanna et al., 2021) and to translocate to the cytosol (Hagedorn and Soldati, 2007). *M. marinum* lacking the T7SS ESX-1 (ΔRD1) does not induce MCV damage and is attenuated in *D. discoideum* (Hagedorn and Soldati, 2007, Cardenal-Muñoz et al., 2017a). Membrane lesions and cytosolic exposure of *M. marinum* are recognized by ubiquitin and recruit the

autophagy machinery (Atg8a/LC3^{+}) (Cardenal-Muñoz et al., 2017a). Eventually, *M. marinum* may exit the cell through ejectosomes, F-actin-dense structures that facilitate dissemination without host cell lysis (Hagedorn et al., 2009).

Interestingly, while cytosolic translocation and cell exit occur at later infection stages, *M. marinum* induces membrane damage already at early stages. However, the bacteria escape to the cytosol once the intrinsic repair machineries of the host are overwhelmed by cumulative damage.

1.4. How membrane repair pathways act against vacuole damage inflicted by mycobacteria

Although the bilayer of vacuole serves as a potential barrier, mycobacteria induce damage to translocate to the cytosol. The host responds to these lesions by activating membrane repair machineries belonging to the endosomal sorting complex required for transport (ESCRT)- and sphingomyelin (SM)-dependent repair (Fig. 1.3A-B) (Barisch et al., 2023). The molecular mechanisms of membrane repair have been extensively studied by employing L-leucyl-L-leucine methyl ester (LLOMe) to induce sterile damage. LLOMe is converted by dipeptidyl peptidase-I into a polymer with membranolytic properties in lysosomes (Thiele and Lipsky, 1990a, Thiele and Lipsky, 1990b).
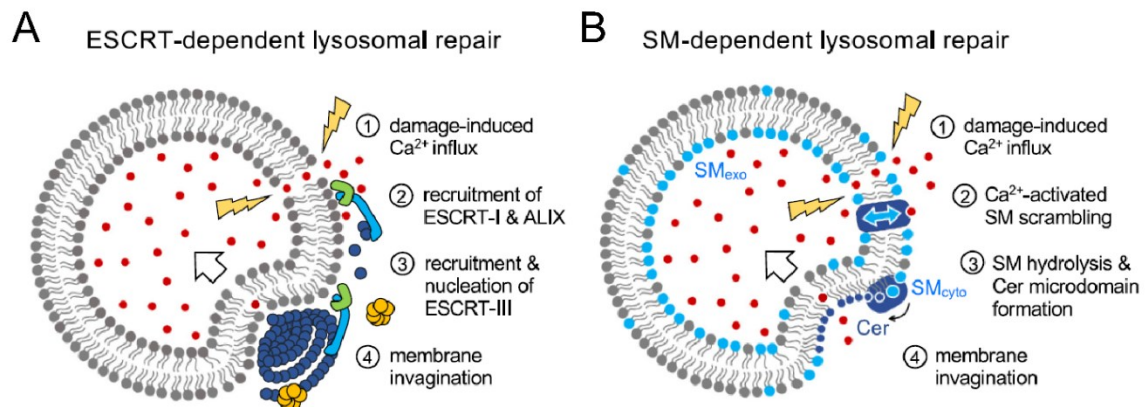
FIG 1.3 Membrane repair pathways fostering recovery of damaged lysosomes. (A) Model depicting ESCRT-dependent repair. (B) Model depicting SM-dependent repair. Sterile damage of lysosomes causes leakage of Ca^{2+} that triggers downstream events in the respective pathways (see text for details). Modified from (Barisch et al., 2023).

The ESCRT machinery repairs lesions $\leq$ 100 nm in diameter (Barisch et al., 2023). Briefly, Ca^{2+} leakage upon sterile damage triggers the accumulation of ESCRT-I subunit TSG101 and its interaction partner ALIX. Subsequently, ESCRT-III components including the AAA ATPase

VPS4 that facilitate inward budding and sealing of the affected region are recruited. This leads to the formation of intraluminal vesicles (ILVs) in which ubiquitinated membrane proteins are sorted (Pfitzner et al., 2020, Vietri et al., 2020, Katzmann et al., 2003).

Although ESCRT-independent, SM-dependent repair is also activated by the influx of Ca^{2+} into the cytosol (Niekamp et al., 2022). This leads to SM scrambling from the luminal to outer leaflet of the lysosomes by a Ca^{2+}-dependent scramblase. SM is then converted to ceramide by neutral SMase resulting in curved microdomains. It was hypothesized that these invaginations bud off into the lumen and become ILVs. In line with this, lack of neutral SMase impairs membrane integrity and affects lysosomal repair (Niekamp et al., 2022).

Intriguingly, both repair pathways respond to mycobacterial infection. ESCRT-III components (Chmp4) are recruited to MCVs containing *M. tuberculosis* in macrophages (Mittal et al., 2018). However, mycobacteria oppose ESCRT recruitment through EsxG and EsxH, secreted by the T7SS ESX-3 (Mittal et al., 2018). Notably in *D. discoideum, M. marinum* infection leads to the recruitment of ESCRT-I (Tsg101) and ESCRT-III (Vps32 and Vps4) components (López-Jiménez et al., 2018). Additionally, autophagy proteins accumulate at the MCV (Cardenal-Muñoz et al., 2017a). However, lack of ESCRT-I and autophagy (*atg1*) lead to more cytosolic mycobacteria and enhanced growth (López-Jiménez et al., 2018). In analogy to this, in macrophages, autophagy restricts *M. tuberculosis* growth (Aylan et al., 2023). Altogether, this suggests that ESCRT- and autophagy-dependent machineries are critical for MCV repair. While ESCRT components repair tiny lesions, the autophagy machinery seals larger ruptures by patching the membrane. In the case of SM-dependent repair, SM is exposed to the cytosolic leaflet upon infection with *M. marinum* in an ESX-1-dependent manner in macrophages (Niekamp et al., 2022).

ESCRT- and SM-dependent repair are proposed to remove the wounded area by ILV formation. How lipids are supplied to restore the membrane composition and integrity of lysosomes remains poorly understood.

1.5. ER-dependent repair as a novel membrane repair pathway

Recent proteomic (Tan and Finkel, 2022) and lipidomic (Radulovic et al., 2022) analyses of damaged lysosomes revealed a repair pathway that includes lipid transport, i.e. ER-dependent repair pathway (Fig. 1.4). Briefly, sterile lysosomal damage causes Ca^{2+} influx into the cytosol. This recruits PI4K2A that generates PI4P on lysosomes. PI4P enrichment induces ER-lysosome membrane contact sites (MCS) that mediate non-vesicular transport of lipids by lipid transfer proteins (LTPs). Subsequently, LTPs of the oxysterol binding protein (OSBP) family
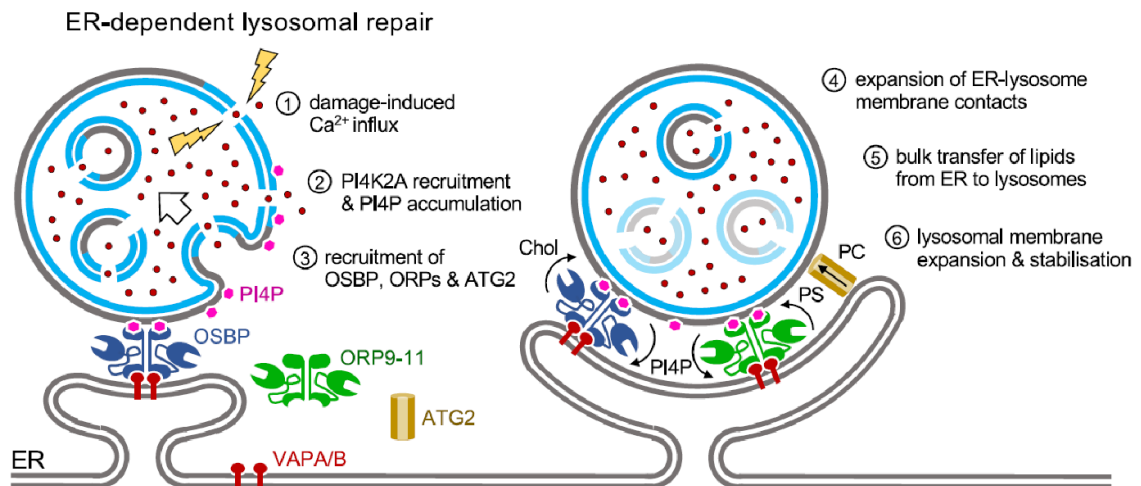
FIG 1.4 A novel membrane repair pathway. Model depicting ER-dependent repair (see text for details). Modified from (Barisch et al., 2023).

(OSBP, ORP9, ORP10 and ORP11) are recruited to these sites (detailed below). OSBPs interact with the vesicle-associated membrane protein (VAMP)-associated protein (VAP) on the ER and bind to the lysosomes via their PH-domain in order to form a tether between both organelles. This interaction fosters PI4P transport from the lysosome to the ER in exchange for cholesterol or PS. Recruitment of LTPs and lipid shuttling leads to the expansion of the ER-contact site on damaged lysosome (Tan and Finkel, 2022). In addition, ATG2, another LTP, is also mobilised to ER-lysosome MCS (Tan and Finkel, 2022). ATG2 acts as a tunnel that facilitates bulk transfer of lipids (Tan and Finkel, 2022). Cells lacking various components involved in ER-dependent repair fail to restore lysosomal membrane integrity. This affects cell viability probably due to the leakage of lysosomal content, which is hazardous to cells (Radulovic et al., 2022). Whether ER-dependent repair plays a role in the battle against intracellular pathogens remains to be explored (Barisch et al., 2023).

1.6. Membrane contact sites and conservation of oxysterol binding proteins in *D. discoideum*

MCS are zones where membranes of two organelles are in close proximity (10 - 80 nm) without undergoing fusion (Scorrano et al., 2019). These nanocompartments accommodate proteins that function as tethers, transporters or regulators facilitating lipid/ion exchange. Examples are LTPs from the OSBP family that mediate non-vesicular sterol transport. Other sterol transporters for example, the Steroidogenic Acute Regulatory Protein-related Lipid Transfer Domain (STARD) family and the Aster-domain containing family (He et al., 2023). OSBP and OSBP-related proteins (ORPs) are highly conserved in eukaryotes (Olkkonen, 2015). Twelve members (OSBP and ORP1-11) have been identified in *Homo sapiens* and seven OSBP-

9

homologues (Osh1-7) in *Saccharomyces cerevisiae* (Raychaudhuri and Prinz, 2010, Lehto et al., 2001). Typically, OSBPs consist of the following motifs or domains: (i) pleckstrin homology (PH) domain to bind to PI4P or other PIPs, (ii) ankyrin repeats that facilitate protein-protein interactions, (iii) two phenylalanines in an acidic tract (FFAT) motif to tether to VAP and the (iv) OSBP-related domain (ORD) for lipid transport (Nakatsu and Kawasaki, 2021). However, short versions also exist in *H. sapiens* and *S. cerevisiae* that exclusively contain the ORD.

Among the twelve members in *H. sapiens*, OSBP was first identified (Raychaudhuri and Prinz, 2010). OSBP localizes at the ER-Golgi MCS (Fig. 1.5A) and fosters PI4P/cholesterol exchange that is driven by a PI4P gradient (Mesmin et al., 2017). Briefly, PI4K2A synthesizes PI4P at the Golgi (Wang et al., 2003). PI4P is transported by OSBP via the ORD from the Golgi to the ER. Here, PI4P is hydrolyzed by the PI4P-phosphatase Sac1 and this generates a PI4P gradient between the organelles. The hydrolysis of PI4P allows OSBP to transfer cholesterol against the concentration gradient (Mesmin et al., 2013, Antonny et al., 2018).
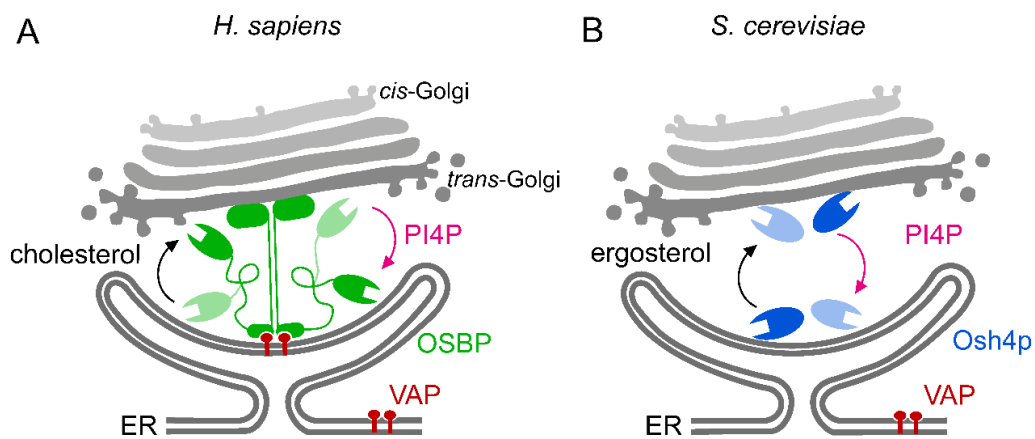
FIG 1.5 Lipid exchange at ER-Golgi contact sites. (A) Model illustrating cholesterol/PI4P shuttling mediated by *H. sapiens* OSBP. (B) Model depicting ergosterol/PI4P exchange fostered by *S. cerevisiae* Osh4. See text for details.

On the contrary, there are few evidences on the subcellular localizations of short versions of OSBPs in *H. sapiens* (Weber-Boyvat et al., 2015, Aw et al., 2020, Johansson et al., 2003). However, their functions and their mechanism of membrane targeting are poorly understood. *S. cerevisiae* Osh4 is so far the best-characterized short version. In analogy to OSBP, Osh4 localizes at the ER-Golgi MCS (Fig. 1.5B) and facilitates PI4P/ergosterol exchange that is driven by a PI4P gradient (de Saint-Jean et al., 2011).

OSBPs are conserved in *D. discoideum*. However, they are poorly characterized. The *D. discoideum* genome encodes twelve OSBPs (OSBP1-12) which are all short and mainly contain the ORD (Anand et al., 2023). A comparison of *D. discoideum* OSBP sequences with

short counterparts in *H. sapiens* and *S. cerevisiae* revealed that OSBP8, 9, and 11 are closely related (Vormittag et al., 2023). Interestingly, OSBP8 and OSBP11 are involved in ER-contact site formation during *Legionella* infection (Vormittag et al., 2023). However, their subcellular localizations and role at MCS during mycobacterial infection remain to be investigated.

1.7. *D. discoideum* as an ideal host to monitor lipid dynamics during mycobacterial infection

A key requirement to investigate MCS is visualization. The most common method to study organelle interactions is live cell imaging (Rizzuto et al., 1998). Although light microscopy (LM) is suitable for monitoring dynamics, the spatiotemporal resolution is limited as MCS falls below its diffraction limit (Scorrano et al., 2019). Super resolution microscopy techniques, such as lattice light sheet microscopy (Chen et al., 2014) or expansion microscopy (Wassie et al., 2019), have high spatial and temporal resolution to monitor the dynamics of these nanocompartments. However, the combination of LM with electron microscopy (EM), correlative light and electron microscopy (CLEM), allows to relate the subcellular information of LM to its ultrastructural detail. Other techniques to visualize MCS in a 3D perspective are electron tomography (de Brito and Scorrano, 2008) or focused ion beam scanning electron microscopy (FIB-SEM) (Wu et al., 2017). Importantly, advanced imaging methodologies have gained importance in the field of infection biology (Greenwood et al., 2019, Lerner et al., 2020, Kommnick et al., 2019).

To study MCS during mycobacterial infection, *D. discoideum* is an excellent and attractive organism suitable for live cell imaging (Arafah et al., 2013, Barisch et al., 2015a). The dynamics of lipid droplets (LDs) during mycobacterial infection has been extensively studied in *D. discoideum* (Barisch et al., 2015b) when compared to macrophages (Peyron et al., 2008, Singh et al., 2012). Briefly, LDs are ubiquitous organelles and consist of a hydrophobic core of cholesterol esters and triacylglycerols (TAGs). They are surrounded by a monolayer of phospholipids along with various proteins including perilipin (PLIN) and diacylglycerol acyltransferese 2 (Dgat2) (Mekonnen et al., 2021). Interestingly, PLIN and Dgat2 interact with cytosolic mycobacteria in *D. discoideum* (Barisch et al., 2015b, Barisch and Soldati, 2017). In addition to LDs, there are fluorescent reporters to monitor phosphoinositide (PI3P, PI(3,5)P$_2$, PI4P) signaling during phagocytosis (Koliwer-Brandl et al., 2019, Vines et al., 2023, Weber et al., 2014). Vacuolin, a homologue of flotillin, can be used to track lipid microdomains and as marker for the MCV during infection (Hagedorn and Soldati, 2007). Besides LM, TEM analyses showed an accumulation of intracytosolic lipid inclusions in *M. marinum* (Barisch and Soldati, 2017). Despite live cell imaging and TEM tools available in this system, correlative

methodologies are limited. However, FIB-SEM analysis of *M. marinum* infected *D. discoideum* revealed autophagosomes interacting with the MCV (López-Jiménez et al., 2018) and CLEM studies showed autophagy machinery interacting with ejectosomes (Gerstenmaier et al., 2015). Conventional EM sample preparation often induces artifacts due to dehydration whereas in case of FIB-SEM, milling destroys the sample (López-Jiménez and Mostowy, 2021). Collectively, a CLEM method that preserves the lipid bilayers in its native state in *D. discoideum* needs to be established.

2. SCOPE OF THE THESIS

M. tuberculosis is remarkably a successful pathogen and subverts the endolysosomal system in macrophages. In addition, it induces membrane damage to destroy the membrane potential and ion gradients as well as to translocate to the cytosol. In response to damage, host membrane repair machineries are recruited to restore the gradients and to prevent the vacuole escape. Previous studies in the *D. discoideum*/ *M. marinum* system revealed that the ESCRT- and autophagy-dependent repair pathways restrict vacuolar and cytosolic mycobacteria. However, recent work in mammalian cells revealed an ER-dependent repair of damaged lysosomes that is mediated by host lipid transfer proteins of the oxysterol binding protein (OSBP) family independent of ESCRT components. Whether ER-dependent repair is conserved in *D. discoideum* and what impact it has during mycobacterial infection are questions that remain to be explored. However, imaging tools to visualize these ER-contact sites in their near-native state are lacking at present. Therefore, the primary objective of this thesis was to provide insights into the significance of ER-vacuole contact sites during *M. marinum* infection, with an emphasis on developing a correlative workflow to monitor their morphology and studying their functional implications using knockouts in *D. discoideum*. To this end, the experiments were designed to accomplish the following goals:

   i. To establish a 3D-correlative imaging pipeline to visualize organelle interactions and to monitor exit events of mycobacteria.

   ii. To investigate whether ER-dependent repair plays a role during infection and to identify the OSBPs involved.

   iii. To uncover the function of ER-dependent repair pathway during infection.

   iv. To study the conservation of the mechanism in the macrophage/ *M. tuberculosis* system.

3. RESULTS

The results of my cumulative thesis will be presented in three parts. The first part focuses on the establishment of a correlative methodology to monitor mycobacterial exit events in *D. discoideum* and includes the manuscript under revision entitled "Resolving exit strategies of mycobacteria by combining high-pressure freezing with 3D-correlative light and electron microscopy". The second part describes a previously unknown mechanism of vacuole repair during mycobacterial infection and includes the accepted manuscript entitled "ER-dependent membrane repair of mycobacteria-induced vacuole damage". The third part is an extension of the second manuscript that includes unpublished data revealing the potential mechanism of OSBP8 mobilisation.

3.1.1. Resolving exit strategies of mycobacteria by combining high-pressure freezing with 3D-correlative light and electron microscopy

Authors

Rico Franzkoch[1, 2, 3,#], Aby Anand[2,4,#], Leonhard Breitsprecher[1,2,3], Olympia E. Psathaki[1,2,*], Caroline Barisch[2,4,5,6,7,*]

[#]These two authors contributed equally to the work.

Affiliations

[1]iBiOs–integrated Bioimaging Facility, University of Osnabrück, Osnabrück, Germany

[2]Center of Cellular Nanoanalytics, Osnabrück, Germany

[3]Division of Microbiology, Department of Biology, University of Osnabrück, Osnabrück, Germany

[4]Division of Molecular Infection Biology, Department of Biology, University of Osnabrück, Osnabrück, Germany

[5]Centre for Structural Systems Biology, Hamburg, Germany

[6]Research Center Borstel - Leibniz Lung Center (FZB), Borstel, Germany

[7]Department of Biology, University of Hamburg, Hamburg, Germany

*Corresponding authors:

Caroline.Barisch@uos.de – Tel: +49-541-969-7232
Katherina.Psathaki@uos.de – Tel: +49-541-969-7355

Running title: Imaging of vacuole escape by correlative microscopy

15

Abstract

The infection course of *Mycobacterium tuberculosis* is highly dynamic and comprises sequential stages that require damaging and crossing of several membranes to enable the translocation of the bacteria into the cytosol or their escape from the host. Many important breakthroughs such as the restriction of vacuolar and cytosolic mycobacteria by the autophagy pathway and the recruitment of sophisticated host repair machineries to the *Mycobacterium*-containing vacuole have been gained in the *Dictyostelium discoideum/ M. marinum* system. Despite the availability of well-established light and advanced electron microscopy techniques in this system, a correlative approach integrating both methods with near-native ultrastructural preservation is currently lacking.

This is most likely due to the low ability of *D. discoideum* to adhere to surfaces, which results in cell loss even after fixation. To address this problem, we improved the adhesion of cells and developed a straightforward and convenient workflow for 3D-correlative light and electron microscopy. This approach includes high-pressure freezing, which is an excellent technique for preserving membranes. Thus, our method allows to monitor the ultrastructural aspects of vacuole escape which is of central importance for the survival and dissemination of bacterial pathogens.

Introduction

Phagocytosis is a fundamental defence mechanism that triggers inflammatory and immunological responses and plays a crucial role in bridging innate and adaptive immunity against invading pathogens (Lim et al., 2017, Lee et al., 2020). Professional phagocytes such as macrophages and neutrophils use a variety of innate immunity strategies to identify and eliminate intruders within bacteria-containing phagosomes. However, some microbes have developed sophisticated strategies to overcome these processes. For example, *Mycobacterium tuberculosis*, the causative agent of tuberculosis, subverts this compartment into a proliferation-friendly niche while also damaging the membrane and rendering the phagosomal defences ineffective. The host, on the other hand, counteracts by recruiting various membrane repair pathways to the site of damage to retain *M. tuberculosis* inside the *Mycobacterium*-containing vacuole (MCV) (Barisch et al., 2023). When the damage overwhelms the repair machineries, *M. tuberculosis* translocates into the cytosol before exiting the cell (Bussi and Gutierrez, 2019).

We and others have pioneered the investigation of various membrane repair pathways such

16

as ESCRT- and autophagy- (López-Jiménez et al., 2018), as well as ER-dependent repair (Anand et al., 2023) in the *Dictyostelium discoideum*/ *M. marinum* model. Within this system, the sequential stages of the *M. tuberculosis* infection course such as (i) the initial stage when the bacteria remodel the phagosome, (ii) the vacuolar stage when replication begins, and (iii) vacuole exit as well as the cytosolic stage that precedes (iv) host cell exit, are conserved and are distinguishable with well-established markers (Figure 1) (Cardenal-Munoz et al., 2017). In *D. discoideum*, light microscopy (LM) of live cells has been increasingly important to study the course of infection due to it's high temporal and spatial resolution. For example, LM was used to generate time-lapse movies to monitor the escape of *M. marinum* via ejectosomes (Hagedorn et al., 2009), the spatiotemporal dynamics of Rab proteins at the MCV (Barisch et al., 2015a) and the re-distribution of lipid droplets during infection (Barisch et al., 2015b). Although LM is a powerful tool for observing dynamic processes, it does have limitations. For instance, it relies on selective labelling techniques, e.g. fluorescent proteins or dyes, to visualize subcellular structures or protein localization. Additionally, the relatively low resolution of LM and the absence of ultrastructural context makes it difficult to accurately identify the structures underlying the fluorescence signal. For several decades, transmission electron microscopy (TEM) has been used to unravel the ultrastructural architecture of various organelles. Unlike other techniques, TEM provides near-atomic spatial resolution and allows all subcellular components to be visualised simultaneously (Bozzola and Kuo, 2014). In the *D. discoideum*/ *M. marinum* model system, TEM protocols including chemical fixation were used to image ejectosomes (Hagedorn et al., 2009) and to monitor accumulation of intracytosolic lipid inclusions inside *M. marinum* (Barisch and Soldati, 2017). However, conventional sample preparation for TEM is known to induce artefacts such as cell shrinkage and extraction of cellular material which can drastically alter the ultrastructure of the sample (McDonald and Auer, 2006).

The combination of both imaging approaches as correlative light and electron microscopy (CLEM) overcomes the individual limitations and thus represents a robust tool that has recently gained increasing attention in the field of infection biology (Kommnick and Hensel, 2021, Weiner et al., 2016b, Lerner et al., 2020). Especially when investigating vacuole escape, reliable preservation and visualisation of the vacuolar membrane is of utmost importance. To overcome the induction of artefacts during sample preparation, high-pressure freezing (HPF) and freeze substitution (FS) were established already in the 1980s (Moor, 1987, Humbel and Müller, 1985). These techniques reduce the occurrence of artefacts and preserve membrane organization in a near native state (Vanhecke et al., 2008, Kaneko and Walther, 1995). HPF and FS are therefore essential for analysing the battlefield at the MCV including vacuole damage and escaping pathogens in their ultrastructural environment. However, an approach

that combines HPF and FS with CLEM has yet to be established for the *D. discoideum* system. This is very likely due to the fact that *D. discoideum* adhesion points are small, relatively weak and transient (Mijanović and Weber, 2022). Consequently, the ability of *D. discoideum* to adhere to surfaces is relatively low and is very likely the reason for the great loss of cells during HPF and FS. Adherence is critical for CLEM experiments since effective correlation requires the observation of the same cell using both, LM and TEM.

The three-dimensional organisation of a cell makes it difficult to detect membrane damage using traditional TEM, as it is limited to capturing two-dimensional sections. High-resolution 3D-EM including TEM-tomography has become an essential tool for accurately identifying membrane discontinuity. For instance, in a recent study, membrane rupture within mitochondria during apoptosis was elegantly shown using this approach (Ader et al., 2019).

Due to the lack of protocols that allow the visualisation of membrane rupture as well as vacuole escape of *M. marinum*, we developed a 3D-HPF/FS-CLEM workflow for the *D. discoideum/ M. marinum* system. To this end, we first improved substrate adhesion of *D. discoideum* before combining high resolution fluorescence microscopy, HPF and FS to preserve near-native ultrastructure for TEM tomography analysis. Our protocol provides a basis for studying exit events in *D. discoideum* and presents the first published HPF/FS-CLEM protocol for the *D. discoideum/ M. marinum* model system.

Results

Optimizing *D. discoideum* adherence and fixation for CLEM

D. discoideum adheres to surfaces via focal-like adhesions that resemble the ones from fibroblasts and other mammalian cells. While these points have been shown to be F-actin positive, *D. discoideum* cell-to-substrate adhesion includes the homologue of talin A and several integrin-like proteins (Mijanović and Weber, 2022, Kreitmeier et al., 1995, Cornillon et al., 2008). However, adhesion points in *D. discoideum* are characterized by their small size (< 10 % of cell size), fragility, and short lifespan (Wessels et al., 1994, Weber et al., 1995). Tapping the petri dish or pipetting media onto the cells typically results in cell detachment. Therefore, techniques like immunostaining or EM are challenging for adherent *D. discoideum* cells as the standard protocols involve many washing steps. To resolve this issue, we set out to optimize the cell-to-substrate adherence of *D. discoideum*. We took advantage of the fact that the attachment of cells is improved by enhancing their electrostatic interactions by treating surfaces with poly-l-lysine (PLL) (Mazia et al., 1975). Consequently, cell adherence with and without PLL treatment of sapphire discs, i.e. coverslips suitable for HPF was evaluated by LM before and after several washing steps. Without treatment, cells detached from large areas of the discs (Supplementary Figure S1), while PLL coating improved cell adherence. It should be

noted that PLL treatment has been observed to change the morphology of *D. discoideum* and also leads to cell death if exposed for a long time. Thus, we kept incubation times to a minimum of 15 min. However, despite the PLL coating, a high proportion of cells detached after HPF. This was improved when a strain expressing GFP-actin-binding domain (ABD) was used. These cells exhibit a high degree of adhesion and are challenging to detach during cell culture. Currently it is poorly understood how the expression of GFP-ABD improves adhesion,
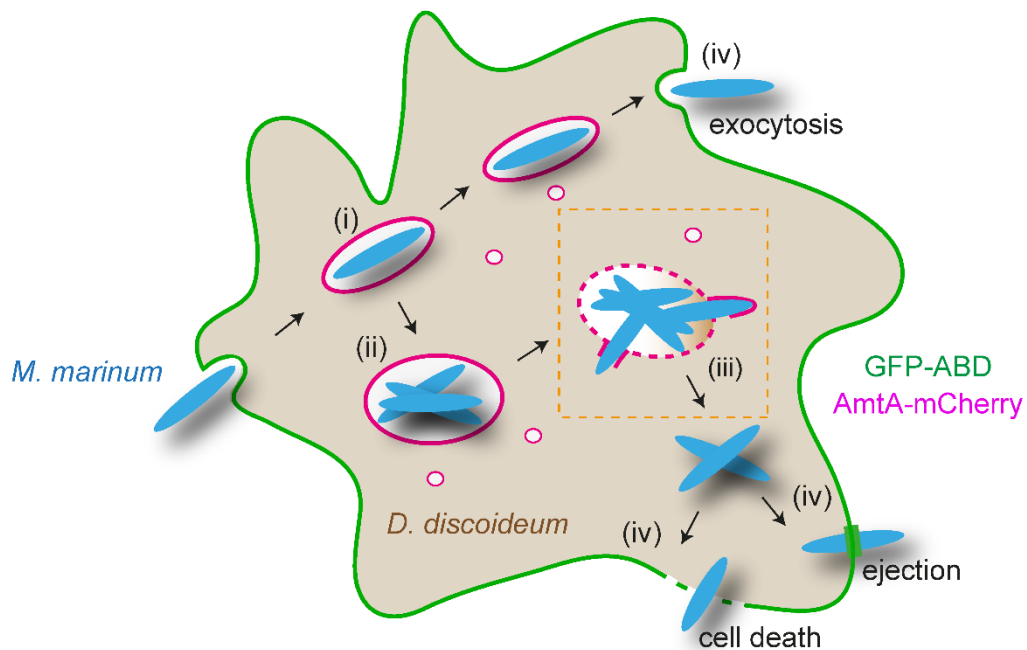

FIGURE 1 Scheme sketching the sequential infection stages of *M. marinum* in *D. discoideum*. Early after uptake, *M. marinum* resides in the MCV (i) and creates a friendly environment for its own replication by blocking phagosome maturation (ii). Cumulative damage at the MCV membrane leads to vacuole escape of the bacteria (iii). *M. marinum* exits *D. discoideum* either by exocytosis, ejection or upon host cell death (iv). The markers GFP-ABD (F-Actin, cell cortex) and AmtA-mCherry (endosomes and MCV) are suited to distinguish various infection stages. The orange box indicates the "infection stage of interest" that was investigated using the here described workflow.

however, this might be linked to the fact that foci enriched in F-actin are the anchorage points of traction forces in *D. discoideum* (Mijanović and Weber, 2022, Iwadate and Yumura, 2008). Thus, overexpression of GFP-ABD might increase adhesion by cross-linking the F-actin cytoskeleton. To rule out that this leads to artefacts, we performed an infection experiment in cells co-expressing AmtA-mCherry (Figure 2). AmtA is an ammonium transporter that labels all endosomes in *D. discoideum* (Uchikawa et al., 2011) and is a suitable marker for the MCV (Barisch et al., 2015b). While GFP-ABD enabled us to monitor MCVs at early infection stages and host cell exit by ejection (GFP-ABD[+]), AmtA-mCherry allows to visualise MCV membrane rupture and cytosolic bacteria (AmtA-mCherry[-]) (Figure 2). Importantly, the timing of sequential stages of the infection (Figure 1) appeared to be unaltered by the overexpression of both
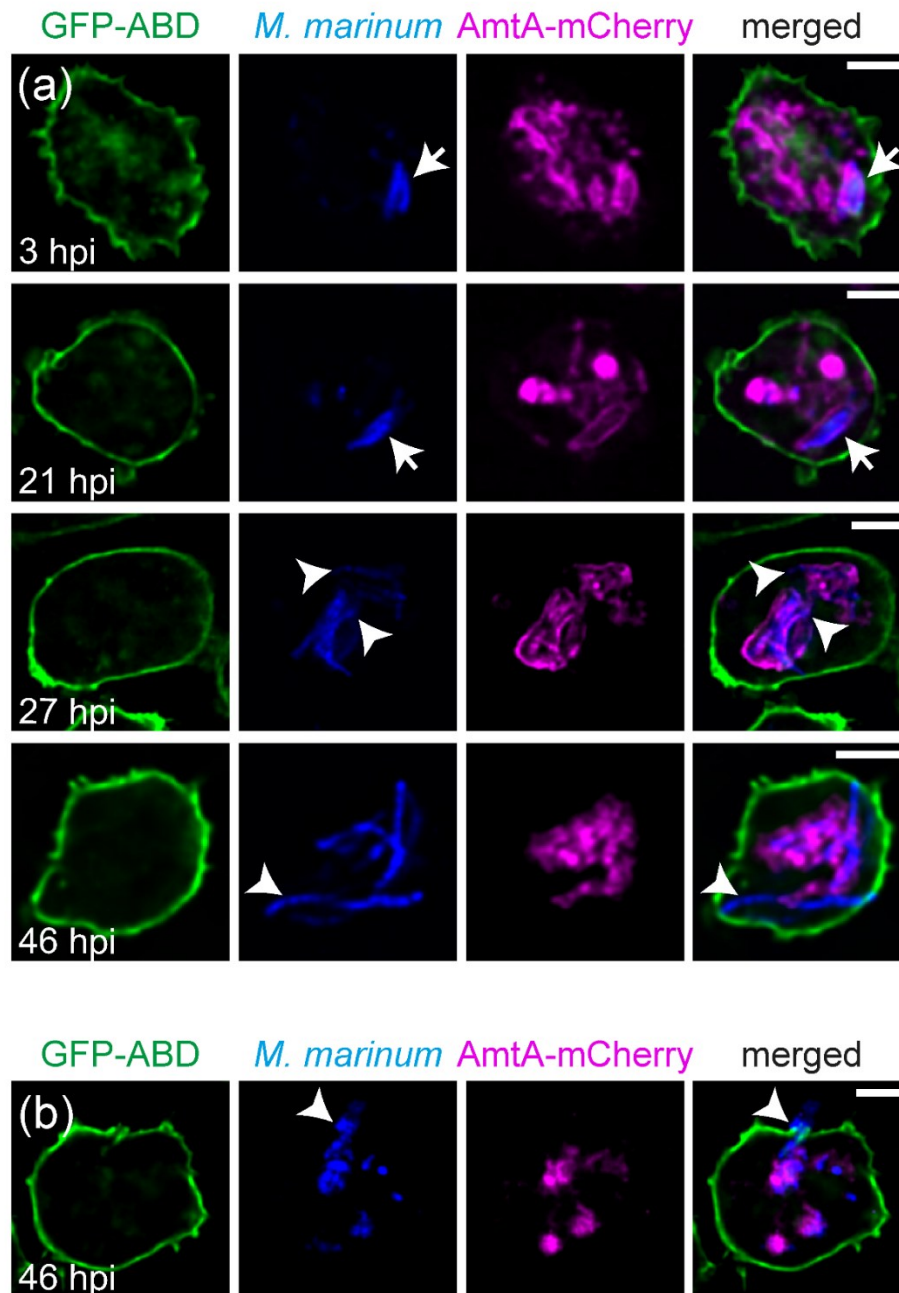
FIGURE 2 The infection course in cells overexpressing AmtA-mCherry and GFP-ABD. *D. discoideum* overexpressing both, GFP-ABD and AmtA-mCherry, were infected with eBFP-expressing *M. marinum*. At the indicated time points, cells were imaged live. Arrows label vacuolar mycobacteria, arrowheads point to either cytosolic mycobacteria in (a) or a bacterium that is exiting the host by ejection in (b). Scale bars, 5 μm.

proteins (Figure 2). In summary, treating sapphires with PLL as well as the overexpression of GFP-ABD significantly improved cell-to-substrate adherence of *D. discoideum* and did not impact on the infection course.

D. discoideum moves a lot and even escapes the imaging field (Barisch et al., 2015a). This

together with the extremely dynamic nature of its organelles including the MCV, and the time lag between LM and HPF makes the correlation very challenging. To address this, we first tested how different concentrations of the fixative glutaraldehyde (GA) affect cell shape by seeding *D. discoideum* on sapphire discs and transferring them into an ibidi 8-well dish for live imaging. Next, we carefully added double-concentrated fixative to the cells at final concentrations of 0.05 %, 0.1 % and 0.5 % GA and avoided laser exposure to reduce phototoxicity. This revealed that low concentrations of GA immobilised the cells, however their morphology still continued to change (Supplementary Figure S2a, Movie S1-4). In addition, we observed cells rounding up especially when incubated with 0.1 and 0.5 % GA. We applied a combination of 0.05 % GA and 3 % paraformaldehyde (PFA) which even lead to the subsequent shrinkage of cells (Movie S5). Finally, we discovered that dipping the cells grown on sapphires into medium containing 2% GA for a short exposure (~1 sec), followed by imaging in 0.5% GA effectively preserved the cell morphology for 30 minutes (Supplementary Figure S2a, b, Movie S4). Under these conditions we were able to locate the cells after fixation (Supplementary Figure S2b) and did not observe any interfering background signals (Supplementary Figure S2c). A beneficial side effect of the GA fixation was the improved cell adhesion which has already been demonstrated for *D. discoideum* (Koonce et al., 2020).

Design of a LM configuration for high numerical aperture oil immersion objectives

Initially, we imaged upright sapphire discs (3*0.05 mm) with cells on top in an ibidi 3-cm dish or 8-well slide. Focusing the cells with an inverted 63x or 40x oil immersion objective was difficult and the quality of the LM image was poor. We believe that this was caused by (i) the limited working distance of these objectives or by (ii) optical interferences of the bottom of the imaging slide and the sapphire disc.

Subsequently, we designed an imaging setup that is simple to install and was utilised to acquire LM images of exceptional quality with high NA oil immersion objectives. Figure 3a shows a schematic representation of the entire setup. First, a coordinate system was sputtered onto acid cleaned sapphire discs (3*0.16 mm) using a 20 nm thin layer of gold. Following that, a gold grid with a 2 mm aperture was attached on top of the sapphire disc using Loctite AA 350 to avoid crushing of the cells during the imaging process (Figure 3b). This glue has proven to be non-toxic to cells and is non-soluble in water or acetone (Brown et al., 2012). The assembly was UV-cured overnight in a Leica AFS2 and then coated with PLL. Cells were seeded on top of the sapphire disc with gold spacer at appropriate densities. We used extra thin 24 mm coverslips (130 - 160 µm) as a bottom for the construct, which was fitted into a custom-made holder onto the microscope stage and sealed with a rubber ring (Figure 3c). To
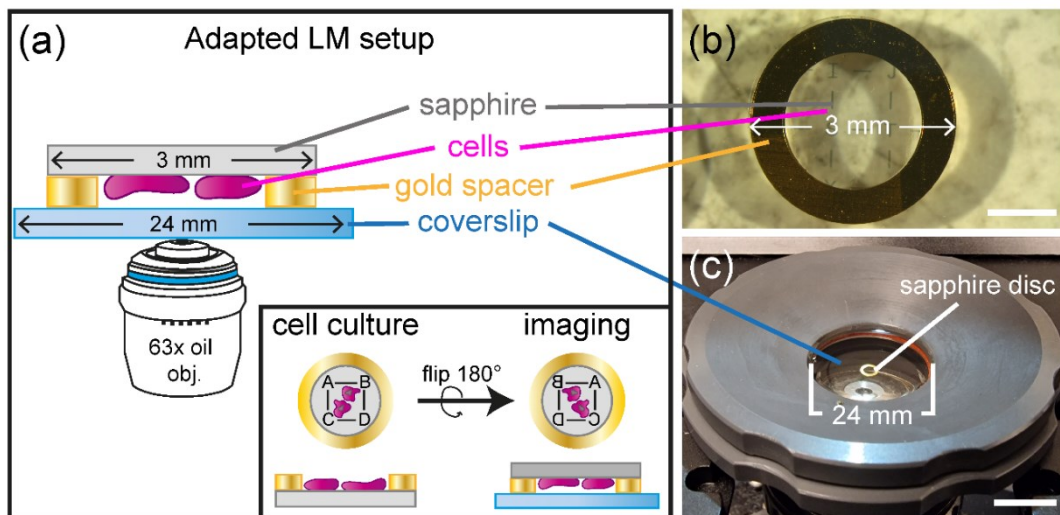
FIGURE 3 Light microscopy imaging setup for optimized z-resolution and correlative work flows. (a) Schematic representation of a 3 mm sapphire disc (grey) with gold spacer (yellow) and monolayer of cells (magenta) on a 24 mm coverslip facing the 63x NA 1.46 oil immersion objective. Rotation of the disc (as indicated in the inset) and application of the gold spacer allows reliable and reproducible focusing since the laser has to pass only through the coverslip. (b) Customization of the sapphire discs. Cells are seeded on sapphire discs with coordinate system until they form a monolayer of about 70% confluency. (c) Position of the sapphire discs on the stage. The sapphire discs are flipped and placed on a coverslip that is mounted with the help of a custom-made adaptor.

prevent cells from drying, 500 µl of Hl5c filtered medium containing 0.5 % GA were added. The sapphire disc was then flipped upside down and placed on the 24 mm coverslip, resulting in cells directly facing the objective (Figure 3a). This enabled high resolution LM imaging using the 63x 1.46 NA oil immersion lens.

Workflow of 3D-HPF/FS-CLEM of infected *D. discoideum*

The implementation of our improved cell adhesion and imaging protocols, combined with HPF and FS resulted in highly reproducible outcomes. Briefly, infected cells expressing GFP-ABD and AmtA-mCherry were seeded on PLL-coated sapphire discs. Prior to LM, the discs were dipped into 2% GA diluted in Hl5c filtered medium and transferred upside down with the cells facing the coverslip into the custom-made coverslip holder (Figure 3). Samples were screened for regions of interest (ROI) followed by an acquisition of a z-stack (Figure 4a) and a low resolution brightfield overview (Figure 4b). Following this protocol at least two positions were monitored on each sapphire disc. Directly after acquisition of the last image the sapphires were transferred into the HPF holder with the cells facing upwards (Figure 4c, i). The flat side
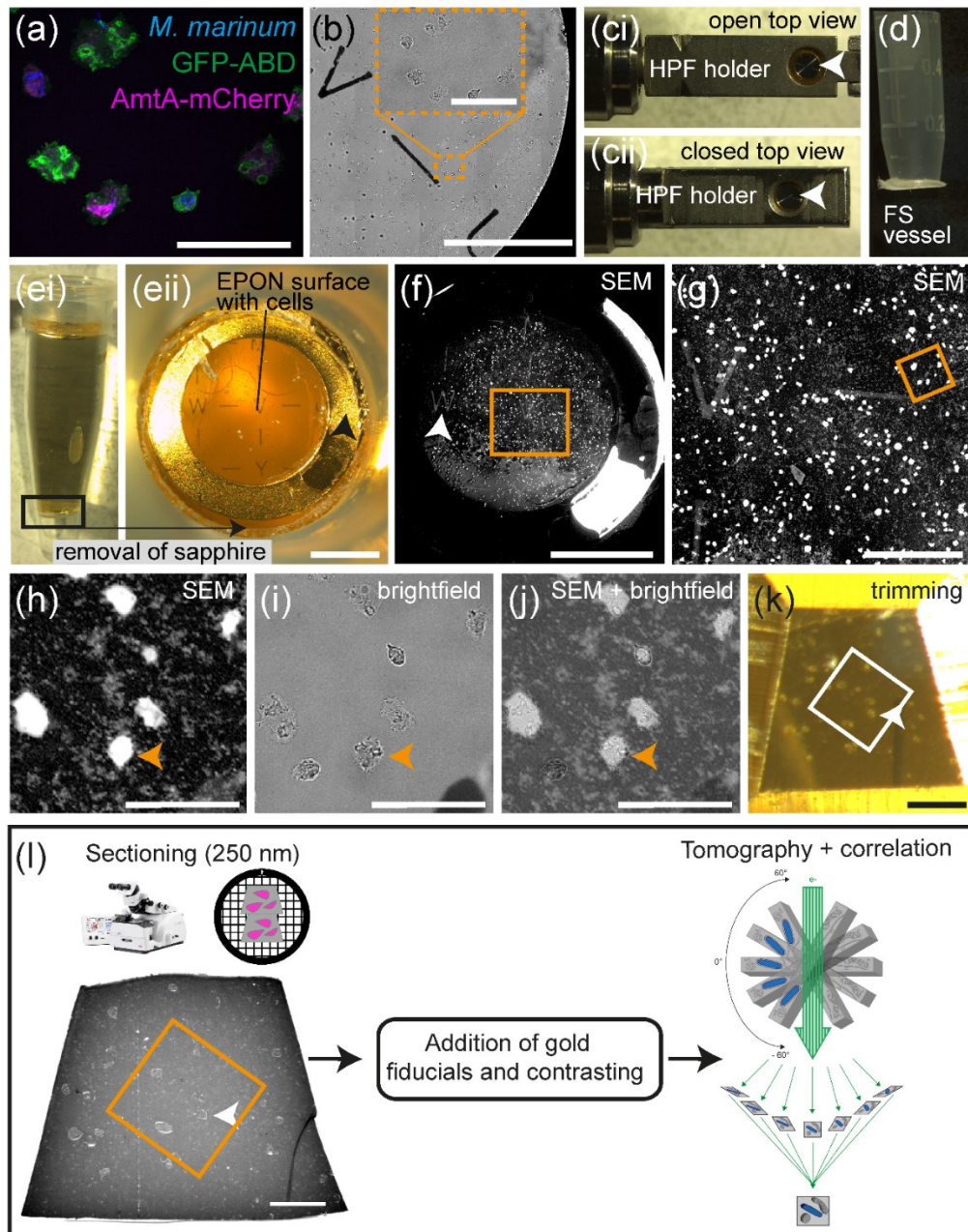
FIGURE 4 3D-HPF/FS-CLEM workflow. (a) Locating the cell of interest and fluorescence z-stack acquisition of fixed cells by SD microscopy using the 63x objective. (b) An overview is acquired using either the 25x oil immersion or 10x air objective to visualise the coordinates of the desired region (orange box). (c) Assembly of the sandwich consisting of a flat planchette dipped in 1-hexadecene and the sapphire with gold spacer and cells is assembled in the HPF-holder (i). With the redesigned carrier, the holder can be closed properly and HPF can be initiated (ii). (d) After HPF, sapphire discs are placed in a special vessel that facilitates storage in liquid nitrogen and their further processing. (e) Embedding of cells in a 0.2 ml tube that is filled with EPON 812 (i) and removal of the sapphire via heat shock which leaves the resin with cells, the gold spacer and the coordinates on top (ii, black arrowhead). (eii) Bottoms-up view of (ei). (f-j) Locating the cells of interest (orange arrowheads) by acquiring an overview using SEM in which the gold coordinates are easily visible (f, white arrowhead), zoom of orange box in f (g), zoom of orange box in g (h), bright field image of the SEM region shown

FIGURE 4 legend continued

in h (i) and its overlay (j). (k) Trimming of the ROI and sectioning of 250 nm thin sections using an ultramicrotome facilitated by the previously recorded LM and SEM images. Sections are then transferred onto copper grids. (l) Addition of gold fiducials and contrasting agents prior to tomogram acquisition and correlation. Arrowheads in (eii), (f), (h) - (l) indicate the cell of interest. White or orange boxes in (k) and (l) indicate the ROI. Scale bar, 50 µm in (a), (h), (i), (j); 500 µm in (b); 1 mm in (e; i, ii); 200 µm in (g) and (l); 100 µm in (k).

of a planchette was dipped into 1-hexadecene and added on top of the sapphire. Then the holder was closed and high pressure frozen (Figure 4c, ii). After HPF the samples were stored in specially designed vessels in liquid nitrogen. These vessels consisted of a 0.5 ml tube with cut-off top and bottom and were used from this point on during the whole FS and embedding procedure. To prevent samples from slipping through the bottom, while also allowing solutions to access the specimen, a fine piece of mesh was attached by slightly melting the end of the tube and pressing it onto the mesh (Figure 4d). This avoids problems that occur when samples are moved to fresh tubes for each step and turned out to be critical in preventing cells from detaching from the sapphires. The protocol for FS is described in Material and Methods. For final polymerization in EPON 812, sapphire discs with cells facing upwards were transferred into a 0.2 ml PCR tube which was then filled with resin (Figure 4e, i). Polymerized blocks were separated from the tubes with a razor blade. Excess resin on the top and sides of the sapphire was removed. By immersing the top of the block into liquid nitrogen and then touching the sapphire disc with a 50 °C warm razor blade, the disc was removed and the EPON surface with cells and coordinate system became visible (Figure 4e, ii). To facilitate trimming and initial correlation, images of the whole block-face were acquired in a scanning EM (SEM) at low vacuum mode (50 Pa) with high probe current (60 A) and voltage (30 kV) (Figure 4f, g). This revealed the gold imprint of the coordinate system on the surface of the EPON block (Figure 4g) and confirmed that the cells remained on the sapphire during the whole procedure thus making a first correlation possible (Figure 4h-j). In addition, this allowed precise targeting and trimming of the block to exclusively include the ROI (Figure 4k). Thin sections (250 nm) were prepared using an ultramicrotome and deposited on copper slot grids (Figure 4l). With the help of LM and SEM micrographs, the cell of interest was rapidly identified and relocated on the section (Figure 4k). After addition of 10 or 15 nm gold fiducials and contrasting with 3 % uranyl acetate for 30 min and 2 % lead citrate for 20 min correlative TEM tomograms with a tilt range from ± 60° were acquired (Figure 4l).

3D-HPF/FS-CLEM to monitor the ultrastructure of vacuolar escape of *M. marinum* in *D. discoideum*

To showcase the applicability of our developed 3D-HPF/FS-CLEM workflow, we set out to

resolve and correlate the ultrastructure of the MCV during vacuolar escape of *M. marinum* in *D. discoideum.* Cells co-expressing GFP-ABD and AmtA-mCherry were infected with eBFP-expressing bacteria and analysed at 24 hours post-infection (hpi) (Figure 5). During LM we partly observed absence of the AmtA-mCherry signal on the MCV indicating that there might be membrane rupture at the site of escape (Figure 5a, arrowheads). However, without the underlying ultrastructural information, this interpretation remains speculative. The previously
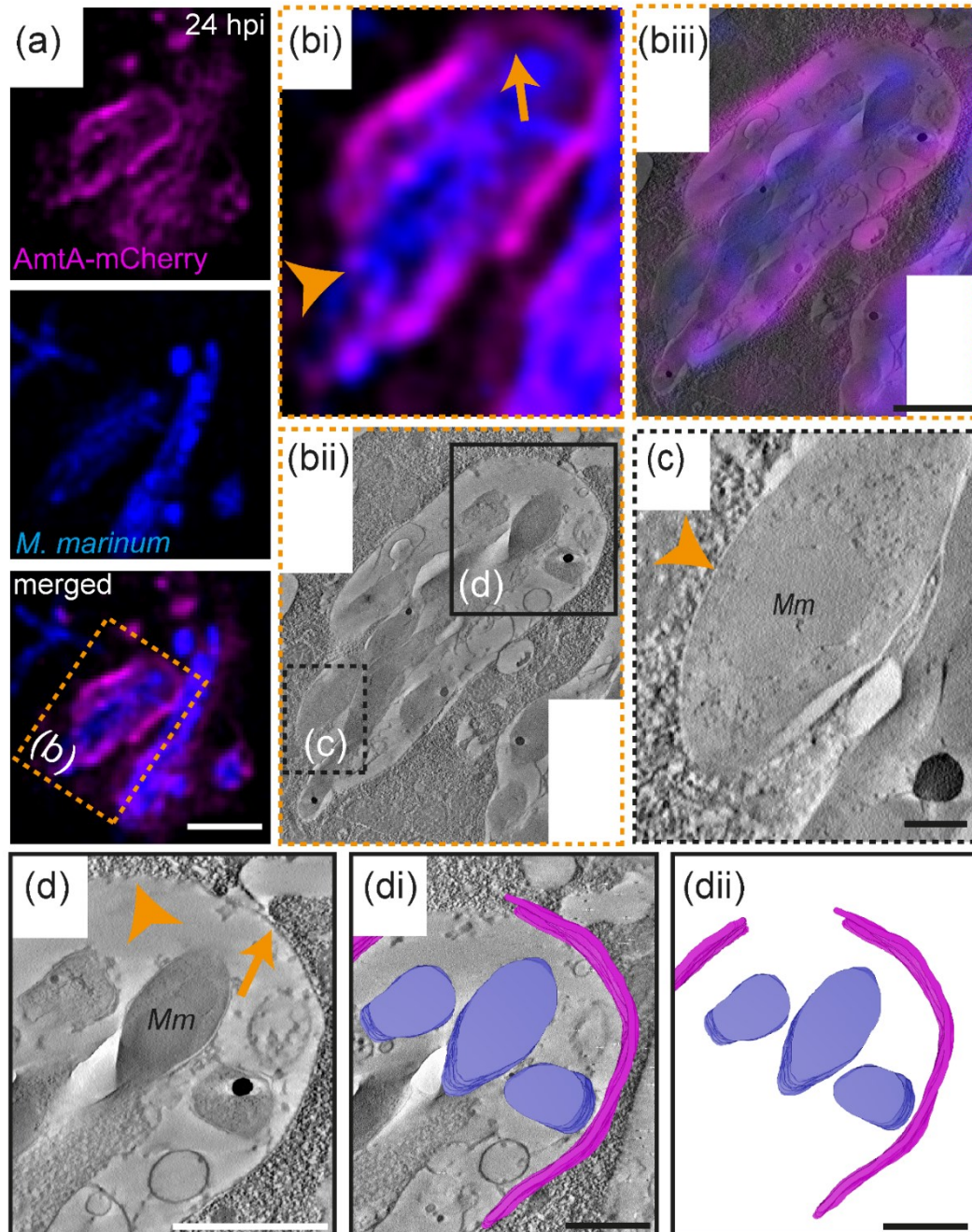

FIGURE 5 3D-HPF/FS-CLEM enables the visualisation of *M. marinum* exiting the MCV. (a) Fluorescence image showing the cytosolic translocation of *M. marinum.* (b) Correlation of the magnified LM image with the tomogram; (i) LM image showing membrane ruptures reflected by the loss of the AmtA-mCherry-signal (arrow: minor lesion, arrowhead: full rupture).

25

FIGURE 5 legend continued

(ii) Corresponding tomography slice. (iii) Overlay of both imaging modalities to identify possible exit events. (c-d) Higher magnification tomograms of the areas indicated in (bii) revealed bacterium that is fully cytosolic (c, arrowhead) and bacteria that are partially enclosed by the membrane of the MCV (arrow). (d) The gap in the MCV membrane correlates with the absence of the AmtA-mCherry-signal (arrowhead). (di, dii) This is supported by the segmentation showing a discontinuity of the MCV membrane throughout the whole tomogram. Blue: *M. marinum*, magenta: MCV membrane. *Mm*: *M. marinum*. Scale bar, 5 µm (a), 1 µm (b), 200 nm (c), 1 µm (d). Please see also Movie S6-S7.

described 3D-HPF/FS-CLEM workflow enables precise correlation of areas without AmtA-mCherry signal with high resolution tomography data (Figure 5b, Movie S6-7). This revealed one single MCV containing at the same time a large membrane rupture with partially cytosolic bacteria (Figure 5c), as well as a small membrane lesion in close proximity to vacuolar bacteria (Figure 5d). In conclusion, our approach enables the efficient correlation of LM and EM data, and consequently facilitates an accurate and comprehensive understanding of subcellular structures and dynamic processes such as vacuole escape.

Discussion

In this article we describe a robust 3D-HPF/FS-CLEM workflow that integrates LM, HPF, FS and TEM-tomography for studying exit events in the *D. discoideum*/ *M. marinum* model system. To this end, we created a unique LM setup which facilitates high resolution LM using high numerical aperture oil immersion lenses that is also compatible with live cell imaging (Figure 3, Supplementary Movies S1-5). However, because of the time delay of up to 1 min between acquisition of the last LM image and HPF, we decided to include a mild fixation step. This immobilises *D. discoideum* and allows precise correlation of LM and TEM-tomography. A system that allows even faster transfer of the sample to the HPF machine, was developed by Verkade in 2008. To this end, LM and HPF are carried out in the same holder (Verkade, 2008). Using this setup, time until cryo-fixation was reduced to up to four seconds (Brown et al., 2012). This configuration is only available from Leica which severely limits its use. Another comparable setup was recently presented by Heiligenstein *et al.* consisting of the HPM live µ high-pressure freezer in combination with the CryoCapsule (Heiligenstein et al., 2021). Here, the process from LM to cryo-fixation is completely automated and happens within 1.2 seconds. The recent advancements in holder and transfer systems underline the urgent need for new methodological approaches for sample carriers and preparation for CLEM including HPF. In this regard we established a method which does not require further equipment and allows precise correlation of ROIs monitored by LM (Figure 3-4). Nevertheless, there is a need for the development of systems that enable swift transfer between LM and HPF. Additional modifications of our method would include the design of an LM setup in which LM is directly

carried out through the bottom of the sapphire disc rather than through the coverslip. In this arrangement cells would be closer to the objective lens which resulting in higher-quality fluorescence images, however, construction and handling of such a system would be more challenging.

Key advantages of utilizing HPF and FS are near-native preservation of ultrastructure including membranes which present important barriers pathogens have to overcome (McDonald and Auer, 2006, Vanhecke et al., 2008, Kaneko and Walther, 1995). For the *D. discoideum/ M. marinum* model system only few CLEM approaches are published (Gerstenmaier et al., 2015, Malinovska et al., 2015). They all include conventional sample preparation for EM which may not accurately reflect the native membrane organization in the investigated specimens and complicates data interpretation. A general challenge for setting up CLEM with *D. discoideum* is the fact that these cells adhere only weakly to the substrate (Wessels et al., 1994, Weber et al., 1995). To overcome this, we used a strain expressing GPF-ABD, which enhances cell-substrate adhesion, combined with PLL coating of sapphire discs and mild GA fixation, which dramatically improved the success of the protocol. Coating substrates with PLL is a well-known method to improve adherence in cell culture and also provided excellent results for *D. discoideum* (Lombardi et al., 2008). Fixation with low concentrations of GA has been previously shown to promote cell attachment in *D. discoideum* and was suggested to be used when several washing or incubation steps are involved (Koonce et al., 2020). Even when chemical fixation is employed prior to HPF, ultrastructural preservation is drastically enhanced, indicating that the most problematic steps in the conventional sample preparation protocol are indeed post-fixation and especially dehydration. This procedure is applicable for a wide range of specimens ranging from highly labile tissues to cells infected with Hepatitis C virus (Romero-Brey and Bartenschlager, 2015, Sosinsky et al., 2008).

Since TEM-tomography is able to achieve high resolution 3D-data for volumes below 500 nm thin sections, a great improvement to understand escape of pathogens would be to also visualise whole cells or larger volumes. For conventional sample preparation this has been already shown for *M. marinum* infected *D. discoideum* and other host-pathogen systems such as epithelial cells infected with *Shigella* (Weiner et al., 2016a, López-Jiménez et al., 2018, Anand et al., 2023). In principle, specimens prepared with the workflow developed in this study could also be directly processed via focused ion beam (FIB)-SEM to provide high volumetric information with EM resolution (Villinger et al., 2012). This further underlines the versatility of our approach and would allow also correlation in three dimensions. Because EM allows us to see not just one but all cellular compartments, we can conduct correlative studies on other organelles that potentially interact directly with pathogens or the MCV, for example the

endoplasmic reticulum (Anand et al., 2023).

Overall, our workflow provides the first approach to correlatively visualise adherent *D. discoideum* cells infected with *M. marinum* in a more native state using HPF and FS. This allows data to be evaluated more accurately and vacuole escape to be detected with near-atomic spatial resolution in three dimensions. The low cost and ease of implementation of our approach also have important advantages for monitoring membrane damage and exit events in other infection systems.

Experimental Procedures

D. discoideum strains and cell culture

All the *D. discoideum* material is listed in Table 1. *D. discoideum* wild type (AX2) was cultured axenically at 22 °C in Hl5c medium (Foremedium) in the presence of 100 U/mL penicillin and 100 µg/mL streptomycin, respectively. The GFP-ABD expressing cells were electroporated with pDM1044-AmtA-mCherry (Barisch et al., 2015b) and grown in Hl5c containing the respective antibiotics (hygromycin 50 µg/ml and G418 at 5 µg/ml).

Mycobacteria strains and cell culture

M. marinum was cultured in 7H9 medium supplemented with 10 % OADC, 0.2 % glycerol and 0.05 % Tween-80 at 32 °C in shaking at 150 rpm until an OD_{600} of 1 (~1.5 x 10^8 bacteria/ml). To prevent bacteria from clumping, flasks containing 5 mm glass beads were used. To generate wt mycobacteria expressing eBFP, the unlabelled strain was transformed with the pTEC18 plasmid and cultured in medium containing 25 µg/ml hygromycin.

D. discoideum infection with M. marinum

To prepare *D. discoideum* for infection, cells were grown overnight in 10-cm dishes in media devoid of antibiotics until confluency. The infection was carried out as previously described (Hagedorn and Soldati, 2007, Barisch et al., 2015a). Briefly, for a final multiplicity of infection (MOI) of 10, 5 x 10^8 bacteria were washed twice and resuspended in 500 µl Hl5c. To remove clumps, bacteria were passed 10 times through a 25-gauge needle and added to a 10-cm dish of *D. discoideum* cells. To increase the phagocytosis efficiency, the plates were centrifuged at 500 g for two times for 10 min at RT. After 20-30 min, the extracellular bacteria were removed by several washes with Hl5c. Finally, the infected cells were taken up in 30 ml of Hl5c at a density of 1 x 10^6 cells/ml supplemented with 5 µg/ml streptomycin and 5 U/ml penicillin to prevent growth of extracellular bacteria and incubated at 25 °C at 130 rpm. At 24 hpi, samples were taken and prepared for live imaging.

Preparation of sapphire discs

Before usage, sapphire discs (3mm x 0.16 mm) were acid cleaned. To this end, the discs were

soaked in 3.7 % hydrochloric acid (HCl) for an hour on a tumbler, washed with de-ionised water, with 100 % ethanol and air dried. Next, sapphires were equipped with a coordinate system by gold sputtering and a gold spacer to optimize image acquisition. The spacer consisted of a 3-mm gold grid (G2620A, Plano) with a central aperture of 2 mm and was glued onto the sapphire disc using Loctite AA 350 (Henkel, Hemel Hempstead, UK). The glue was polymerized overnight in a Leica AFS2. To improve cell adherence, sapphires were then incubated with 1 mg/ml PLL (P1274, Sigma) for 3 hrs at 37 °C. Unbound PLL was removed by three washes with double distilled water, air dried on Kimtech paper (#7552, Diagonal) and stored at RT.

Pre-fixation and fluorescence imaging by spinning disc confocal microscopy

Before seeding infected cells, 6 - 8 sapphire discs were washed twice with HI5c (without antibiotics), placed in a 2-well µ-ibidi dish and checked under a light microscope for handling errors (flipped upside down?). 70 % confluent sapphires were prepared by adding the cells and frequent inspection with a cell culture microscope. To remove floating cells, the medium was then replaced with fresh HI5c filtered medium. Prior to image acquisition, the sapphires with cells were briefly dipped into 2% GA in HI5c filtered and transferred with the cells and gold spacer facing the objective into a custom holder containing 0.5 % GA in HI5c filtered for light microscopy.

The Zeiss Cell Observer.Z1 is an inverted microscope, fully motorized and equipped with a Yokogawa Spinning Disc Unit CSU-X1a 5000 with a custom-built acrylic glass incubation chamber. The chamber was set to 25 °C 30 min prior to image acquisition. Alpha Plan-Apochromat 63x (NA 1.46, TIRF, oil immersion equipped with DIC slider EC PN 63x 1.25 III, CA 63x /1.2 W III), Plan-Apochromat 40x (NA 1.4, DIC, oil immersion equipped with DIC slider CA 40x /1.2 W, LD CA 40x /1.1 W III), LD LCI Plan-Apochromat 25x (NA 0.8, DIC, immersion: oil, water, and glycerin, equipped with DIC slider LCI PN 25x/0.8 II) and Plan-Neofluar 10x (NA. 0.3, DIC I, Ph 1, air) were used as objectives. The system is equipped with computer-controlled multi-color laser module with AOTF combiner (405 nm diode laser, max. power 50 mW, 488 nm optically pumped semiconductor laser, max. power 100 mW, 561 nm diode laser, max. power 40 mW, 635 nm diode laser, max. power 30 mW). The photometrics Evolve EMCCD camera was used and contained filters for blue (Zeiss Filter set 49), eGFP (Zeiss Filter set 38 HE) and Cy3 (Zeiss Filter set 43 HE). An area of 512 x 512 pixels with binning 1x1 was imaged with laser power of 20% to 30% for 488 nm, 10% to 20% for 405 nm and 40% to 50% for 561 nm. All channels were captured with a 100 ms exposure time. Data was acquired in Zeiss ZEN 2012 (blue edition) and stored in the OMERO 5.6.4 database. Images were processed using FIJI/ImageJ and deconvolved using the Huygens Software from Scientific Volume Imaging (Netherlands).

High pressure freezing (HPF)

Directly after acquisition of the last light microscopy image, sapphire discs were further processed for high-pressure freezing (HPF). To this end, the discs were placed with the cells and gold spacer facing the flat side of a 3 mm aluminum planchette no. 242 (Engineering Office M. Wohlwend GmbH, Sennwald, Switzerland) which was dipped into 1-hexadecene (822064, Merck). Subsequently, the assembly was placed in the HPF-holder and immediately frozen using a Wohlwend HPF Compact 03 high-pressure freezer (Engineering Office M. Wohlwend GmbH, Sennwald, Switzerland). The vitrified samples were stored in homemade storage vessels consisting of 0.5 ml tubes with cut-off tops and bottoms. A fine mesh was bonded to the bottom to allow the flow of solutions to the samples while preventing them from falling.

Freeze substitution (FS)

Prior to FS, the aluminum planchettes were separated from the sapphire discs in liquid nitrogen. All steps were conducted with sapphire discs in aforementioned vessels. The sapphire discs were then immersed in a substitution solution containing 1 % osmium tetroxide (19134, Electron Microscopy Sciences), 0.1 % uranyl acetate (E22400, Electron Microscopy Sciences) and 5 % H_2O in anhydrous acetone (83683.230, VWR) pre-cooled to −90 °C. The FS was performed in a Leica AFS2 (Leica, Wetzlar, Germany): 27 hrs at −90 °C, 12 hrs at −60 °C, 12 hrs at −30 °C and 1 hr at 0 °C. After 5 washes with anhydrous acetone on ice, the discs were stepwise embedded in EPON 812 (Roth, Karlsruhe, Germany), incubated with acetone (30 % EPON, 60 % EPON, 100 % EPON) and finally polymerized for 48 hrs at 60 °C. Semithin sections of 250 nm were cut with a Leica UC7 ultramicrotome using diamond knives (Diatome, Switzerland). Sections were collected on formvar-coated grids and post-stained for 30 min with 2 % uranyl acetate and 20 min in 3 % lead citrate and analyzed with a JEM 2100-Plus (Jeol, Japan) operating at 200 kV equipped with a 20-megapixel CMOS XAROSA camera (EMSIS, Muenster, Germany).

Tomography acquisition

For TEM tomography, 250 nm thick sections were labelled with 10 or 15 nm protein-A-gold fiducials on both sides prior to post-contrasting. Tilt series were acquired from ± 60° with 1 ° increments using the TEMography software (Jeol, Japan) and a JEM 2100-Plus operating at 200 kV and equipped with a 20-megapixel CMOS XAROSA camera (EMSIS, Muenster, Germany). Nominal magnifications and pixel size were 10000 x and 0.94 nm (Figure 5b-e) and 15000 x and 0.62 nm (Figure 5f).Tomograms were reconstructed using the back projection algorithm in IMOD (Kremer et al., 1996). Segmentation was done manually using IMOD or Microscopy Image Browser (Belevich et al., 2016) and animations were visualised using

Amira-Avizo (Thermo Fisher Scientific, Waltham, USA). For visualisation of the MCV in Figure 5b-e two independent tomograms were stitched together using Amira-Avizo.

Acknowledgments

Conflict of interests

The authors declare that they have no conflict of interest.

Table 1 Material used in this publication.

D. discoideum strains	Relevant characteristics	Source/Reference
AX2	wild type	www.dictybase.org

D. discoideum plasmids	Relevant characteristics	Source/Reference
GFP-ABD	pDXA-GFP-ABD120, G418^r, Amp^r	(Pang et al., 1998)
AmtA-mCherry	pDM1044-AmtA-mCherry, Hyg^r, Amp^r	

M. marinum strains	Relevant characteristics	Source/Reference
M. marinum M	wt, parental strain	L. Ramakrishnan (University of Cambridge)

Mycobacteria plasmids	Relevant characteristics	Source/Reference
pTEC18	eBFP2 under control of the MSP promoter, Hyg^r, Amp^r	Addgene #30177 (Takaki et al., 2013)

References

ADER, N. R., HOFFMANN, P. C., GANEVA, I., BORGEAUD, A. C., WANG, C., YOULE, R. J. & KUKULSKI, W. 2019. Molecular and topological reorganizations in mitochondrial architecture interplay during Bax-mediated steps of apoptosis. *eLife,* 8**,** e40712.

ANAND, A., MAZUR, A.-C., ROSELL-AREVALO, P., FRANZKOCH, R., BREITSPRECHER, L., LISTIAN, S. A., HÜTTEL, S. V., MÜLLER, D., SCHÄFER, D. G., VORMITTAG, S., HILBI, H., MANIAK, M., GUTIERREZ, M. & BARISCH, C. 2023. ER-dependent membrane repair of mycobacteria-induced vacuole damage. *bioRxiv***,** 2023.04.17.537276.

BARISCH, C., HOLTHUIS, J. C. M. & COSENTINO, K. 2023. Membrane damage and repair: a thin line between life and death. *Biological Chemistry*.

BARISCH, C., LÓPEZ-JIMÉNEZ, A. T. & SOLDATI, T. 2015a. Live imaging of Mycobacterium marinum infection in Dictyostelium discoideum. *Methods Mol Biol,* 1285**,** 369-85.

BARISCH, C., PASCHKE, P., HAGEDORN, M., MANIAK, M. & SOLDATI, T. 2015b. Lipid droplet dynamics at early stages of Mycobacterium marinum infection in Dictyostelium. *Cell Microbiol,* 17**,** 1332-49.

BARISCH, C. & SOLDATI, T. 2017. Mycobacterium marinum Degrades Both Triacylglycerols and Phospholipids from Its Dictyostelium Host to Synthesise Its Own Triacylglycerols and Generate Lipid Inclusions. *PLoS Pathog,* 13**,** e1006095.

BELEVICH, I., JOENSUU, M., KUMAR, D., VIHINEN, H. & JOKITALO, E. 2016. Microscopy Image Browser: A Platform for Segmentation and Analysis of Multidimensional Datasets. *PLOS Biology,* 14**,** e1002340.

BOZZOLA, J. & KUO, J. 2014. Electron Microscopy: Methods and Protocols.

BROWN, E., VAN WEERING, J., SHARP, T., MANTELL, J. & VERKADE, P. 2012. Chapter 10 - Capturing Endocytic Segregation Events with HPF-CLEM. *In:* MÜLLER-REICHERT, T. & VERKADE, P. (eds.) *Methods in Cell Biology.* Academic Press.

BUSSI, C. & GUTIERREZ, M. G. 2019. Mycobacterium tuberculosis infection of host cells in space and time. *FEMS Microbiol Rev,* 43**,** 341-361.

CARDENAL-MUNOZ, E., BARISCH, C., LEFRANCOIS, L. H., LOPEZ-JIMENEZ, A. T. & SOLDATI, T. 2017. When Dicty Met Myco, a (Not So) Romantic Story about One Amoeba and Its Intracellular Pathogen. *Front Cell Infect Microbiol,* 7**,** 529.

CORNILLON, S., FROQUET, R. & COSSON, P. 2008. Involvement of Sib proteins in the regulation of cellular adhesion in Dictyostelium discoideum. *Eukaryot Cell.* United States.

GERSTENMAIER, L., PILLA, R., HERRMANN, L., HERRMANN, H., PRADO, M., VILLAFANO, G. J., KOLONKO, M., REIMER, R., SOLDATI, T., KING, J. S. & HAGEDORN, M. 2015. The autophagic machinery ensures nonlytic transmission of mycobacteria. *Proceedings of the National Academy of Sciences,* 112**,** E687-E692.

HAGEDORN, M., ROHDE, K. H., RUSSELL, D. G. & SOLDATI, T. 2009. Infection by tubercular mycobacteria is spread by nonlytic ejection from their amoeba hosts. *Science,* 323**,** 1729-33.

HAGEDORN, M. & SOLDATI, T. 2007. Flotillin and RacH modulate the intracellular immunity of Dictyostelium to Mycobacterium marinum infection. *Cell Microbiol,* 9**,** 2716-33.

HEILIGENSTEIN, X., DE BEER, M., HEILIGENSTEIN, J., EYRAUD, F., MANET, L., SCHMITT, F., LAMERS, E., LINDENAU, J., KEA-TE LINDERT, M., SALAMERO, J., RAPOSO, G., SOMMERDIJK, N., BELLE, M. & AKIVA, A. 2021. Chapter 6 - HPM live μ for a full CLEM workflow. *In:* MÜLLER-REICHERT, T. & VERKADE, P. (eds.) *Methods in Cell Biology.* Academic Press.

HUMBEL, B. & MÜLLER, M. 1985. Freeze substitution and low temperature embedding. *Scanning Electron Microscopy,* 4**,** 19.

IWADATE, Y. & YUMURA, S. 2008. Actin-based propulsive forces and myosin-II-based contractile forces in migrating Dictyostelium cells. *J Cell Sci,* 121**,** 1314-24.

KANEKO, Y. & WALTHER, P. 1995. Comparison of Ultrastructure of Germinating Pea Leaves Prepared by High-Pressure Freezing–Freeze Substitution and Conventional Chemical Fixation. *Journal of Electron Microscopy,* 44**,** 104-109.

KOMMNICK, C. & HENSEL, M. 2021. Correlative Light and Scanning Electron Microscopy to Study Interactions of Salmonella enterica with Polarized Epithelial Cell Monolayers. *Methods Mol Biol,* 2182**,** 103-115.

KOONCE, M., TIKHONENKO, I. & GRÄF, R. 2020. Dictyostelium Cell Fixation: Two Simple Tricks. *Methods and Protocols,* 3**,** 47.

KREITMEIER, M., GERISCH, G., HEIZER, C. & MÜLLER-TAUBENBERGER, A. 1995. A talin homologue of Dictyostelium rapidly assembles at the leading edge of cells in response to chemoattractant. *J Cell Biol,* 129**,** 179-88.

KREMER, J. R., MASTRONARDE, D. N. & MCINTOSH, J. R. 1996. Computer visualization of three-dimensional image data using IMOD. *J Struct Biol,* 116**,** 71-6.

LEE, H. J., WOO, Y., HAHN, T. W., JUNG, Y. M. & JUNG, Y. J. 2020. Formation and Maturation of the Phagosome: A Key Mechanism in Innate Immunity against Intracellular Bacterial Infection. *Microorganisms,* 8.

LERNER, T. R., QUEVAL, C. J., LAI, R. P., RUSSELL, M. R., FEARNS, A., GREENWOOD, D. J., COLLINSON, L., WILKINSON, R. J. & GUTIERREZ, M. G. 2020. Mycobacterium tuberculosis cords within lymphatic endothelial cells to evade host immunity. *JCI Insight,* 5.

LIM, J. J., GRINSTEIN, S. & ROTH, Z. 2017. Diversity and Versatility of Phagocytosis: Roles in Innate Immunity, Tissue Remodeling, and Homeostasis. *Front Cell Infect Microbiol,* 7**,** 191.

LOMBARDI, M. L., KNECHT, D. A. & LEE, J. 2008. Mechano-chemical signaling maintains the rapid movement of Dictyostelium cells. *Experimental Cell Research,* 314**,** 1850-1859.

LÓPEZ-JIMÉNEZ, A. T., CARDENAL-MUÑOZ, E., LEUBA, F., GERSTENMAIER, L., BARISCH, C., HAGEDORN, M., KING, J. S. & SOLDATI, T. 2018. The ESCRT and autophagy machineries cooperate to repair ESX-1-dependent damage at the Mycobacterium-containing vacuole but have opposite impact on containing the infection. *PLoS Pathog,* 14**,** e1007501.

MALINOVSKA, L., PALM, S., GIBSON, K., VERBAVATZ, J.-M. & ALBERTI, S. 2015. Dictyostelium discoideum has a highly Q/N-rich proteome and shows an unusual resilience to protein aggregation. *Proceedings of the National Academy of Sciences,* 112**,** E2620-E2629.

MAZIA, D., SCHATTEN, G. & SALE, W. 1975. Adhesion of cells to surfaces coated with polylysine. Applications to electron microscopy. *J Cell Biol,* 66**,** 198-200.

MCDONALD, K. L. & AUER, M. 2006. High-Pressure Freezing, Cellular Tomography, and Structural Cell Biology. *BioTechniques,* 41**,** 137-143.

MIJANOVIĆ, L. & WEBER, I. 2022. Adhesion of Dictyostelium Amoebae to Surfaces: A Brief History of Attachments. *Front Cell Dev Biol,* 10**,** 910736.

MOOR, H. 1987. Theory and Practice of High Pressure Freezing. *In:* STEINBRECHT, R. A. & ZIEROLD, K. (eds.) *Cryotechniques in Biological Electron Microscopy.* Berlin, Heidelberg: Springer Berlin Heidelberg.

PANG, K. M., LEE, E. & KNECHT, D. A. 1998. Use of a fusion protein between GFP and an actin-binding domain to visualize transient filamentous-actin structures. *Curr Biol,* 8**,** 405-8.

ROMERO-BREY, I. & BARTENSCHLAGER, R. 2015. Viral Infection at High Magnification: 3D Electron Microscopy Methods to Analyze the Architecture of Infected Cells. *Viruses,* 7**,** 6316-6345.

SOSINSKY, G. E., CRUM, J., JONES, Y. Z., LANMAN, J., SMARR, B., TERADA, M., MARTONE, M. E., DEERINCK, T. J., JOHNSON, J. E. & ELLISMAN, M. H. 2008. The combination of chemical fixation procedures with high pressure freezing and freeze substitution preserves highly labile tissue ultrastructure for electron tomography applications. *Journal of structural biology,* 161**,** 359-371.

TAKAKI, K., DAVIS, J. M., WINGLEE, K. & RAMAKRISHNAN, L. 2013. Evaluation of the pathogenesis and treatment of Mycobacterium marinum infection in zebrafish. *Nat Protoc,* 8**,** 1114-24.

UCHIKAWA, T., YAMAMOTO, A. & INOUYE, K. 2011. Origin and function of the stalk-cell vacuole in Dictyostelium. *Dev Biol,* 352**,** 48-57.

VANHECKE, D., GRABER, W. & STUDER, D. 2008. Chapter 9 Close-to-Native Ultrastructural Preservation by High Pressure Freezing. *Methods in Cell Biology.* Academic Press.

VERKADE, P. 2008. Moving EM: the Rapid Transfer System as a new tool for correlative light and electron microscopy and high throughput for high-pressure freezing. *Journal of Microscopy,* 230**,** 317-328.

VILLINGER, C., GREGORIUS, H., KRANZ, C., HÖHN, K., MÜNZBERG, C., VON WICHERT, G., MIZAIKOFF, B., WANNER, G. & WALTHER, P. 2012. FIB/SEM tomography with TEM-like resolution for 3D imaging of high-pressure frozen cells. *Histochemistry and Cell Biology,* 138**,** 549-556.

WEBER, I., WALLRAFF, E., ALBRECHT, R. & GERISCH, G. 1995. Motility and substratum adhesion of Dictyostelium wild-type and cytoskeletal mutant cells: a study by RICM/bright-field double-view image analysis. *J Cell Sci,* 108 (Pt 4)**,** 1519-30.

WEINER, A., MELLOUK, N., LOPEZ-MONTERO, N., CHANG, Y.-Y., SOUQUE, C., SCHMITT, C. & ENNINGA, J. 2016a. Macropinosomes are Key Players in Early Shigella Invasion and Vacuolar Escape in Epithelial Cells. *PLOS Pathogens,* 12**,** e1005602.

WEINER, A., MELLOUK, N., LOPEZ-MONTERO, N., CHANG, Y. Y., SOUQUE, C., SCHMITT, C. & ENNINGA, J. 2016b. Macropinosomes are Key Players in Early Shigella Invasion and Vacuolar Escape in Epithelial Cells. *PLoS Pathog,* 12**,** e1005602.

WESSELS, D., VAWTER-HUGART, H., MURRAY, J. & SOLL, D. R. 1994. Three-dimensional dynamics of pseudopod formation and the regulation of turning during the motility cycle of Dictyostelium. *Cell Motil Cytoskeleton,* 27**,** 1-12.
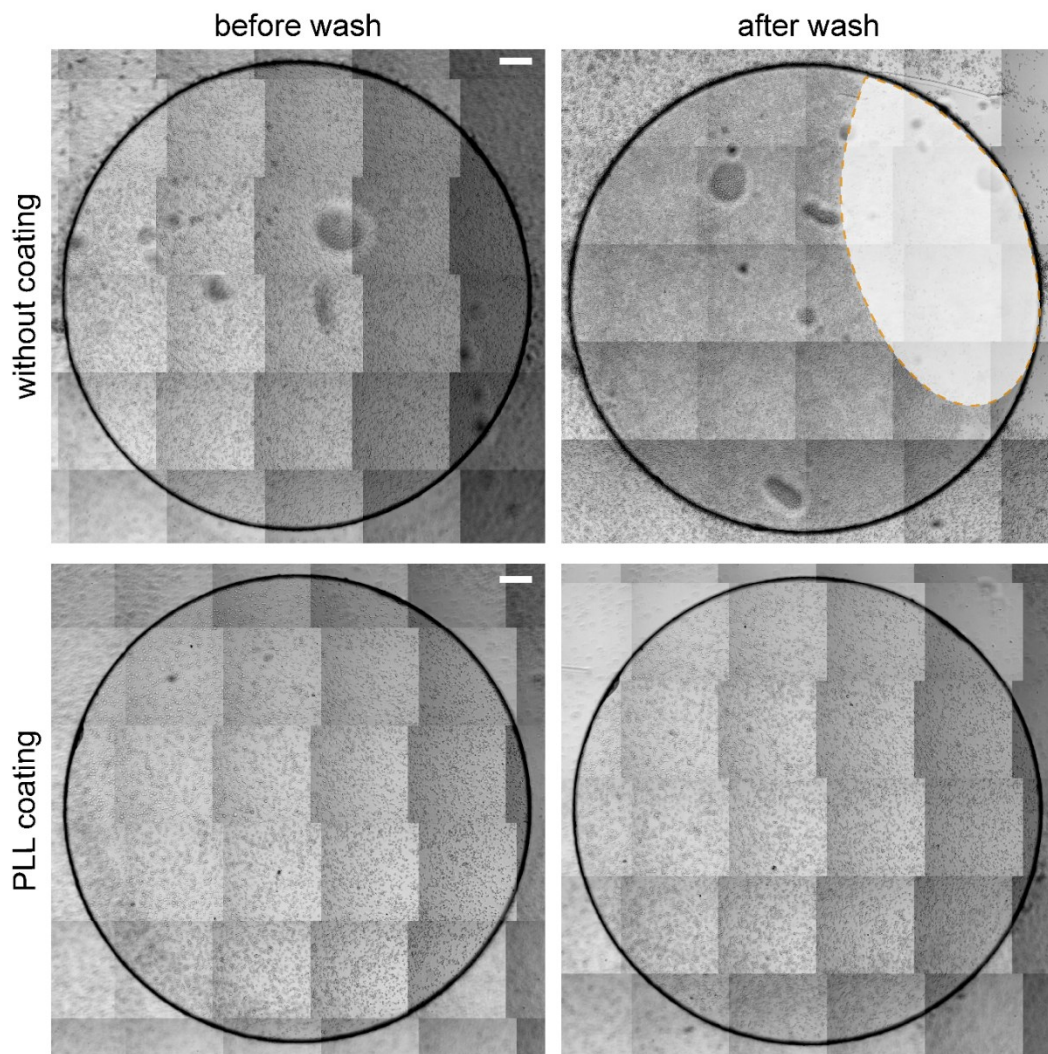
Supplementary figures

FIGURE S1 PLL improves *D. discoideum* adherence on sapphire discs. *D. discoideum* wild type was seeded on non-coated or PLL-coated sapphire discs and imaged live before and after washing with Hl5c. An area in which many cells were lost is indicated (orange line). Scale bar, 200 µm.
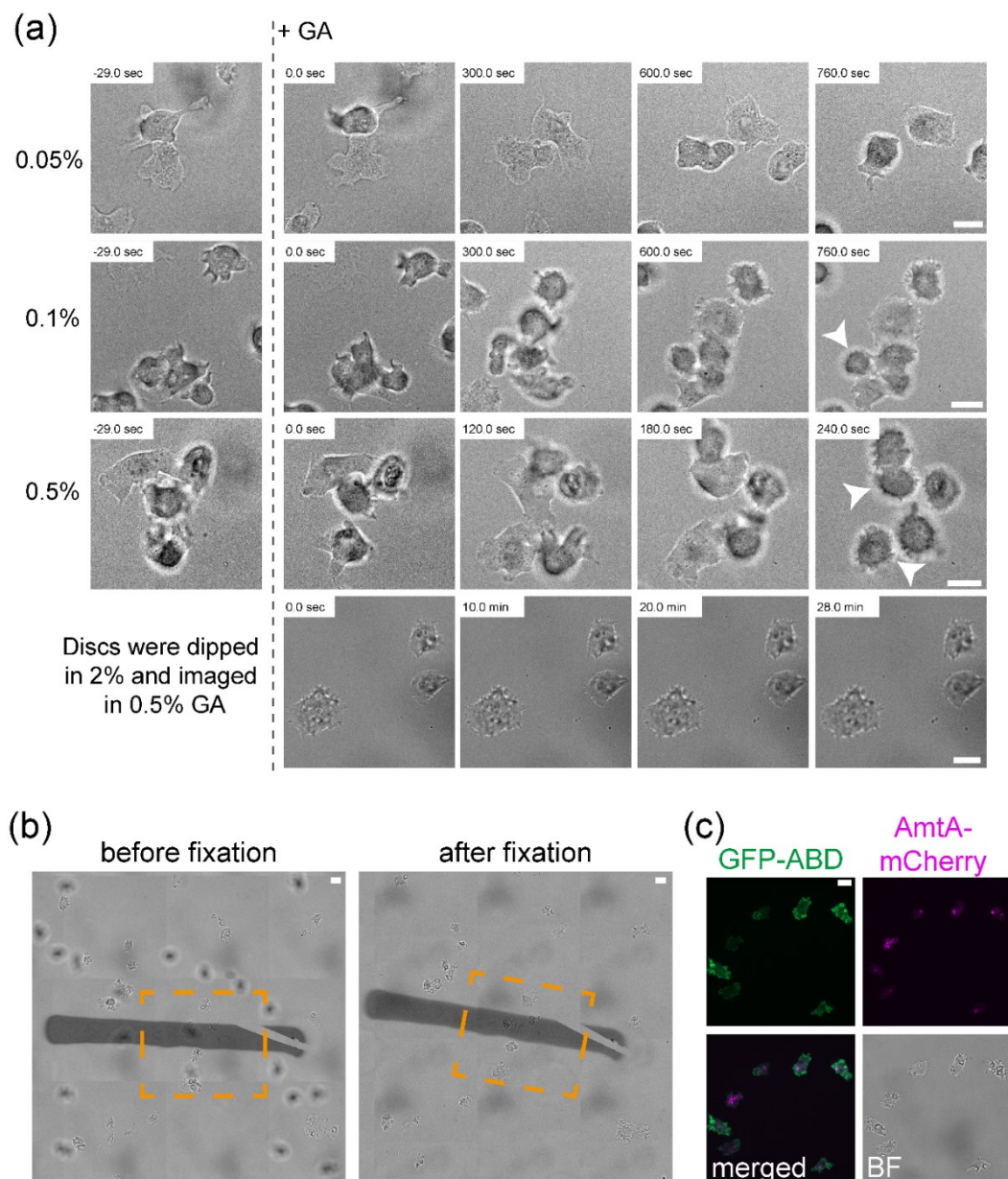
FIGURE S2 Pre-chemical fixation immobilises *D. discoideum* and does not impact on background fluorescence. (a) Cell fixation upon exposure to 0.05 %, 0.1 %, 0.5 % GA or upon short immersion in 2 % GA. Incubation with 0.1 % or 0.5 % GA leads to cell death (round cells) while a short immersion in 2 % GA immobilised the cells up to 30 min in 0.5 % GA. (b) Relocation and fluorescence imaging of cells after fixation. (c) 0.5 % GA does not produce any background noise. Cells expressing GFP-ABD and AmtA-mCherry were seeded on sapphires with or without coordinates before movies were recorded. Arrowheads indicate round cells. After fixation, cells can be tracked back (orange box). Fixed GFP-ABD cells were imaged live using the SD microscope with the 63x objective. Please see also Movies S1-5. Scale bar, 10 µm.

Supplementary movies

MOVIES S1-S5 Time lapse movies of *D. discoideum* in presence of 0.05 % (S1), 0.1 % (S2), 0.5 % (S3), 2 % GA (S4) and 3 % PFA and 0.05 % GA (S5). For more information see Figure S2.

MOVIES S6-S7 Tomogram (S6) and 3D-reconstruction (S7) of the ruptured MCV containing several bacteria as shown in Figure 5. For more information see Figure 5.

3.1.2. Author contributions

Here, I summarise the contributions made by each author to this section of the thesis.

I generated the strains, conducted the infection experiments as well as light microscopy. Rico Franzkoch carried out the transmission electron microscopy and tomography. Together, we improved the fixation protocol, adapted the imaging setup, prepared the final figures and wrote the original draft of the manuscript. Leonhard Breitsprecher assisted with the stitching of the tomograms. Olympia E. Psathaki supervised the electron microscopy experiments. Caroline Barisch supervised the experiments and authored the final draft of the manuscript.

3.2.1. ER-dependent membrane repair of mycobacteria-induced vacuole damage

Authors

Aby Anand[a], Anna-Carina Mazur[a], Patricia Rosell-Arevalo[b], Rico Franzkoch[c], Leonhard Breitsprecher[c], Stevanus A. Listian[a], Sylvana V. Hüttel[a], Danica Müller[a], Deise G. Schäfer[a], Simone Vormittag[d], Hubert Hilbi[d], Markus Maniak[e], Maximiliano G. Gutierrez[b] and Caroline Barisch[a,f,g,h,*]

Affiliations

[a]Division of Molecular Infection Biology, Department of Biology & Center of Cellular Nanoanalytics, University of Osnabrück, Osnabrück, Germany

[b]Host–Pathogen Interactions in Tuberculosis Laboratory, The Francis Crick Institute, London, United Kingdom

[c]iBiOs–integrated Bioimaging Facility, Center of Cellular Nanoanalytics, University of Osnabrück, Osnabrück, Germany

[d]Institute of Medical Microbiology, University of Zürich, Zürich, Switzerland

[e]Department of Cell Biology, University of Kassel, Kassel, Germany

[f]Centre for Structural Systems Biology, Hamburg, Germany

[g]Biology Department, University of Hamburg, Hamburg, Germany

[h]Leibniz Lung Center (Research Center Borstel), Borstel, Germany

*Corresponding author: Caroline.Barisch@uos.de – Tel: +49-541-969-7232

Running title Role of OSBP8 in mycobacterial infection

Abstract

Several intracellular pathogens, such as *Mycobacterium tuberculosis,* damage endomembranes to access the cytosol and subvert innate immune responses. The host counteracts endomembrane damage by recruiting repair machineries that retain the pathogen inside the vacuole.

Here, we show that the endoplasmic reticulum (ER)-Golgi protein oxysterol binding protein (OSBP) and its *Dictyostelium discoideum* homologue OSBP8 are recruited to the *Mycobacterium*-containing vacuole (MCV) dependent on the presence of the ESX-1 secretion system, suggesting that their mobilization is associated with membrane damage. Lack of OSBP8 causes a hyperaccumulation of phosphatidylinositol-4-phosphate (PI4P) on the MCV and decreased cell viability. OSBP8-depleted cells had reduced lysosomal and degradative capabilities of their vacuoles that favoured mycobacterial growth. In agreement with a potential role of OSBP8 in membrane repair, human macrophages infected with *M. tuberculosis* recruited OSBP in an ESX-1-dependent manner. These findings identified an ER-dependent repair mechanism for restoring MCVs in which OSBP8 functions to equilibrate PI4P levels on damaged membranes.

Importance

Tuberculosis still remains a global burden and is one of the top infectious diseases from a single pathogen. *Mycobacterium tuberculosis*, the causative agent, has perfected many ways to replicate and persist within its host. While mycobacteria induce vacuole damage to evade the toxic environment and eventually escape into the cytosol, the host recruits repair machineries to restore the MCV membrane. However, how lipids are delivered for membrane repair is poorly understood. Using advanced fluorescence imaging and volumetric correlative approaches, we demonstrate that this involves the recruitment of the ER-Golgi lipid transfer protein OSBP8 in the *D. discoideum*/ *M. marinum* system. Strikingly, depletion of OSBP8 affects lysosomal function accelerating mycobacterial growth. This indicates that an ER-dependent repair pathway constitutes a host defence mechanism against intracellular pathogens such as *M. tuberculosis*.

Keywords

Membrane repair, *Mycobacterium tuberculosis, Mycobacterium marinum, Dictyostelium discoideum,* macrophages, oxysterol binding protein, membrane contact site, sterol, phosphatidylinositol-4-phosphate, Sac1, lysosome.

Introduction

Cellular compartmentalization renders cells susceptible to membrane damage caused by

41

pathogens, chemicals or mechanical stressors. Endolysosomal damage by vacuolar pathogens disrupts the proton gradient between the endolysosome and the cytosol and reduces the efficacy of first-line innate immune defences. Several pathogens including *Mycobacterium tuberculosis* have evolved sophisticated strategies to avoid phagosome maturation and to overcome the ion gradients (H^+, Zn^{2+} or Cu^{2+}), creating an optimal environment for their proliferation (1). Membrane damage inflicted by pathogenic mycobacteria depends on the pathogenicity locus region of difference (RD) 1 encoding the type VII secretion system ESX-1. This leads among others to the leakage of Zn^{2+} from the *Mycobacterium*-containing vacuole (MCV) thus preventing the bacteria from zinc poisoning (2).

Endosomal sorting complex required for transport (ESCRT)-dependent membrane repair plays a role during the infection of *Dictyostelium discoideum* with *M. marinum*, a pathogenic mycobacterium that primarily infects poikilotherms and is genetically closely related to the tuberculosis (TB) group (3). Importantly, the host response and course of infection by *M. tuberculosis* and *M. marinum* share a high level of similarity (4) including the molecular machinery for host lipid acquisition and turnover (5). In *M. marinum*-infected *D. discoideum*, the ESCRT machinery cooperates with autophagy to repair EsxA-mediated damage at the MCV (6). The evolutionarily conserved E3-ligase TrafE mobilizes various ESCRT components to damaged lysosomes and the MCV (7). While the ESCRT components Tsg101, Chmp4/Vps32 and the AAA-ATPase Vps4 are recruited to small membrane ruptures, the autophagy machinery operates at places of extensive membrane damage (6). When ESCRT-dependent and autophagy pathways are disrupted, *M. marinum* escapes to the cytosol at very early infection stages, indicating that both mechanisms are needed to keep the bacteria inside the phagosome (6).

Two other repair pathways restore the integrity of broken lysosomal membranes in mammalian cells (8). Sphingomyelin (SM)-dependent repair operates at damaged lysosomes and ruptured vacuoles containing *Salmonella* Typhimurium (9) or *M. marinum* (10). Moreover, an endoplasmic reticulum (ER)-dependent membrane repair pathway has been described (11, 12). In this pathway, lysosomal damage results in the recruitment of PI4-kinase type 2-alpha (PI4K2A) generating high levels of phosphatidylinositol-4-phosphate (PI4P) (12). The accumulation of PI4P leads to the induction of ER-lysosome contacts and the mobilization of OSBP and several OSBP-related proteins (ORPs) that transfer cholesterol and phosphatidylserine (PS) from the ER to the ruptured lysosomes in exchange for PI4P (11, 12). Proteomics and transcriptomics analyses indicate that ER-dependent membrane repair might also play a role during mycobacterial infection in human macrophages (13) and in *D. discoideum* (14, 15). Genes encoding the proteins involved in the establishment of membrane

contact sites (MCS) with the ER or in lipid transfer are upregulated at infection stages, when major vacuolar damage occurs and the bacteria translocate to the cytosol. In this study, we investigated the role of OSBPs in ER-mediated membrane repair in the context of mycobacterial infection. We show that ESX-1-dependent membrane damage results in the mobilization of OSBP and its *D. discoideum* homologue OSBP8 to *M. tuberculosis*- and *M. marinum*-containing vacuoles, respectively. We demonstrate that OSBP8 is on ER-tubules in close contact with lysosomes and MCVs dependent on PI4P accumulation. OSBP8 depletion leads to cells that are less viable upon sterile damage. Upon infection, lack of OSBP8 causes a massive accumulation of PI4P on MCVs, impairs the functionality of this compartment and promotes mycobacterial replication. Altogether, our work reveals that OSBPs play an important role in equilibrating PI4P levels during ER-dependent repair to maintain the integrity of MCVs and contribute to the maintenance of the phagosomal innate immune defences against intracellular pathogens.

Results

Mycobacterial infection induces an ER-dependent repair gene expression signature

During lysosomal damage, cells stimulate a phosphatidylinositol (PI)-initiated signalling pathway for rapid lysosomal repair (12). This results in the recruitment of membrane tethers and lipid transfer proteins (LTPs) to ER-lysosome contact sites (11, 12). Analysis of RNA-sequencing data of *D. discoideum* during *M. marinum* infection (14, 15) revealed a possible role for ER-dependent repair: Genes encoding the homologues of the PI4P phosphatase Sac1 and several PI4Ks (*pi4k* and *pikD*) were upregulated at later infection stages when *M. marinum* inflicts major membrane damage (Fig. 1A). Additionally, the expression of many OSBPs is affected in complex manners during infection (Fig. 1B).

In *D. discoideum*, *M. marinum* resides in a compartment with partially lysosomal and post-lysosomal characteristics that is exposed to damage starting from early infection stages (6, 16). We investigated whether mycobacterial infection leads to the formation of ER-MCV contacts. Indeed, when cells expressing the ER-marker Calnexin-mCherry were infected with *M. marinum* and stained for the MCV-marker p80 (16), we observed Calnexin[+] ER-tubules in the close vicinity of the MCV (Fig. S1A). This is consistent with previous findings showing *M. tuberculosis* infection of dendritic cells, in which approximately 50% of the MCVs were Calnexin[+] (17). To gain a better understanding of the morphology of these sites, cells expressing GFP-actin-binding-domain (ABD) as well as the endosomal and MCV marker AmtA-mCherry (18) were infected and analysed by correlative light and electron microscopy (CLEM). The overexpression of GFP-ABD leads to a significant improvement of cell adhesion and was necessary to re-locate the cells after sample preparation for EM (19). By correlating
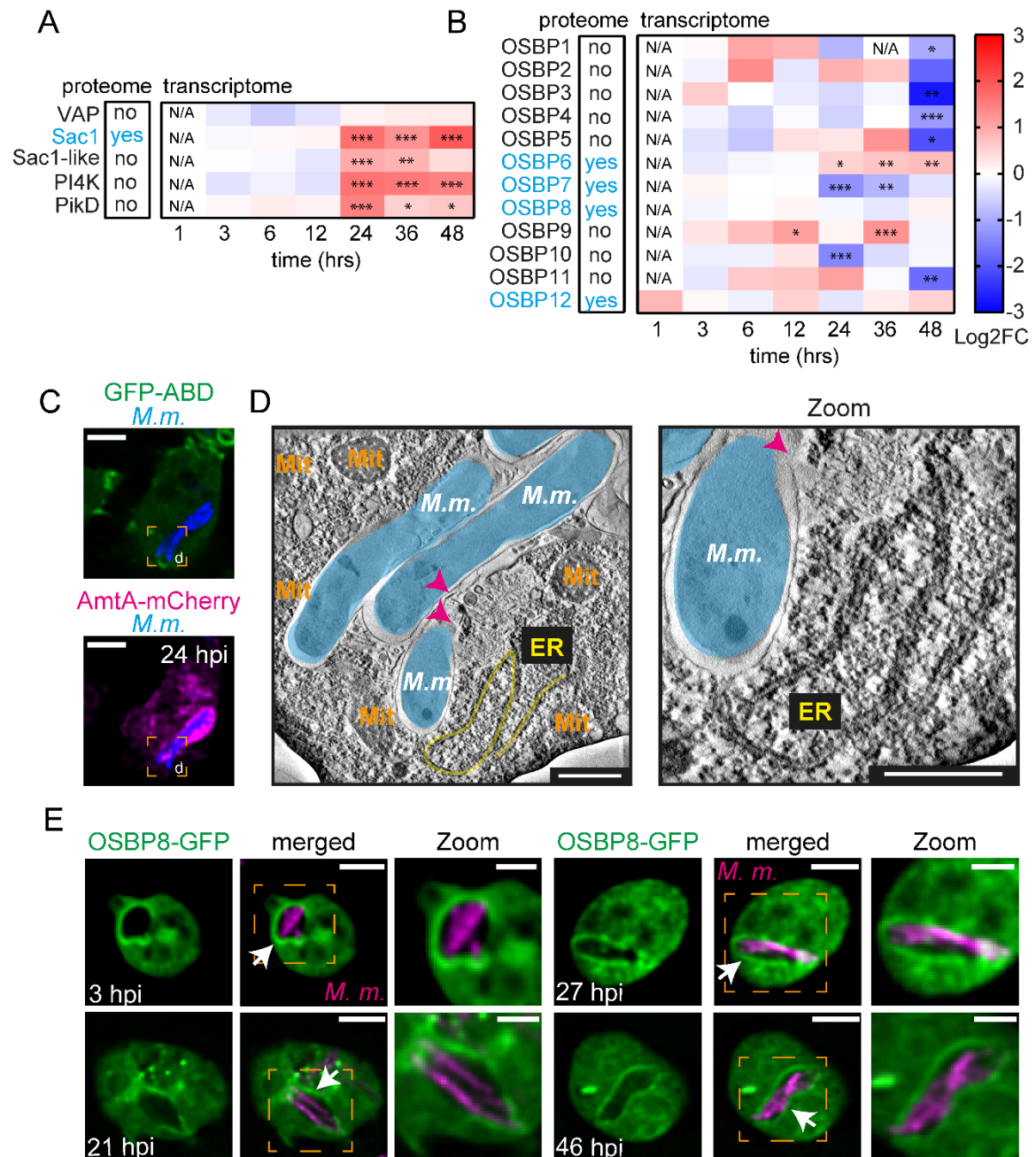
FIG 1 Evidence for ER-mediated repair and mobilization of OSBP8 during mycobacterial infection. (A-B) Proteomics (left) and heatmaps (right) representing the transcriptional data derived from (14) and (15). Cells were infected with GFP-expressing *M. marinum* wt. Samples were collected at the indicated time points. Statistically significant differences in expression are marked with asterisks (*, p < 0.05; **, p < 0.01; ***, p < 0.001). Colours indicate the amplitude of expression (in logarithmic fold change (Log2FC)) in infected cells compared to mock-infected cells: from red (highest expression) to blue (lowest expression). (C-D) CLEM to monitor ER-tubules close to ruptured MCVs. Cells expressing GFP-ABD and AmtA-mCherry were infected with eBFP-expressing *M. marinum*. At 24 hpi, cells on sapphire discs were imaged by SD microscopy in the presence of low concentrations of GA before high-pressure freezing. Left: deconvolved SD images, scale bars, 5 μm; right: representative EM micrographs, scale bars, 500 nm. Magenta arrow heads point to the ruptured MCV membrane.

FIG 1 legend continued

Mitochondria (Mit) were indicated in orange text, *M. marinum* (*M.m.*) were pseudo-coloured in cyan and ER-tubules in yellow. (E) Live cell imaging of OSBP8-GFP during infection. Cells overexpressing OSBP8-GFP were infected with mCherry-expressing *M. marinum*. At the indicated time points, cells were imaged live by SD microscopy. Arrows point to OSBP8-GFP$^+$ mycobacteria. Scale bars, 5 µm; Zoom, 2 µm. Images in (C and E) were deconvolved.

the images of vacuolar bacteria obtained by live cell imaging (AmtA$^+$) (Fig. 1C) with the corresponding EM micrographs, ER-tubules were seen close to ruptured MCVs (Fig. 1D).

In summary, we discovered a unique transcriptomic signature that, together with the observation of ER-tubules in the proximity of the MCV, supports the hypothesis that mycobacterial infection triggers ER-dependent membrane repair.

OSBP8-GFP is mobilized by intracellular mycobacteria

LTPs from the OSBP/ORP family are mobilized during ER-dependent lysosomal repair to provide lipids such as PS or cholesterol. Members of this protein family counter-transport these lipids in exchange for PI4P at ER-lysosome contacts. Sequence comparison of the twelve *D. discoideum* OSBPs with human and yeast homologues revealed that family members consist primarily of the lipid-binding OSBP-related domain (ORD) (Fig. S1B) (20). By analysing recent proteomics data from infected *D. discoideum* (14), we found four out of the twelve *D. discoideum* homologues enriched on isolated MCVs (i.e. OSBP6, OSBP7, OSBP8 and OSBP12) (Fig. 1B). These proteins are potential candidates for OSBP-mediated ER-dependent repair during infection. The fact that OSBP8 is the closest homologue to mammalian family members (20) and is the only *D. discoideum* OSBP with a fully conserved EQVSHHPP lipid-binding motif (Fig. S1C) prompted us to investigate its localization during mycobacterial infection and to use OSBP7, which is more distantly related, as a control.

To study the subcellular localization of OSBP8, we generated cells overexpressing either GFP-OSBP8 (N-terminally GFP-tagged OSBP8) or OSBP8-GFP (C-terminally GFP-tagged OSBP8) (Fig. S2A-F). OSBP8-GFP was partly cytosolic and co-localized with Calnexin-mCherry at the perinuclear ER as well as with ZntC-mCherry, a zinc transporter that is located at the Golgi and/or recycling endosomes (21) (Fig. S2A-B). Interestingly, the membrane localization of OSBP8 was abolished in cells overexpressing GFP-OSBP8, indicating that the N-terminus is important for membrane targeting (Fig. S2C-D).

Strikingly, when the localization of OSBP8 was monitored during infection with *M. marinum*, OSBP8-GFP re-localized to MCVs starting from early stages (Fig. 1E). In contrast, we did not observe such a prominent accumulation of either OSBP8-GFP or GFP-OSBP8 on bead-

containing phagosomes (BCPs) (Fig. S2E-F). OSBP7 localized in the cytosol and nucleus in non-infected cells and did not re-localize during infection (Fig. S2G) suggesting that some OSBPs are specifically mobilized.

Overall, OSBP8 is recruited to MCVs starting from early infection stages, which correlates with the occurrence of MCV-damage in *D. discoideum* (6).

OSBP8-GFP is located on ER-tubules in the vicinity of damaged MCVs

To test if OSBP8-GFP was recruited to MCVs or cytosolic mycobacteria, we infected cells expressing OSBP8-GFP and AmtA-mCherry and performed lattice light sheet microscopy (LLSM) (Fig. 2A-C). OSBP8-GFP did not colocalize with the MCV membrane (AmtA⁺), but it was recruited to its immediate vicinity (Fig. 2A-B; see also Movie S1). This finding was further corroborated by a 3D analysis that demonstrates that some MCVs were fully enclosed by OSBP8-GFP⁺ structures (Fig. 2C; see also Movie S2). To visualize these potential ER-MCV contacts, expansion microscopy (ExM) of cells expressing OSBP8-GFP and Calnexin-mCherry was carried out. In line with the previous results, Calnexin-mCherry⁺ and OSBP8-GFP⁺ ER-tubules were observed in the vicinity of the MCV (Fig. 2D). Additionally, we performed CLEM (Fig. S3A-B) and 3D-CLEM (Fig. 2E-G, Fig. S3C) to acquire a deeper insight of the morphology of these micro-compartments. The CLEM analysis confirmed by live imaging that OSBP8-mCherry is recruited to the MCV. Strikingly, in the corresponding EM images OSBP8-mCherry coincides with ER-tubules that were in the vicinity of seemingly damaged MCVs (Fig. S3A-B). For volumetric analysis, the infected cells were subjected after live cell imaging to serial block face-scanning electron microscopy (SBF-SEM). In agreement with our previous observations, electron micrographs and the 3D rendering clearly showed that the MCV is surrounded by OSBP8⁺ ER-tubules (Fig. 2E-G, Fig. S3C; see also Movie S3). Altogether, this supports the hypothesis that OSBP8 might be potentially involved in ER-dependent repair during mycobacterial infection.

Next, we tested if the mobilization of OSBP8 to the MCV is damage-dependent and performed infections with a mutant of *M. marinum* lacking ESX-1 (ΔRD1) (6). Remarkably, the localization of OSBP8-GFP in the vicinity of the MCV was abolished in cells infected with the ΔRD1 mutant (Fig. 3A-B). A similar observation was made with the ΔCE mutant that has a functional ESX-1 system but lacks EsxA together with its chaperone EsxB (Fig. 3C). Since overexpression can lead to artefacts and to the induction of MCS, we generated a chromosomally-tagged C-terminal GFP-fusion of OSBP8 (OSBP8::GFP) in which OSBP8 is under the control of its endogenous promoter and expressed 20 times less than in OSBP8-GFP overexpressing cells (Fig. S4A-B). OSBP8::GFP shows a similar distribution and is also recruited to the MCV in an
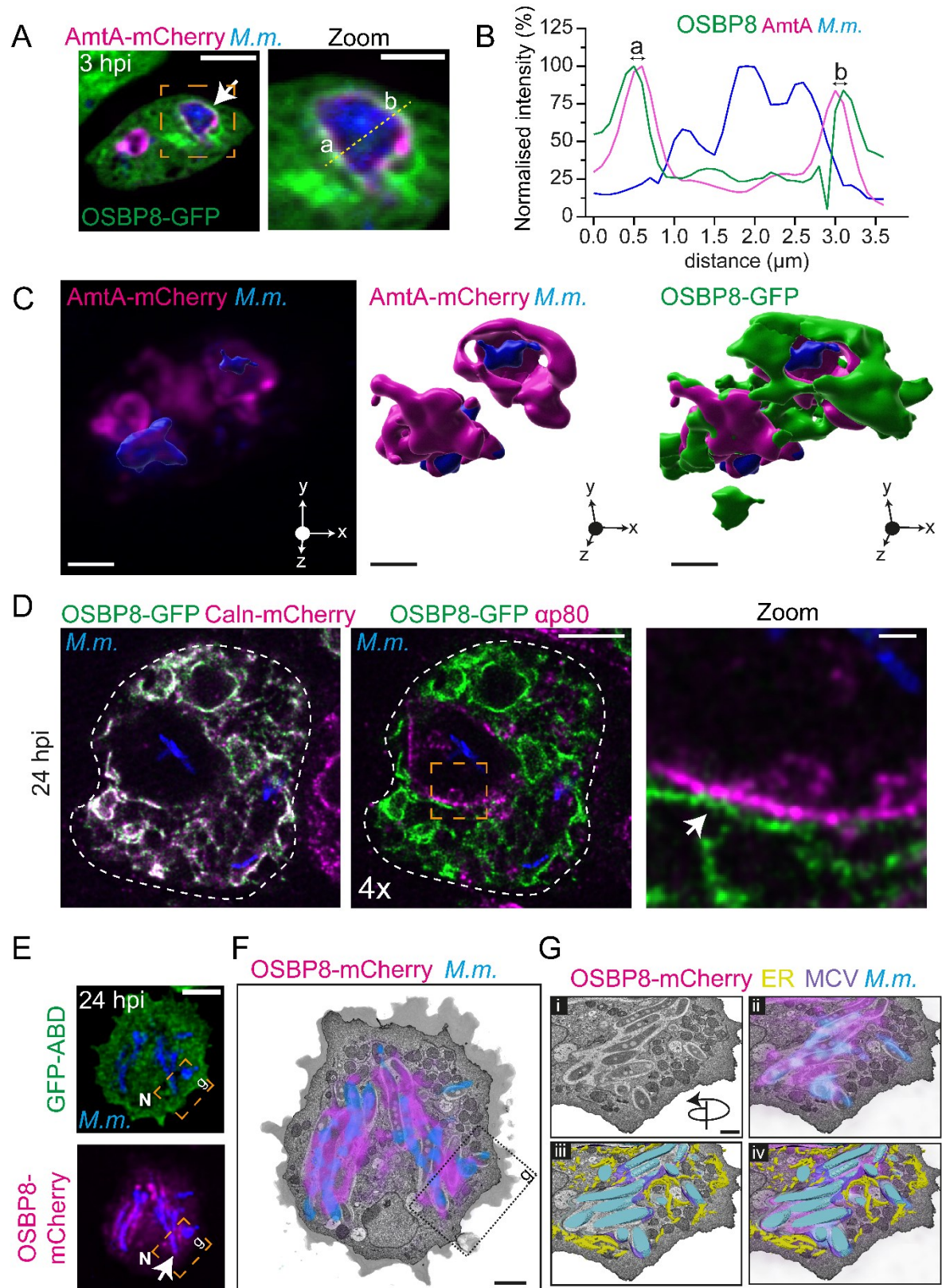
FIG 2 Subcellular localization of OSBP8-GFP during infection. (A) LLSM to monitor OSBP8-GFP close to the MCV. (B) Intensity profile of the line plotted through the MCV shown in the zoom of A. (C) 3D-model of the cell shown in (A) illustrating OSBP8-GFP+ membranes capping the MCV (AmtA+). Cells dually expressing OSBP8-GFP/AmtA-mCherry were infected with

FIG 2 legend continued

eBFP-expressing *M. marinum* and imaged live at 3 hpi by LLSM. Arrow points to OSBP8-GFP$^+$ membranes close to the MCV. Scale bars in A, 5 µm; Zoom, 2 µm; in C, 2 µm. (D) Expansion microscopy to visualize ER-MCV MCS during infection. Cells dually expressing OSBP8-GFP/Calnexin-mCherry were infected with eBFP-expressing *M. marinum*, fixed at 24 hpi and stained with antibodies against p80, GFP and mCherry before 4x expansion. Arrow points to an OSBP8-GFP$^+$ ER-tubule close to the MCV. Scale bar, 20 µm; Zoom, 1 µm. Images were deconvolved. (E) 3D-CLEM to visualize OSBP8-mCherry$^+$ ER-tubules close to the MCV (arrow). Cells expressing OSBP8-mCherry/GFP-ABD were infected with eBFP-expressing *M. marinum*. At 24 hpi, cells were imaged by SD microscopy (E) and prepared for SBF-SEM (F-G). (F) EM micrograph showing the cell with the correlated OSBP8-mCherry and eBFP-*M. marinum* signal. Please see Fig. S3C for more information. (G) Closeup of the position indicated in (E-F) showing ER-tubules close to the MCV. (i-iv) correlation of the (i) EM micrograph (ii) with OSBP8-mCherry (magenta) and mycobacteria (blue), (iii-iv) segmentation of the ER (yellow), MCV (violet) and mycobacteria (cyan). Scale bars, 5 µm (E); 2 µm (F) and 1 µm (G). SD images were deconvolved. N: nucleus.

ESX-1-dependent manner (Fig. S4C-D). We conclude that ESX-1/EsxA-mediated membrane damage triggers the formation of ER-MCV MCS and the recruitment of OSBP8-GFP to these sites.

The recruitment of OSBP8-GFP to damaged lysosomes and the MCV is dependent on PI4P

We analysed the distribution of OSBP8-GFP upon treatment with lysosome disrupting agent Leu-Leu-O-Me (LLOMe) (22) to test whether OSBP8 is recruited as a general response to lysosomal damage. As observed previously, LLOMe induced the formation of ESCRT-III-(GFP-Vps32$^+$) structures at the periphery of lysosomes labelled with fluorescent dextran (Fig. S5A) (6). In mammalian cells, ER-dependent lysosome repair is initiated by the recruitment of PI4K2A leading to an accumulation of PI4P at the damage site and the recruitment of ORPs/OSBPs (11, 12). Also in *D. discoideum*, PI4P, visualized with the PI4P-binding domain (P4C) of the *Legionella* effector SidC (23-25), was rapidly observed on ruptured lysosomes. The kinetics of P4C-GFP associated with damaged lysosomes was slightly delayed compared to GFP-Vps32 (Fig. S5A). Also OSBP8-GFP was mobilized upon sterile damage (Fig. S5A), however, as observed for OSBP in HeLa (11) and U2OS cells (12), the recruitment happened relatively late (20-40 min after LLOMe treatment) and was observed less frequently. In contrast, OSBP7-GFP remained cytosolic and in the nucleus upon LLOMe treatment (Fig. S5A). This implies that OSBP8-GFP$^+$ ER-lysosome contacts were a response to lysosomal damage and that this pathway might be activated after SM- and ESCRT-dependent repair. Intriguingly, the mobilization of OSBP8-GFP was totally abolished in cells highly expressing P4C-mCherry (Fig. S5B), indicating that P4C binds to PI4P with such a high affinity that it displaces OSBP8-GFP. In cells expressing P4C-mCherry at low levels, OSBP8-GFP became
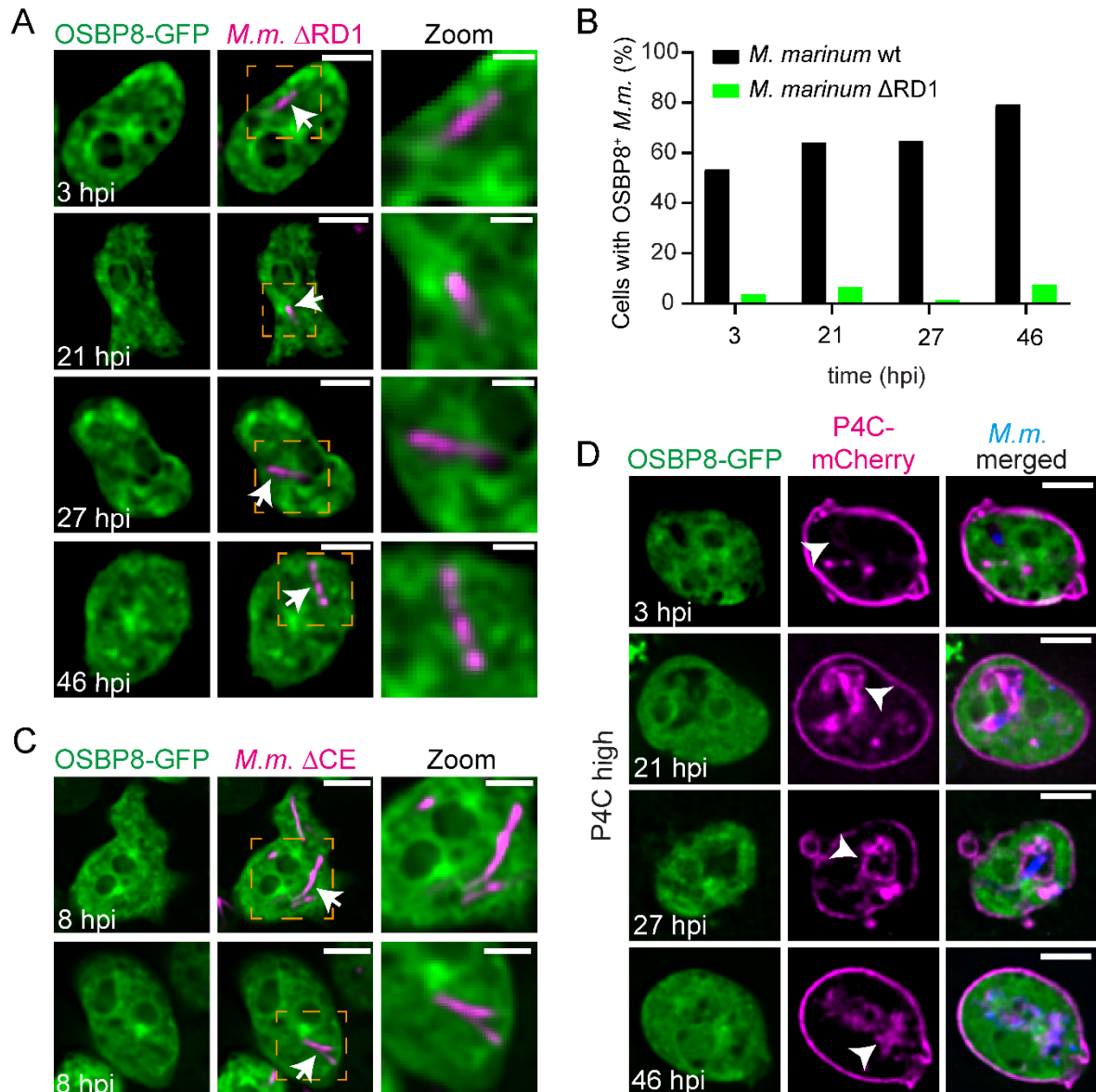
FIG 3 OSBP8-GFP localization during infection with mycobacterial mutants and cells additionally expressing P4C-GFP. (A) Localization of OSBP8-GFP during infection with the *M. marinum* ΔRD1 mutant. (B) Quantification of A. Data represent two independent experiments (OSBP8-GFP 3, 21, 27, 46 hpi N=2, 23≤n≤274). (C) Localization of OSBP8-GFP during infection with the *M. marinum* ΔCE mutant. (D) OSBP8-GFP localization during infection in cells highly expressing P4C-mCherry. Cells overexpressing OSBP8-GFP or co-expressing P4C-mCherry were infected with mCherry- or eBFP- expressing *M. marinum* wt, ΔRD1 or ΔCE. At the indicated time points samples were taken for SD microscopy. Arrows point to OSBP8-GFP⁻ intracellular mycobacteria. Arrow heads indicate PI4P⁺ MCV. Scale bars, 5 μm; Zoom, 2.5 μm. Images were deconvolved. *M.m.: M. marinum.*

visible at the periphery of dextran-labelled endosomes upon LLOMe treatment (Fig. S5C). A similar observation was made during infection: Here, P4C-mCherry accumulated at the MCV starting from early infection stages. In cells highly expressing P4C-mCherry, OSBP8-GFP was not recruited to the MCV (Fig. 3D), indicating that P4C-mCherry competes with OSBP8-GFP

for PI4P. However, when P4C-mCherry was expressed at a low level, OSBP8-GFP co-localized with *M. marinum* (Fig. S5D). Altogether, these data indicate that OSBP8-GFP is recruited by PI4P on damaged lysosomes and on ruptured MCVs.

OSBP8 prevents accumulation of PI4P on damaged MCVs and restricts mycobacterial growth

OSBP8 localizes to the perinuclear ER and the juxtanuclear region that is characteristic for the Golgi apparatus in *D. discoideum* and might be a homologue of mammalian OSBP that is recruited to ER-Golgi contacts to shuttle PI4P and cholesterol between the two organelles (26). In ER-dependent membrane repair, OSBP was reported to balance out PI4P levels on ruptured lysosomes (11). To investigate if OSBP8 is involved in PI4P transport, we generated knockouts (KOs), in which the corresponding gene (*osbH*) is disrupted by a BS^r cassette. Similar to OSBP in mammalian cells, deletion of OSBP8 caused a re-distribution of the PI4P probe away from the PM to internal structures reminiscent of the Golgi apparatus (Fig. S6A-B). Upon LLOMe treatment, P4C-GFP$^+$ lysosomes were detected for up to 110 min in cells lacking OSBP8, whereas the P4C-GFP signal dissociated from lysosomes of wild type (wt) cells considerably earlier (Fig. S6C). Additionally, as observed for OSBP (11), OSBP8 was essential for cell viability following LLOMe treatment, however, the effect was less pronounced compared to cells lacking Tsg101 (Fig. S6D-E). Taken together, our data provide strong evidence that OSBP8 is involved in PI4P-removal from ruptured lysosomes.

During infection, we observed a hyperaccumulation of P4C-GFP on the MCVs of the *osbH* KO (Fig. 4A-B). Previous data by us and others indicate that sterols accumulate in the MCV of *M. marinum* (18) and *M. bovis* BCG (27). To test if OSBP8 depletion interferes with sterol transport, we performed filipin staining. A statistically significant lower filipin intensity was observed on MCVs in *osbH* KO at later infection stages (Fig. 4C-D), suggesting that sterols might indeed be shuttled by OSBP8. Since the difference was small, sterols might be additionally transferred to the MCV by other mechanisms or even other OSBPs. PI4P accumulation on lysosomes of OSBP-depleted cells was hypothesized to induce increased and prolonged ER-endosome contact sites and might impact on lysosomal function (11). During infection approximately half of the bacteria were positive for the peripheral subunit VatB of the H$^+$-ATPase and the MCVs are labelled by LysoSensor and Dye-Quenched (DQ)-BSA at early infection stages (28). While LysoSensor allows to assess the pH of lysosomal compartments, DQ-BSA is used to measure their proteolytic activity. Degradation of DQ-BSA by proteases leads to de-quenching of the fluorescent dye, resulting in an increased fluorescence signal. Remarkably, depletion of OSBP8 lead to a decrease of LysoSensor$^+$ bacteria and to MCVs that are less acidic (Fig. 4E-G). Although the percentage of DQ-BSA$^+$
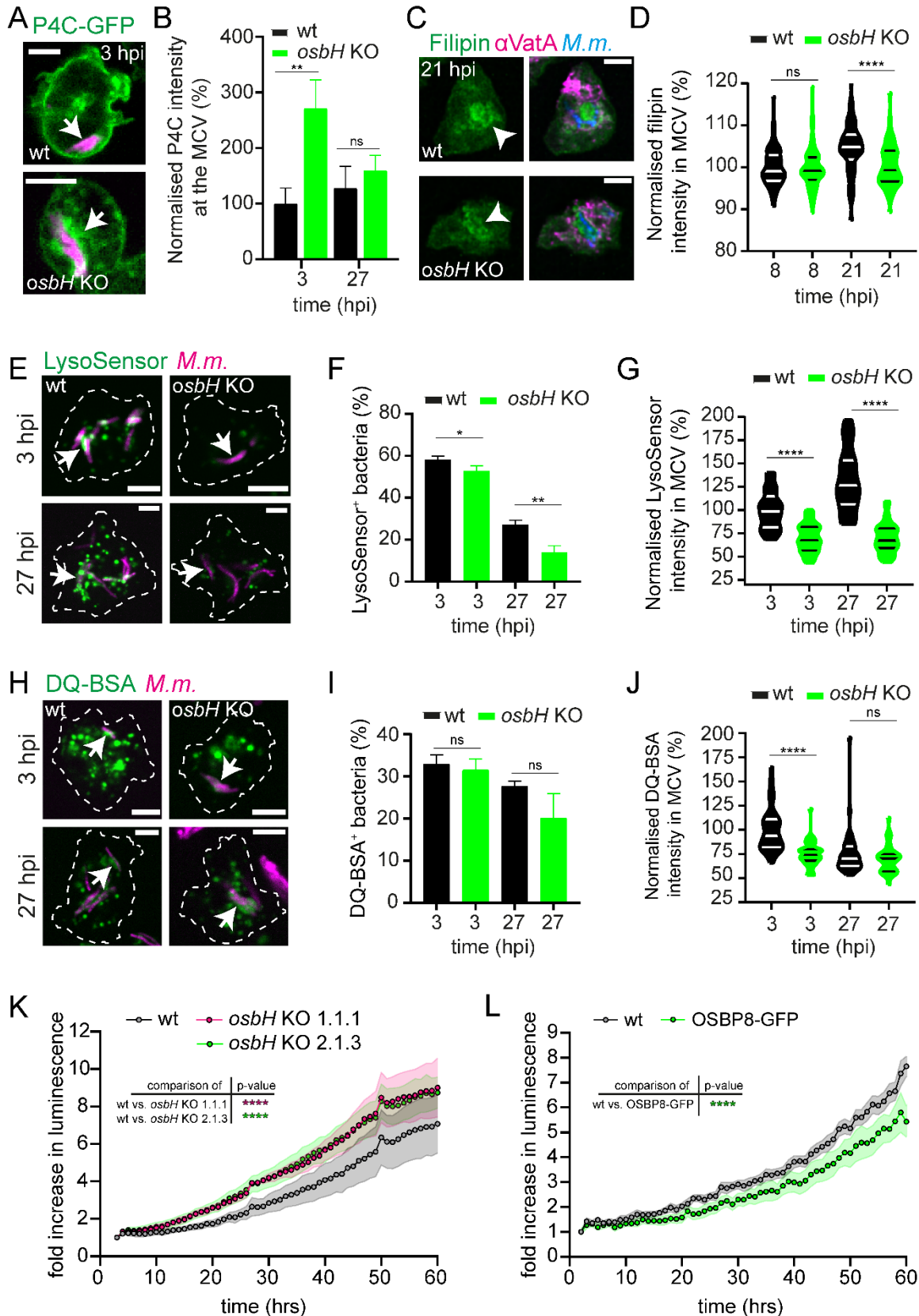
FIG 4 Effect of OSBP8 deletion on PI4P distribution, lysosomal and degradative properties of MCVs and mycobacterial growth. (A) P4C-GFP distribution on MCVs in the *osbH* KO. (B) Quantification of A. Plots show the mean and standard deviation of one of two independent experiments (P4C-GFP 3, 27 hpi N=2, 14≤n≤24). Statistical differences were calculated with

FIG 4 legend continued

an unpaired t-test (**, p < 0.01). (C) Sterol distribution in wt vs. *osbH* KO cells infected with *M. marinum* wt. (D) Quantification of C. Plots show the mean and standard deviation of three independent experiments (Filipin 8, 21 hpi N=3, 30≤n≤70). Statistical differences were calculated with an unpaired t-test (****, p < 0.0001). (E) Lysosomal properties of MCVs in wt vs. *osbH* KO cells. (F-G) Quantifications of E. Plots show the mean and standard deviation of three independent experiments (LysoSensor green 3, 27 hpi N=3, 290≤n≤450). Statistical differences were calculated with an unpaired t-test (*, p < 0.05; **, p < 0.01; ****, p < 0.0001). (H) Proteolytic activity of MCVs in wt vs. *osbH* KO cells. (I-J) Quantification of H. Plots show the mean and standard deviation of three independent experiments (DQ-BSA green 3, 27 hpi N=3, 140≤n≤240). Statistical differences were calculated with an unpaired t-test (****, p < 0.0001). *D. discoideum* wt and *osbH* KO (expressing P4C-GFP (A)) were infected with mCherry- or eBFP-expressing *M. marinum* wt. At the indicated time points samples were taken for SD microscopy. For filipin staining, infected cells were fixed and stained for VatA. Arrows point to PI4P⁺ or LysoSensor⁺ or DQ-BSA⁺ MCV and arrow heads indicate sterol accumulation in the MCV. Scale bars, 5 μm. Images in C were deconvolved. *M.m.: M. marinum.* (K-L) Mycobacterial growth in cells lacking OSBP8 or cells overexpressing OSBP8-GFP. *D. discoideum* wt, two independent *osbH* KOs or OSBP8-GFP overexpressing cells were infected with *M. marinum* wt expressing bacterial luciferase. Luminescence was recorded every hour with a microplate reader. Shown is the fold increase in luminescence over time. Symbols and error bands indicate the mean and standard error of three independent experiments. Statistical differences were calculated with a Tukey post hoc test after two-way ANOVA (****, p < 0.0001).

bacteria was equivalent to wt, MCVs in *osbH* KOs were less degradative (Fig. 4H-J), indicating that the increased accumulation of PI4P impaired the lysosomal and proteolytic capabilities of the MCV. This finding is further supported by the fact that intracellular *M. marinum* growth was increased in two independent *osbH* KOs (Fig. 4K). Conversely, overexpression of OSBP8-GFP lead to reduced intracellular growth (Fig. 4L). Importantly, deletion of OSBP8 did not impact vacuolar escape (Fig. S6F-G) suggesting that the MCV environment is responsible for the growth advantage of the bacteria.

Thus, OSBP8-mediated removal of PI4P from the MCV during ER-dependent membrane repair is necessary to preserve the membrane integrity and the lysosomal functionality of this compartment.

M. tuberculosis recruits OSBP in an ESX-1-dependent manner in human macrophages

Next, we sought to validate our findings in induced pluripotent stem cell (iPSC)-derived macrophages (iPSDMs) infected with *M. tuberculosis* (Fig. 5). According to RNA-sequencing, key genes of this repair pathway were significantly upregulated in an ESX-1-dependent manner (Fig. 5A-B). We observed a higher expression level of *ORP5*, *ORP9* and *PI4K2B,* i.e. another PI-kinase that also localizes to lysosomes (29). This signature was significant at 48 hpi and most of the genes were not upregulated in cells infected with the *M. tuberculosis* ΔRD1 mutant. OSBP transfers cholesterol to damaged lysosomes to preserve membrane stability

and PI4P in the opposite direction to ensure the establishment of functional contact sites (11). Strikingly, during infection of iPSDMs, endogenous OSBP re-localized to *M. tuberculosis* wt (Fig. 5C). Notably, this recruitment is ESX-1-dependent as OSBP was less efficiently recruited in cells infected with *M. tuberculosis* ΔRD1 mutant (Fig. 5D-E). Collectively, our data highlight the evolutionary conservation of an ER-dependent membrane repair mechanism from simple eukaryotes such as *D. discoideum* to human cells.
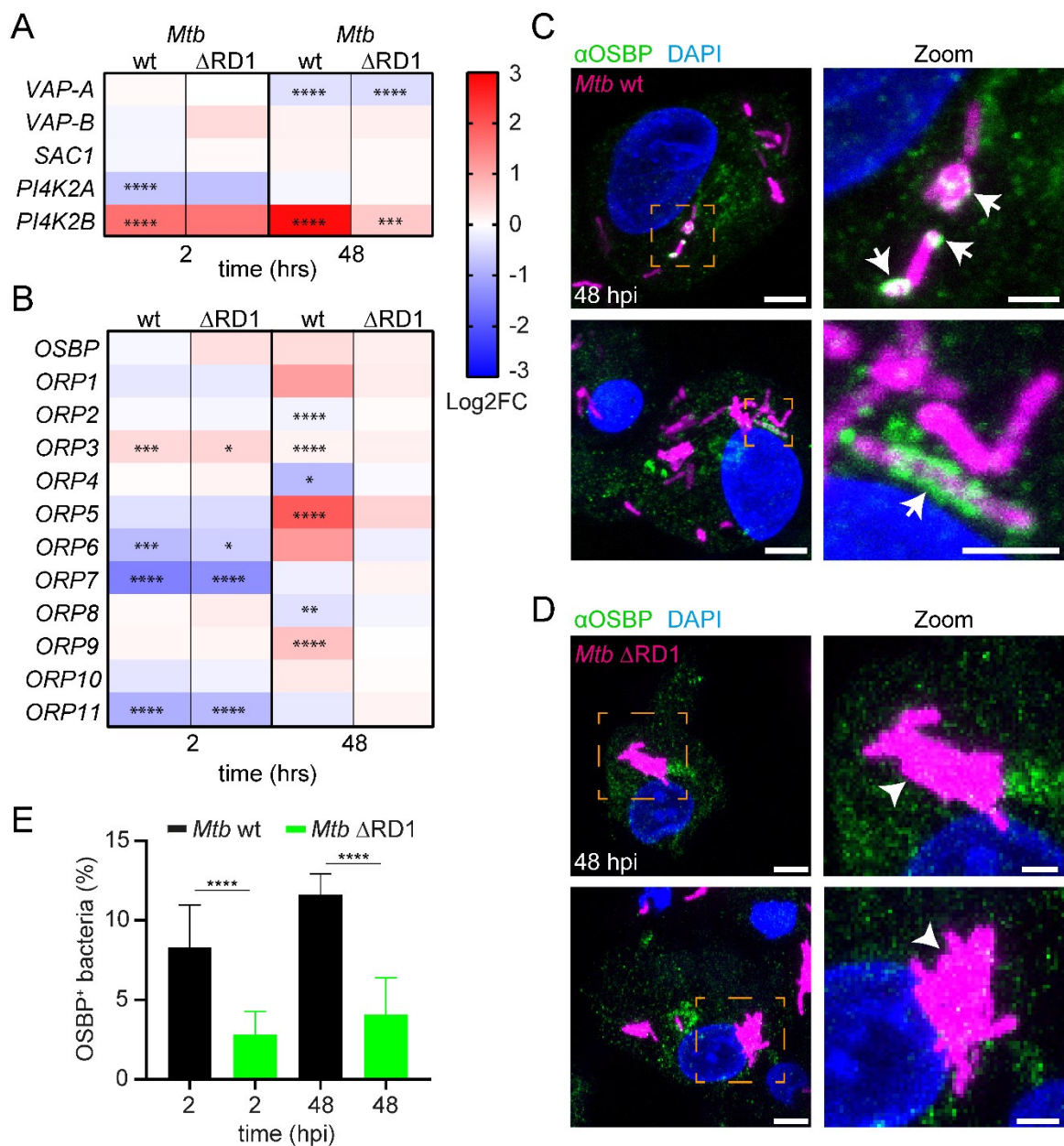

FIG 5 Evidence for ER-mediated repair and OSBP mobilization during *M. tuberculosis* infection. (A-B) Heatmaps of differentially expressed genes (Log2FC) encoding proteins involved in MCS formation from RNA-sequencing analysis of human iPSDMs infected with either *M. tuberculosis* wt or ΔRD1. Data was retrieved from (13). Samples were collected at the indicated time points. Statistically significant differences in expression are marked with asterisk (*, $p < 0.05$; **, $p < 0.01$; ***, $p < 0.001$; ****, $p < 0.0001$). Colours indicate the amplitude

FIG 5 legend continued

of expression (Log2FC) in infected cells compared to mock-infected cells: from red (highest expression) to blue (lowest expression). (C-D) Localization of endogenous OSBP in human iPSDMs upon infection with *M. tuberculosis* wt and the ΔRD1 mutant. iPSDMs were infected with E2-Crimson-expressing wt or RD1 bacteria. At 2 and 48 hpi cells were fixed and stained against OSBP. Shown are two representative images from 48 hpi. Z-stacks: 20, 0.3 *μm.* Arrows and arrowheads point to OSBP8$^+$ or OSBP8$^-$ intracellular bacteria, respectively. Scale bars, 5 μm; Zoom; *2* μm. (E) Quantification of (C-D). Plots show the mean and standard deviation of three independent experiments (OSBP 2, 48 hpi N=3, 800≤n≤1200). Statistical differences were calculated with an unpaired t-test (****, p < 0.0001). Mtb: *M. tuberculosis*.

Discussion

Using transcriptomics and proteomics data of infected cells as well as advanced imaging approaches, we provide evidence that ER-dependent repair is involved in mycobacterial infection. The main features of this membrane repair pathway at MCVs are shown in Fig. 6. Since various genes encoding for PI4Ks are upregulated at later infection stages (Fig. 1A), we hypothesize that cumulative damage at the MCV leads to the recruitment of PI4K. This is consistent with the fact that PI4P accumulated at this compartment (Fig. 3D). The presence of
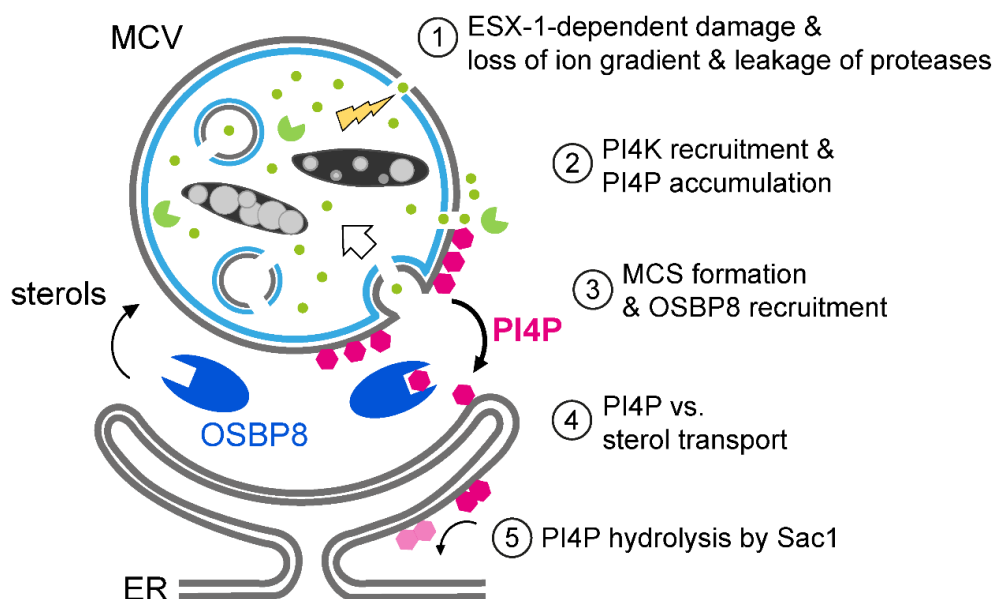

FIG 6 Schematic outline of ER-dependent repair during mycobacterial infection. 1.) ESX1-dependent vacuolar damage (yellow flash) leads to a loss of ion gradients (green spots) and the release of proteases (green packmen). 2.) PI4K are recruited to generate PI4P (pink polygons) at the MCV. 3.) This leads to the establishment of ER-MCV MCS and the mobilization of OSBP8 (blue) in *M. marinum*-infected *D. discoideum*. 4.) OSBP8 transports sterols from the ER to the MCV and PI4P in the opposite direction. 5.) The transport is fuelled by the lipid phosphatase Sac1 that hydrolyses PI4P generating PI (light pink).

PI4P is essential for (i) the formation of MCS via the interaction with PI4P-binding, tethering proteins that might interact with the anchor VAP at the ER and (ii) for the recruitment of LTPs belonging to the OSBP/ORP-family. We suggest that lipid transport is fuelled by a PI4P gradient that is maintained by the PI4P hydrolase Sac1 on the ER. Conversely, an upregulation of Sac1 during infection was observed in *D. discoideum* (Fig. 1A). We propose that the ER-dependent pathway plays a role in providing lipids for other membrane repair mechanisms, including SM- and ESCRT-dependent repair (8). In line with that we also observed an upregulation of *ORP5* and *ORP9* during *M. tuberculosis* infection. The corresponding proteins might transfer PS to the MCV (12, 30). These lipids might be essential for the generation of intraluminal vesicles, which ultimately facilitate the removal of the damage site. To better understand the potential crosstalk between SM-, ESCRT-, and ER-dependent repair mechanisms during infection, further work is necessary.

Besides transferring sterols to the MCV, OSBP8 and mammalian OSBP have a crucial role in equilibrating PI4P levels to ensure the formation of functional ER-MCV MCS. Strikingly, both proteins were recruited to MCVs. Consistent with previous results (6), the kinetics of OSBP8-GFP recruitment (Fig. 3B) correlates with the accumulation of GFP-Vps32 and GFP-Tsg101, i.e. components of ESCRT-dependent repair. Mycobacteria lacking ESX-1 failed to mobilize OSBP in macrophages and OSBP8-GFP in *D. discoideum* (Fig. 5C-E, Fig. 3A-C). Altogether this suggests that membrane damage is likely a prerequisite for OSBP and OSBP8-GFP recruitment. Using advanced imaging approaches such as LLSM, CLEM and 3D-CLEM, we discovered that OSBP8 is on ER-tubules that form MCS with the MCV (Fig. 2, Fig. S3). OSBP8 depletion resulted in the hyperaccumulation of PI4P on MCVs (Fig. 4A-B) and intracellular growth of *M. marinum* was accelerated (Fig. 4K). The observed growth advantage is probably due to the impaired lysosomal function and degradative properties of the MCV in the absence of OSBP8 (Fig. 4E-J). Depletion of OSBP8 did not fully inhibit the accumulation of sterols inside the MCV (Fig. 4C-D). Thus, sterol transport might be mediated either by vesicular transport or even by other OSBPs such as OSBP6 and OSBP12 which were also abundant in the MCV proteome (Fig. 1B).

How is OSBP8 recruited to ER-MCV MCS? Members of the OSBP/ORP family are typically targeted to the ER by binding to VAP through their two phenylalanines-in-an-acidic tract (FFAT)-motif. Sequence analysis revealed that all *D. discoideum* OSBPs are short and contain neither a FFAT-motif, nor pleckstrin homology- (PH-) or transmembrane domains but consist primarily of the ORD (Fig. S1B). OSBP8 has a short amphipathic lipid packing sensor (ALPS)-like motif (31) flanked by an unstructured N-terminus (Fig. S6H). Intriguingly, the presence of an N-terminal GFP-tag prevented membrane targeting of OSBP8 (Fig. S2C-D) suggesting that the ALPS-like motif may be involved in PI4P-binding (Fig. 3D, Fig. S2C-D).

In summary, *D. discoideum* and macrophages restrict pathogenic mycobacteria such as *M. tuberculosis* and *M. marinum* by restoring the MCV membrane with the help of ER-dependent membrane repair. We conclude that PI4P levels at the MCV need to be tightly regulated to allow the correct establishment of ER-MCV MCS to provide adequate levels of lipids to preserve membrane integrity. This in turn is necessary to maintain ion gradients and fundamental innate immune functions of these compartments. Our findings pave the way for an in-depth mechanistic analysis of the role of ER-dependent repair for the formation and stability of pathogen vacuoles.

Materials and Methods

D. discoideum plasmids, strains and cell culture

All the *D. discoideum* material is listed in Table S1. Most of the experiments were conducted using AX2; however, for the experiments presented in Fig. S6D-E, AX2(Kay) was additionally utilized. *D. discoideum* was grown axenically at 22°C in HI5c medium (Formedium) containing 100 U/mL penicillin and 100 µg/mL streptomycin. To generate *osbH* KOs, *osbH* was amplified with the primers #293 (5' CGG AAT TCA AAA TGT TTT CAG GAG CAT TG) and #294 (5' CGG AAT TCT TAA TTT GAA GCT GCT GC) from genomic DNA of AX2 digested with EcoRI and ligated into the same site of pGEM-T-Easy (Promega) to yield plasmid #625. From this plasmid a central 0.3 kbp fragment was eliminated by MfeI and the ends were blunted by T4 DNA polymerase. Thereafter the blasticidin S-resistance cassette flanked by SmaI sites from plasmid pLPBLP (32) was inserted, resulting in plasmid #629. Digestion with EcoRI produced an *osbH* gene interrupted by the BS^r-cassette that was used for electroporation. The *D. discoideum* clones were screened and verified by PCR with #353 (5' CAAT ACC AAT AGA TTT TAT ATC ATT AC) that bound genomic DNA just upstream the construct used for targeting and primers #57 (5' CGC TAC TTC TAC TAA TTC TAG A) complementary to the 5' end of the resistance cassette. Because this primer combination did not yield a product for the wildtype, further verifications involved primers #353 in combination with #358 (5' CCT CTG ATG AGT TAC CAT AG) in the 3' homologous sequence, as well as #357 (5' GCC TCA AAA CAA GAT AGC G) binding in the 5' region of the targeting construct together with #356 (5' CAG CGG AAA TTG AAT GAA TAA ATT) complementary to a sequence downstream of the region used for homologous recombination. The *osbH* KO 1.1.1 and *osbH* KO 2.1.3 strains are two clones that were obtained from two independent electroporations followed by subscreening on bacteria lawns.

The OSBP8::GFP knockin cell line was generated using a previously described strategy (33) with the aim to insert the GFP-tag and the BS^r cassette after the endogenous gene by homologues recombination. To this end, two recombination arms consisting of the last ~ 500 bp of *osbH* (left arm (RA)) and of ~ 500 bp downstream of *osbH* (right arm (RA) were amplified

by PCR using the LA primers (oMIB56: 5'CGA GAT CTG GTT GGT TAG GTG CCG GTC G and oMIB57: 5'GGA CTA GTA TTT GAA GCT GCT GCT TTA ACT CTT TCT TCT C) as well as the RA primers (oMIB101: 5'CGG TCG ACT AAA AAC AAT AAT AAT TAT ATA TTT TAA TCG TAA ACA ATT TAT TCA TTC AAT TTC C and oMIB102: 5'GCG AGC TCG AAA TCT TTG TTG GAG G) and cloned into the plasmid pPI183 (33) using the restriction sites BglII, BcuI (LA) and SalI and SacI (RA). The resulting plasmid pMIB173 was used for electroporation after linearization with PvuII. The *D. discoideum* clones were screened and verified by PCR with the primers oMIB56 (5'CGA GAT CTG GTT GGT TAG GTG CCG GTC G) and oMIB57 (5' GGA CTA GTA TTT GAA GCT GCT GCT TTA ACT CTT TCT TCT C) complementary to the *osbH* gene and the downstream region and by western blot using an anti-GFP antibody.

To create OSBP7- and OSBP8-GFP overexpressing cells, *osbG* and *osbH* were amplified from cDNA using the primers oMIB20 (*osbG* forward 5'CGA GAT CTA AAA TGG AGG CCG ATC CG), oMIB18 (*osbG* reverse with stop 5' CCA CTA GTT TAA TTA CTA CCA CTT GCA GC), oMIB19 (*osbG* reverse without stop 5' CCA CTA GTA TTA CTA CCA CTT GCA GC), oMIB21 (*osbH* forward 5' CGA GAT CTA AAA TGT TTT CAG GAG CAT TG), oMIB23 (*osbH* reverse with stop 5' CCA CTA GTT TAA TTT GAA GCT GCT GC) and oMIB22 (*osbH* reverse without stop 5' CCA CTA GTA TTT GAA GCT GCT GCT TTA AC) and cloned into pDM317 and pDM323 (34) to generate N- and C-terminal GFP-fusions, respectively.

All plasmids used in this study are listed in Table S1. Plasmids were electroporated into *D. discoideum* and selected with the appropriate antibiotic. Hygromycin was used at a concentration of 50 μg/ml, blasticidin at a concentration of 5 µg/ml, and neomycin at a concentration of 5 µg/ml.

SDS-PAGE and western blot

$5x10^5$ cells were harvested and incubated with 2x Laemmli buffer containing ß-mercapto-ethanol and DTT. After the electrophoresis, proteins were transferred to a nitrocellulose membrane (Amersham™ Protran™, Premium 0.45µm NC) as described in (35). Transfer was performed for 50 min and a constant voltage of 120 V on a Mini Trans-Blot Cell (Biorad R) system. The membranes were stained with Ponceau S solution to check the efficiency of the protein transfer. For immunodetection, the membranes were blocked using non-fat dry milk and stained with an anti-GFP primary (Roche; 1:1000) and a goat anti-mouse secondary antibody coupled to horseradish peroxidase (HRP) (BioRad, 1:5000). The detection of HRP was accomplished using the Pierce™ ECL Western Blotting Substrate (Thermo Scientific).

Cell viability assay

Cell viability was assessed by measuring the fraction of propidium iodide$^+$ cells by flow cytometry. To this end, approximately 10^6 cells were harvested and resuspended in Soerensen

buffer (SB). Membrane damage was induced by addition of 5 mM LLOMe and measured in SB buffer containing 3 µM PI (Thermo Fisher Scientific). After one hour of incubation, 10,000 cells per condition were analysed using a SonySH800 and the PE-A channel. Flow cytometry plots were generated with FloJo.

Induced pluripotent stem cell-derived macrophages (iPSDMs) differentiation and cell culture
iPSDMs were generated from human induced pluripotent stem cell line KOLF2 sourced from Public Health England Culture Collections as previously described (13). To collect the cells, iPSDMs were washed in 1x PBS and incubated with Versene (Gibco) for 10 min at 37 °C and 5 % CO_2. Versene was diluted 1:3 in 1x PBS and cells were gently scraped, centrifuged at 300 g, resuspended in X-Vivo 15 (Lonza) supplemented with 2 mM Glutamax (Gibco), 50 µM β-mercaptoethanol (Gibco) and plated for experiments on 96-well CellCarrier™ Ultra glass-bottom plates (Perkin Elmer) at approximately 50,000 cells per well.

Mycobacteria strains, culture and plasmids
All the *M. marinum* material is listed in Table S1. *M. marinum* was cultured in 7H9 supplemented with 10 % OADC, 0.2 % glycerol and 0.05 % Tween-80 at 32 °C at 150 rpm until OD_{600} of 1 (~$1.5x10^8$ bacteria/ml). To prevent bacteria from clumping, flasks containing 5 mm glass beads were used. Luminescent *M. marinum* wt as well as ΔRD1 and ΔCE bacteria expressing mCherry were generated in the Thierry Soldati laboratory (28, 36, 37) and grown in medium supplemented with 25 µg/ml kanamycin and 100 µg/ml hygromycin, respectively. To generate wt and ΔRD1 mycobacteria expressing eBFP, the unlabelled strains were transformed with the pTEC18 plasmid (addgene #30177) and grown in medium with 100 µg/ml hygromycin.
All the *M. tuberculosis* material is listed in Table S1. *M. tuberculosis* were thawed and cultured in Middle 7H9 supplemented with 0.05 % Tween-80, 0.2 % glycerol and 10% ADC.

Infection assays
The infection of *D. discoideum* with *M. marinum* was carried out as previously described (16, 38). Briefly, for a final MOI of 10, 5 x 10^8 bacteria were washed twice and resuspended in 500 µl Hl5c filtered. To remove clumps, bacteria were passed 10 times through a 25-gauge needle and added to a 10 cm petri dish of *D. discoideum* cells. To increase the phagocytosis efficiency, the plates were centrifuged at 500 g for two times 10 min at RT. After 20-30 min incubation, the extracellular bacteria were removed by several washes with Hl5c filtered. Finally, the infected cells were taken up in 30 ml of Hl5c at a density of 1 x 10^6 c/ml supplemented with 5 µg/ml streptomycin and 5 U/ml penicillin to prevent the growth of extracellular bacteria and incubated at 25 °C at 130 rpm. At the indicated time points, samples were taken for downstream experiments.

Infection of iPSDMs was performed as previously described (13). Briefly, *M. tuberculosis* was grown to $OD_{600} \sim 0.8$ and centrifuged at 2000 g for 5 min. The pellet was washed twice with PBS, shaken with 2.5-3.5 mm glass beads for 1 min to produce a single-bacteria suspension. Bacteria were resuspended in 8 ml of cell culture media and centrifuged at 300 g for 5 min to remove clumps. Bacteria were diluted to an MOI of 2 for infection before adding to the cells. After 2 hrs, the inoculum was removed, cells were washed with PBS, and fresh medium was added.

Intracellular growth assays

M. marinum growth was assessed with the help of bacteria expressing luciferase as well as its substrates as previously described (36). Briefly, infected *D. discoideum* cells were plated in dilutions between $0.5 - 2.0 \times 10^5$ on non-treated 96-well plates (X50 LumiNunc, Nunc) and covered with a gas permeable moisture barrier seal (4Ti). Luminescence was measured at 25 °C every hour for around 70 hrs using an Infinite 200 pro M-plex plate reader (Tecan).

RNA-sequencing and proteomic data

RNA-Seq (15) and proteomics data (14) from *M. marinum*-infected *D. discoideum* were re-analysed for selected genes involved in ER-contact site formation or lipid transport. All the data can be accessed via the supplementary files on BioRxiv.

RNA sequencing data of *M. tuberculosis*-infected macrophages was extracted from an original study (13). All RNA-Seq data is deposited in Gene Expression Omnibus (accession number GSE132283).

Live cell imaging

To monitor non-infected cells or the course of infection by SD live imaging, cells were transferred to either 4- or 8-well μ-ibidi slides and imaged in low fluorescent medium (LoFlo, Formedium, UK) with a Zeiss Cell observer spinning disc (SD) microscope using the 63x oil objective (NA 1.46). To improve signal-to-noise, indicated images were deconvolved using Huygens Software from Scientific Volume Imaging (Netherlands).

To analyse whether MCVs have impaired lysosomal or proteolytic function, infected cells were transferred to an ibidi slide and incubated for 10 min in Hl5c filtered medium containing 1μM LysoSensor Green (Thermo Fisher Scientific) or 1 hr with 50 μg/ml DQ-BSA Green (Thermo Fisher Scientific). In the case of LysoSensor Green labelling, the extracellular dye was removed before imaging. Z-stacks of 15 slices with 300 nm intervals were acquired.

To visualize GFP-Vps32, P4C-mCherry, P4C-GFP, OSBP7-GFP and OSBP8-GFP on damaged lysosomes, sterile membrane damage was induced with 5 mM LLOMe (Bachem) as described in (6). To label all endosomes, above mentioned cells were pre-incubated on ibidi

slides overnight with 10 μg/ml dextran (Alexa Fluor™ 647, 10.000 MW, Thermo Fisher Scientific) in Hl5c filtered medium. Time lapse movies of single planes were recorded 10 min prior the addition of LLOMe and then further acquired every 5 min for at least 2 hrs.

For lattice light sheet microscopy (LLSM) the infection was performed as previously described. At 3 hours post infection (hpi) cells were seeded on 5 mm round glass coverslips (Thermo Scientific) and mounted on a sample holder specially designed for LLSM, which was an exact home-built clone of the original designed by the Betzig lab (39). The holder was inserted into the sample bath containing Hl5c filtered medium at RT. A three-channel image stack was acquired in sample scan mode through a fixed light sheet with a step size of 190 nm which is equivalent to a ~189.597 nm slicing. A dithered square lattice pattern generated by multiple Bessel beams using an inner and outer numerical aperture of the excitation objective of 0.48 and 0.55, respectively, was used. The raw data was further processed by using an open-source LLSM post-processing utility called LLSpy v0.4.9 (https://github.com/tlambert03/LLSpy) for deskewing, deconvolution, 3D stack rotation and rescaling. Deconvolution was performed by using experimental point spread functions and is based on the Richardson-Lucy algorithm using 10 iterations. Finally, image data were analysed and processed using ImageJ and 3D surface rendering was performed with Imaris 9.5 (Bitplane, Switzerland).

Antibodies, fluorescent probes, immunofluorescence and expansion microscopy

Fluoresbrite 641 nm Carboxylate Microspheres (1.75 μm) were obtained from Polysciences Inc., LysoSensor Green DND-189 as well as DQ Green BSA, Alexa Fluor 647 10 kDa dextran and FM4-64 from Thermo Fisher Scientific.

The anti-vatA, anti-vacA, anti-p80 antibodies were obtained from the Geneva antibody facility (Geneva, Switzerland). The anti-PDI antibody was provided from the Markus Maniak lab (University of Kassel, Germany). Anti-Ub (FK2) was from Enzo Life Sciences and anti-OSBP antibody from Sigma-Aldrich. As secondary antibodies, goat anti-rabbit, anti-mouse and anti-rat IgG coupled to Alexa546 (Thermo Fisher Scientific), CF488R (Biotium), CF568 (Biotium) or CF640R (Biotium) were used.

For immunostaining of *D. discoideum*, cells were seeded on acid-cleaned poly-L-Lysine coated 10 mm coverslips and centrifuged at 500 g for 10 min at RT. Cells were fixed with 4 % paraformaldehyde/ picric acid and labelled with antibodies as described in (40). Images were acquired using an Olympus LSM FV3000 NLO microscope with a 60x oil objective with a NA of 1.40. Five slices with 500 nm intervals were taken.

Filipin staining was performed as previously described (18). Briefly, fixed cells were treated with Filipin at 50 μg/ml for 2 hrs without further permeabilization prior the primary antibody

60

labelling. To avoid bleaching, images were taken using the SD microscope. Up to 20 slices with 300 nm intervals were obtained.

For immunostaining of infected iPSDMs, cells were fixed overnight with 4 % paraformaldehyde at 4 °C. Samples were quenched with 50 mM NH$_4$Cl for 10 min and then permeabilized with 0.3 % Triton-X for 15 min. After blocking with 3 % BSA for 30 min, samples were incubated with the anti-OSBP antibody for 1 hr at RT. After incubation, the coverslips were washed with PBS, before addition of the secondary antibody (45 min at RT). Nuclei were stained with DAPI. Images were recorded either with a Leica SP8 or an Opera Phenix (Perkin Elmer) with 63x water objective with a NA of 1.15.

The ExM protocol was adapted from (41) and (42). Briefly, cells were fixed with -20 °C cold methanol and stained with antibodies as described before. The signal of mCherry and GFP was enhanced using a rat mAb anti-RFP (Chromotek, 5f8-100) and a rabbit pAb anti-GFP antibody (BIOZOL/MBL, MBL-598), respectively. Samples were then incubated with 1 mM methylacrylic acid-NHS (Sigma Aldrich) in PBS for 1 hr at RT in a 24-well plate. After washing three times with PBS, coverslips were incubated in the monomer solution (8.6 % sodium acrylate, 2.5 % acrylamide, 0.15 % N,N'-methylenebisacrylamide, and 11.7 % NaCl in PBS) for 45 min. This was followed by a 2 hrs incubation in the gelling solution (monomer solution, 4-hydroxy-TEMPO (0.01 %), TEMED (0.2 %) and ammonium persulfate (0.2 %)) inside the humidified gelation chamber at 37 °C. Afterwards, gels were transferred into a 10-cm dish containing the digestion buffer (50 mM Tris, 1 mM EDTA, 0.5 % Triton-X-100, 0.8 M guanidine HCl, and 16 U/ml of proteinase K; pH 8.0) and incubated at 37 °C overnight. For final expansion of the polymer, gels were incubated in deionized water for at least 2.5 hrs. Subsequently, a region of interest was cut out and transferred onto a coverslip coated with poly-L-lysine to prevent movements during the imaging (Olympus LSM FV3000 NLO). Deionized water was used as imaging buffer and to store the samples at 4 °C.

CLEM with high-pressure freezing and freeze substitution
In order to perform CLEM with *D. discoideum*, we followed a previously established protocol (19). Briefly, cells expressing GFP-ABD and AmtA-mCherry or OSBP8-mCherry were seeded on poly-L-lysine coated sapphire discs (3 mm x 0.16 mm*)*. Before seeding cells, a coordinate system was applied on the sapphires by gold sputtering using a coordinate template. Sapphires were dipped into 2 % glutaraldehyde (GA) in HL5c and imaged in 0.5 % GA in HL5c. Directly after acquisition of the LM image using the SD microscope, the sapphire discs were high-pressure frozen with a Compact 03 (M. Wohlwend, Switzerland) high pressure freezer (HPF). For HPF, the sapphire discs were placed with the cells and gold spacer facing onto flat 3 mm-aluminum planchettes (M. Wohlwend GmbH, Switzerland), which were beforehand

dipped into hexadecene (Merck, Germany). The assemblies were thereafter placed into the HPF-holder and were immediately high pressure frozen. The vitrified samples were stored in liquid nitrogen until they were freeze substituted.

For freeze substitution (FS), the aluminum planchettes were opened in liquid nitrogen and separated from the sapphire discs. The sapphire discs were then immersed in substitution solution containing 1 % osmium tetroxide (Electron Microscopy Sciences, Germany), 0.1 % uranyl acetate and 5 % H_2O in anhydrous acetone (VWR, Germany) pre-cooled to −90 °C. The FS was performed in a Leica AFS2 (Leica, Germany) following the protocol of 27 hrs at −90 °C, 12 hrs at −60 °C, 12 hrs at −30 °C and 1 hr at 0 °C, washed 5 times with anhydrous acetone on ice, stepwise embedded in EPON 812 (Roth, Germany) mixed with acetone (30 % EPON, 60 % EPON, 100 % EPON) and finally polymerized for 48 hrs at 60 °C. Ultrathin sections of 70 nm and semithin sections of 250 nm were sectioned with a Leica UC7 ultramicrotome (Leica, Germany) using a Histo diamond- and 35 ° Ultra diamond knife (Diatome, Switzerland). Sections were collected on formvar-coated copper slot grids and post-stained for 30 min with 2 % uranyl acetate and 20 min in 3 % lead citrate and analyzed with a JEM 2100-Plus (JEOL, Germany) operating at 200 kV equipped with a 20 mega pixel CMOS XAROSA camera (EMSIS Germany).

For transmission electron microscopy (TEM) tomography 250 nm thick sections were labelled with 10 nm Protein-A gold fiducials on both sides prior to post-staining. Double tilt series were acquired using the TEMography software (JEOL, Germany) at a JEM 2100-Plus (JEOL, Germany) operating at 200 kV and equipped with a 20-megapixel CMOS XAROSA camera (EMSIS, Muenster, Germany). The nominal magnification was 12000x with a pixel size of 0.79 nm. Double tilt tomograms were reconstructed using the back-projection algorithm in IMOD (43).

Serial block face (SBF) - scanning electron microscopy (SEM)

After SD microscopy in gridded ibidi 8-well chambers, cells were fixed in 2% GA in HL5c. Subsequently, samples were processed via adapted version of the NCMIR rOTO-post-fixation protocol (44) and embedded in hard Epon resin, ensuring pronounced contrast and electron dose resistance for consecutive imaging. All procedures were performed in the ibidi dish. In brief, after fixation, samples were post-fixed in 2 % osmium tetroxide (Electron Microscopy Sciences) and treated with 1.5 % (w/v) potassium ferrocyanide (Riedel de Haen) in Hl5c for 30 min. After washing in ultrapure water, cells were incubated in 1 % (w/v) thiocarbohydrazide (Riedel de Haen) in water for 20 min, followed by an additional 2 % osmication step for 1 hr at RT. Samples were then incubated in 1 % tannic acid in water for 30 min, washed and submerged in 1% aqueous uranyl acetate overnight at 4 °C. Cells were then brought up to 50 °C, washed and incubated in freshly prepared Walton`s lead aspartate (Pb(NO3)2 (Carl-Roth),

L-Aspartate (Serva), KOH (Merck)) for 30 min at 60 °C. Subsequently, cells were dehydrated through a graded ethanol (Carl-Roth) series (50 %, 70 % and 90 %) on ice for 7 min each, before rinsing in anhydrous ethanol twice for 7 min and twice in anhydrous acetone (Carl-Roth) for 10 min at RT. Afterwards, cells were infiltrated in an ascending Epon:acetone mixture (1:3, 1:1, 3:1) for 2 hrs each, before an additional incubation in hard mixture of 100 % Epon 812 (Sigma). Final curation was carried out in hard Epon with 3 % (w/w) Ketjen Black (TAAB) at 60 °C for 48 hrs. Once polymerized, the µ-dish bottom was removed via toluene melting from the resin block leaving behind the embedded cells and finder grid imprint. ROIs were trimmed based on the coordinates (250*250*250 µm³) and the sample blocks were glued to aluminium rivets using two-component conductive silver epoxy adhesive and additionally coated in a 20 nm thick gold layer. The rivet containing the mounted resin block was then inserted into the 3View2XP (Gatan, USA) stage, fitted in a JSM-7200F (JEOL, Japan) FE-SEM, and precisely aligned parallel to the diamond knife-edge. The cells proved to be stable under imaging conditions of 1.2 kV accelerating voltage, high vacuum mode of 10 Pa, utilizing a 30 nm condenser aperture and a positive stage bias of 400 V. Imaging parameters were set to 2 nm pixel size, 1.1 µs dwell time, in between ablation of 30 nm and an image size of 10240x10240 pixels. Overall, an approximate volume of 20x20x7 µm (a 210 slices) was acquired. Image acquisition was controlled via Gatan Digital Micrograph software (Version 3.32.2403.0). Further post processing, including alignment, filtering and segmentations were performed in Microscopy Image Browser (Version 2.7 (45)). Endoplasmic reticulum was traced and segmented manually throughout the entire dataset, whereas bacteria, nucleus and vacuole were annotated semi-automatically via morphological 3D watershed. Correlation of light microscopic and EM datasets was performed in AMIRA (Version 2021.1, Thermo Fisher) by rendering and overlaying both volumes, utilizing GFP and eBFP signal as natural landmarks within the electron micrographs.

Statistical analysis

For a description of the statistical analysis of the RNA-sequencing data, please see the original articles: *D. discoideum*/ *M. marinum*: (15); iPSDM/*M. tuberculosis*: (13). All microscopy images were analysed and processed using ImageJ. Experiments in Fig. 3B, 4F, 4I and S6G were quantified manually. Experiments in Fig. 4B, 4D, 4G and 4J were semi-automatically quantified by measuring the integrated intensity around the bacteria or inside the MCV using MCV markers. Where indicated, data was normalized to wt (100 %). The quantification of the band intensity of the western blot shown in Fig. S4A was analysed with ImageJ. Plots and statistical tests were performed using GraphPad Prism. Plots show standard deviation or standard error of the mean as indicated. Unpaired two-tailed t-tests or two-way ANOVA with a

Tukey multiple comparison ad hoc test was carried out. ns: non-significant, *: p-value < 0.05, **: p-value < 0.01, ***: p-value < 0.001, ****: p-value < 0.0001. "N" indicates the number of independent biological replicates, "n" the number of single cells that were quantified.

Acknowledgments

Conflict of interests

The authors declare that they have no conflict of interest.

Table S1 Material used in this publication.

D. discoideum Strains	Relevant characteristics	Source/Reference
Ax2	wt, parental strain of *osbH* KO, *osbH* KI	
Ax2 *osbH* KO	Bsr[r]	This study
Ax2(Ka)	wt, parental strain of *tsg101* KO	
Ax2(Ka) *tsg101* KO	Bsr[r]	(21)
D. discoideum Plasmids		**Source/Reference**
OSBP8-GFP	pDM323-*osbH*, G418[r], Amp[r]	This study
GFP-OSBP8	pDM317-*osbH*, G418[r], Amp[r]	This study
Calnexin-mCherry	pDM1044-*Calnx*, Hyg[r], Amp[r]	(23)
ZntD-mCherry	pDM1044-*zntD*, Hyg[r], Amp[r]	(21)
AmtA-mCherry	pDM1044-*amtA*, Hyg[r], Amp[r]	(18)
OSBP8-mCherry	pDM1210-*osbH*, Hyg[r], Amp[r]	This study
OSBP7-GFP	pDM323-*osbG*, G418[r], Amp[r]	This study
P4C-mCherry	pDM1044-*p4c*, Hyg[r], Amp[r]	(20),(23)
P4C-GFP	pDM323-*p4c*, G418[r], Amp[r]	(46)
GFP-Vps32	pDM317-*vps32*, G418[r], Amp[r]	(6)
OSBP8::GFP	pPI183-osbH, Hyg[r], Amp[r]	This study
GFP-ABD	pDXA-GFP-ABD120, G418[r], Amp[r]	(47)
Mammalian cells	**Relevant characteristics**	**Source/Reference**
Human induced pluripotent stem cell-derived macrophages (iPSDMs)	iPSDMs were generated from human induced pluripotent stem cell line KOLF2	Public Health England Culture Collections (catalogue number 77650100)
***M. marinum* material**		
***M. marinum* M**	wt, parental strain	L. Ramakrishnan (University of Cambridge)
***M. marinum* ΔRD1**	RD1 locus deletion mutant	L. Ramakrishnan (University of Cambridge) (48)
***M. marinum* ΔCE**	*esxA* and *esxB* deletion mutant	T. Soldati (University of Geneva) (28)
***M. tuberculosis* material**		
M. tuberculosis	H37Rv	Douglas Young (The Francis Crick Institute, London, UK), (13)
***M. tuberculosis* ΔRD1**	H37Rv ΔRD1	Suzie Hingley-Wilson (University of Surrey, Guilford, UK), (13)
Mycobacteria Plasmids		
pTEC18	eBFP2 under control of the MSP promoter, Hyg[r], Amp[r]	Addgene #30177(49)
pCherry10	mCherry under control of the G13 promoter, Hyg[r], Amp[r]	Addgene #24664 (50)
pTEC19	E2-Crimson under the control of the MSP promotor, Hyg[r], Amp[r]	Addgene #30178 (49)

References

1. Uribe-Querol E, Rosales C. 2017. Control of Phagocytosis by Microbial Pathogens. Front Immunol 8:1368.

2. Hanna N, Koliwer-Brandl H, Lefrançois LH, Kalinina V, Cardenal-Muñoz E, Appiah J, Leuba F, Gueho A, Hilbi H, Soldati T, Barisch C. 2021. Zn(2+) Intoxication of Mycobacterium marinum during Dictyostelium discoideum Infection Is Counteracted by Induction of the Pathogen Zn(2+) Exporter CtpC. mBio 12.

3. Stinear TP, Seemann T, Harrison PF, Jenkin GA, Davies JK, Johnson PD, Abdellah Z, Arrowsmith C, Chillingworth T, Churcher C, Clarke K, Cronin A, Davis P, Goodhead I, Holroyd N, Jagels K, Lord A, Moule S, Mungall K, Norbertczak H, Quail MA, Rabbinowitsch E, Walker D, White B, Whitehead S, Small PL, Brosch R, Ramakrishnan L, Fischbach MA, Parkhill J, Cole ST. 2008. Insights from the complete genome sequence of Mycobacterium marinum on the evolution of Mycobacterium tuberculosis. Genome Res 18:729-41.

4. Cardenal-Munoz E, Barisch C, Lefrancois LH, Lopez-Jimenez AT, Soldati T. 2017. When Dicty Met Myco, a (Not So) Romantic Story about One Amoeba and Its Intracellular Pathogen. Front Cell Infect Microbiol 7:529.

5. Foulon M, Listian SA, Soldati T, Barisch C. 2022. Chapter 6 - Conserved mechanisms drive host-lipid access, import, and utilization in Mycobacterium tuberculosis and M. marinum, p 133-161. *In* Fatima Z, Canaan S (ed), Biology of Mycobacterial Lipids doi:https://doi.org/10.1016/B978-0-323-91948-7.00011-7. Academic Press.

6. López-Jiménez AT, Cardenal-Muñoz E, Leuba F, Gerstenmaier L, Barisch C, Hagedorn M, King JS, Soldati T. 2018. The ESCRT and autophagy machineries cooperate to repair ESX-1-dependent damage at the Mycobacterium-containing vacuole but have opposite impact on containing the infection. PLoS Pathog 14:e1007501.

7. Raykov L, Mottet M, Nitschke J, Soldati T. 2022. A TRAF-like E3 ubiquitin ligase TrafE coordinates endolysosomal damage response and cell-autonomous immunity to Mycobacterium marinum. bioRxiv doi:10.1101/2021.06.29.450281:2021.06.29.450281.

8. Barisch C, Holthuis JCM, Cosentino K. 2023. Membrane damage and repair: a thin line between life and death. Biological Chemistry doi:doi:10.1515/hsz-2022-0321.

9. Ellison CJ, Kukulski W, Boyle KB, Munro S, Randow F. 2020. Transbilayer Movement of Sphingomyelin Precedes Catastrophic Breakage of Enterobacteria-Containing Vacuoles. Curr Biol 30:2974-2983.e6.

10. Niekamp P, Scharte F, Sokoya T, Vittadello L, Kim Y, Deng Y, Südhoff E, Hilderink A, Imlau M, Clarke CJ, Hensel M, Burd CG, Holthuis JCM. 2022. Ca(2+)-activated sphingomyelin scrambling and turnover mediate ESCRT-independent lysosomal repair. Nat Commun 13:1875.

11. Radulovic M, Wenzel EM, Gilani S, Holland LK, Lystad AH, Phuyal S, Olkkonen VM, Brech A, Jäättelä M, Maeda K, Raiborg C, Stenmark H. 2022. Cholesterol transfer via endoplasmic reticulum contacts mediates lysosome damage repair. Embo j 41:e112677.

12. Tan JX, Finkel T. 2022. A phosphoinositide signalling pathway mediates rapid lysosomal repair. Nature 609:815-821.

13. Bernard EM, Fearns A, Bussi C, Santucci P, Peddie CJ, Lai RJ, Collinson LM, Gutierrez MG. 2020. M. tuberculosis infection of human iPSC-derived macrophages reveals complex membrane dynamics during xenophagy evasion. J Cell Sci 134.

14. Guého A, Bosmani C, Soldati T. 2019. Proteomic characterization of the Mycobacterium marinum-containing vacuole in Dictyostelium discoideum. bioRxiv doi:10.1101/592717:592717.

15. Hanna N, Burdet F, Melotti A, Bosmani C, Kicka S, Hilbi H, Cosson P, Pagni M, Soldati T. 2019. Time-resolved RNA-seq profiling of the infection of Dictyostelium discoideum by Mycobacterium marinum reveals an integrated host response to damage and stress. bioRxiv doi:10.1101/590810:590810.

16. Hagedorn M, Soldati T. 2007. Flotillin and RacH modulate the intracellular immunity of Dictyostelium to Mycobacterium marinum infection. Cell Microbiol 9:2716-33.

17. Tailleux L, Neyrolles O, Honoré-Bouakline Sp, Perret E, Sanchez Fo, Abastado J-P, Lagrange PH, Gluckman JC, Rosenzwajg M, Herrmann J-L. 2003. Constrained Intracellular Survival of Mycobacterium tuberculosis in Human Dendritic Cells 1. The Journal of Immunology 170:1939-1948.

18. Barisch C, Paschke P, Hagedorn M, Maniak M, Soldati T. 2015. Lipid droplet dynamics at early stages of Mycobacterium marinum infection in Dictyostelium. Cell Microbiol 17:1332-49.

19. Franzkoch R, Anand A, Breitsprecher L, Psathaki OE, Barisch C. 2023. Resolving exit strategies of mycobacteria by combining high-pressure freezing with 3D-correlative light and electron microscopy. bioRxiv doi:10.1101/2023.04.24.538041:2023.04.24.538041.

20. Vormittag S, Hüsler D, Haneburger I, Kroniger T, Anand A, Prantl M, Barisch C, Maaß S, Becher D, Letourneur F, Hilbi H. 2023. Legionella- and host-driven lipid flux at LCV-ER membrane contact sites promotes vacuole remodeling. EMBO Rep doi:10.15252/embr.202256007:e56007.

21. Barisch C, Kalinina V, Lefrançois LH, Appiah J, López-Jiménez AT, Soldati T. 2018. Localization of all four ZnT zinc transporters in Dictyostelium and impact of ZntA and ZntB knockout on bacteria killing. J Cell Sci 131.

22. Repnik U, Borg Distefano M, Speth MT, Ng MYW, Progida C, Hoflack B, Gruenberg J, Griffiths G. 2017. L-leucyl-L-leucine methyl ester does not release cysteine cathepsins to the cytosol but inactivates them in transiently permeabilized lysosomes. J Cell Sci 130:3124-3140.

23. Steiner B, Swart AL, Welin A, Weber S, Personnic N, Kaech A, Freyre C, Ziegler U, Klemm RW, Hilbi H. 2017. ER remodeling by the large GTPase atlastin promotes vacuolar growth of Legionella pneumophila. EMBO Rep 18:1817-1836.

24. Weber SS, Ragaz C, Reus K, Nyfeler Y, Hilbi H. 2006. Legionella pneumophila exploits PI(4)P to anchor secreted effector proteins to the replicative vacuole. PLoS Pathog 2:e46.

25. Ragaz C, Pietsch H, Urwyler S, Tiaden A, Weber SS, Hilbi H. 2008. The Legionella pneumophila phosphatidylinositol-4 phosphate-binding type IV substrate SidC recruits endoplasmic reticulum vesicles to a replication-permissive vacuole. Cell Microbiol 10:2416-33.

26. Mesmin B, Bigay J, Polidori J, Jamecna D, Lacas-Gervais S, Antonny B. 2017. Sterol transfer, PI4P consumption, and control of membrane lipid order by endogenous OSBP. Embo j 36:3156-3174.

27. Fineran P, Lloyd-Evans E, Lack NA, Platt N, Davis LC, Morgan AJ, Hoglinger D, Tatituri RV, Clark S, Williams IM, Tynan P, Al Eisa N, Nazarova E, Williams A, Galione A, Ory DS, Besra GS, Russell DG, Brenner MB, Sim E, Platt FM. 2016. Pathogenic mycobacteria achieve cellular persistence by inhibiting the Niemann-Pick Type C disease cellular pathway. Wellcome Open Res 1:18.

28. Cardenal-Munoz E, Arafah S, Lopez-Jimenez AT, Kicka S, Falaise A, Bach F, Schaad O, King JS, Hagedorn M, Soldati T. 2017. Mycobacterium marinum antagonistically induces an autophagic response while repressing the autophagic flux in a TORC1- and ESX-1-dependent manner. PLoS Pathog 13:e1006344.

29. Nakatsu F, Kawasaki A. 2021. Functions of Oxysterol-Binding Proteins at Membrane Contact Sites and Their Control by Phosphoinositide Metabolism. Front Cell Dev Biol 9:664788.

30. Chung J, Torta F, Masai K, Lucast L, Czapla H, Tanner LB, Narayanaswamy P, Wenk MR, Nakatsu F, De Camilli P. 2015. INTRACELLULAR TRANSPORT. PI4P/phosphatidylserine countertransport at ORP5- and ORP8-mediated ER-plasma membrane contacts. Science 349:428-32.

31. Drin G, Casella JF, Gautier R, Boehmer T, Schwartz TU, Antonny B. 2007. A general amphipathic alpha-helical motif for sensing membrane curvature. Nat Struct Mol Biol 14:138-46.

32. Faix J, Kreppel L, Shaulsky G, Schleicher M, Kimmel AR. 2004. A rapid and efficient method to generate multiple gene disruptions in Dictyostelium discoideum using a single selectable marker and the Cre-loxP system. Nucleic Acids Res 32:e143.

33. Paschke P, Knecht DA, Williams TD, Thomason PA, Insall RH, Chubb JR, Kay RR, Veltman DM. 2019. Genetic Engineering of Dictyostelium discoideum Cells Based on Selection and Growth on Bacteria. J Vis Exp doi:10.3791/58981.

34. Veltman DM, Akar G, Bosgraaf L, Van Haastert PJ. 2009. A new set of small, extrachromosomal expression vectors for Dictyostelium discoideum. Plasmid 61:110-8.

35. Towbin H, Staehelin T, Gordon J. 1979. Electrophoretic transfer of proteins from polyacrylamide gels to nitrocellulose sheets: procedure and some applications. Proc Natl Acad Sci U S A 76:4350-4.

36. Arafah S, Kicka S, Trofimov V, Hagedorn M, Andreu N, Wiles S, Robertson B, Soldati T. 2013. Setting up and monitoring an infection of Dictyostelium discoideum with mycobacteria, p 403-17. In Eichinger L, Rivero F (ed), Dictyostelium Protocols (Methods Mol Bio), vol 983. Humana Press.

37. Kicka S, Trofimov V, Harrison C, Ouertatani-Sakouhi H, McKinney J, Scapozza L, Hilbi H, Cosson P, Soldati T. 2014. Establishment and validation of whole-cell based fluorescence assays to identify anti-mycobacterial compounds using the Acanthamoeba castellanii-Mycobacterium marinum host-pathogen system. PLoS One 9:e87834.

38. Barisch C, Lopez-Jimenez AT, Soldati T. 2015. Live Imaging of Mycobacterium marinum Infection in Dictyostelium discoideum. Methods Mol Biol 1285:369-85.

39. Chen BC, Legant WR, Wang K, Shao L, Milkie DE, Davidson MW, Janetopoulos C, Wu XS, Hammer JA, 3rd, Liu Z, English BP, Mimori-Kiyosue Y, Romero DP, Ritter AT, Lippincott-Schwartz J, Fritz-Laylin L, Mullins RD, Mitchell DM, Bembenek JN, Reymann AC, Böhme R, Grill SW, Wang JT, Seydoux G, Tulu US, Kiehart DP, Betzig E. 2014. Lattice light-sheet microscopy: imaging molecules to embryos at high spatiotemporal resolution. Science 346:1257998.

40. Hagedorn M, Neuhaus EM, Soldati T. 2006. Optimized fixation and immunofluorescence staining methods for Dictyostelium cells. Methods Mol Biol 346:327-38.

41. Chen F, Tillberg PW, Boyden ES. 2015. Optical imaging. Expansion microscopy. Science 347:543-8.

42. Chozinski TJ, Halpern AR, Okawa H, Kim HJ, Tremel GJ, Wong RO, Vaughan JC. 2016. Expansion microscopy with conventional antibodies and fluorescent proteins. Nat Methods 13:485-8.

43. Kremer JR, Mastronarde DN, McIntosh JR. 1996. Computer visualization of three-dimensional image data using IMOD. J Struct Biol 116:71-6.

44. Deerinck T, Bushong E, Lev-Ram V, Shu X, Tsien R, Ellisman M. 2010. Enhancing Serial Block-Face Scanning Electron Microscopy to Enable High Resolution 3-D Nanohistology of Cells and Tissues. Microscopy and Microanalysis 16:1138-1139.

45. Belevich I, Joensuu M, Kumar D, Vihinen H, Jokitalo E. 2016. Microscopy Image Browser: A Platform for Segmentation and Analysis of Multidimensional Datasets. PLOS Biology 14:e1002340.

46. Welin A, Weber S, Hilbi H. 2018. Quantitative Imaging Flow Cytometry of Legionella-Infected Dictyostelium Amoebae Reveals the Impact of Retrograde Trafficking on Pathogen Vacuole Composition. Appl Environ Microbiol 84.

47. Pang KM, Lee E, Knecht DA. 1998. Use of a fusion protein between GFP and an actin-binding domain to visualize transient filamentous-actin structures. Curr Biol 8:405-8.

48. Volkman HE, Clay H, Beery D, Chang JC, Sherman DR, Ramakrishnan L. 2004. Tuberculous granuloma formation is enhanced by a mycobacterium virulence determinant. PLoS Biol 2:e367.

49. Takaki K, Davis JM, Winglee K, Ramakrishnan L. 2013. Evaluation of the pathogenesis and treatment of Mycobacterium marinum infection in zebrafish. Nat Protoc 8:1114-24.

50. Carroll P, Schreuder LJ, Muwanguzi-Karugaba J, Wiles S, Robertson BD, Ripoll J, Ward TH, Bancroft GJ, Schaible UE, Parish T. 2010. Sensitive detection of gene expression in mycobacteria under replicating and non-replicating conditions using optimized far-red reporters. PLoS One 5:e9823.
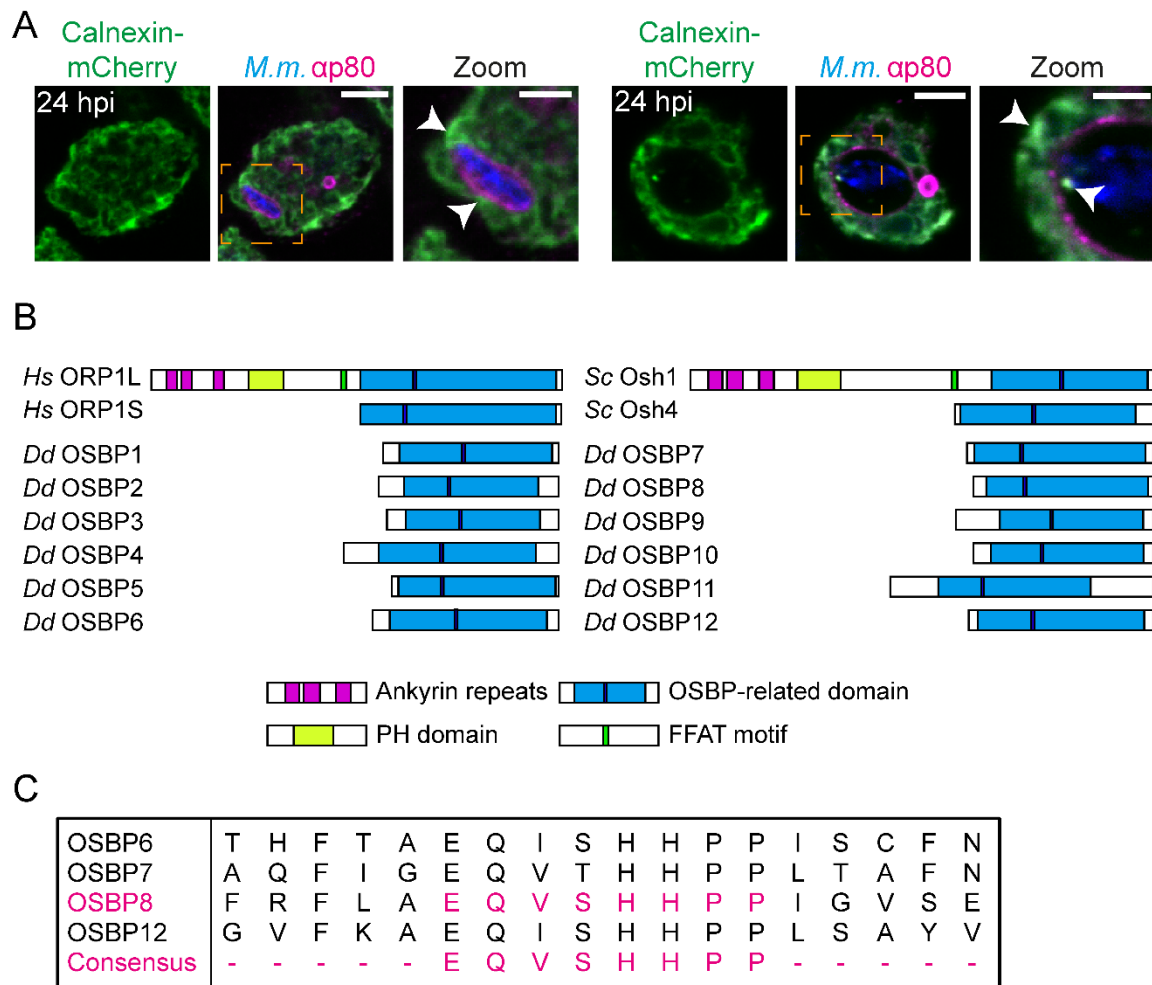
SUPPLEMENTAL MATERIAL

A

Calnexin-mCherry | *M.m.* αp80 | Zoom | Calnexin-mCherry | *M.m.* αp80 | Zoom

24 hpi

B

Hs ORP1L | *Sc* Osh1
Hs ORP1S | *Sc* Osh4
Dd OSBP1 | *Dd* OSBP7
Dd OSBP2 | *Dd* OSBP8
Dd OSBP3 | *Dd* OSBP9
Dd OSBP4 | *Dd* OSBP10
Dd OSBP5 | *Dd* OSBP11
Dd OSBP6 | *Dd* OSBP12

Ankyrin repeats   OSBP-related domain
PH domain   FFAT motif

C

OSBP6	T	H	F	T	A	E	Q	I	S	H	H	P	P	I	S	C	F	N
OSBP7	A	Q	F	I	G	E	Q	V	T	H	H	P	P	L	T	A	F	N
OSBP8	F	R	F	L	A	E	Q	V	S	H	H	P	P	I	G	V	S	E
OSBP12	G	V	F	K	A	E	Q	I	S	H	H	P	P	L	S	A	Y	V
Consensus	-	-	-	-	-	E	Q	V	S	H	H	P	P	-	-	-	-	-

FIG S1 Mycobacterial infection induces ER-MCV contacts. (A) ER in apposition with the MCV. Representative images of cells showing Calnexin-mCherry+ ER-tubules close to the MCV (arrow heads). Cells were infected with eBFP-expressing *M. marinum*. At 24 hpi cells were fixed and stained for p80 to label the membrane of the MCV. Scale bars, 5 µm; Zoom, 2 µm. (B) Domain organization of OSBPs in *D. discoideum* (*Dd*) compared to long (ORP1L, Osh1) and short ORP family members from *Homo sapiens* (*Hs*) and *Saccharomyces cerevisiae* (*Sc*) (ORP1S, Osh4). PH: pleckstrin homology; FFAT: two phenylalanines (FF) in an acidic tract. (C) Conserved fingerprint sequence of *D. discoideum* OSBPs.
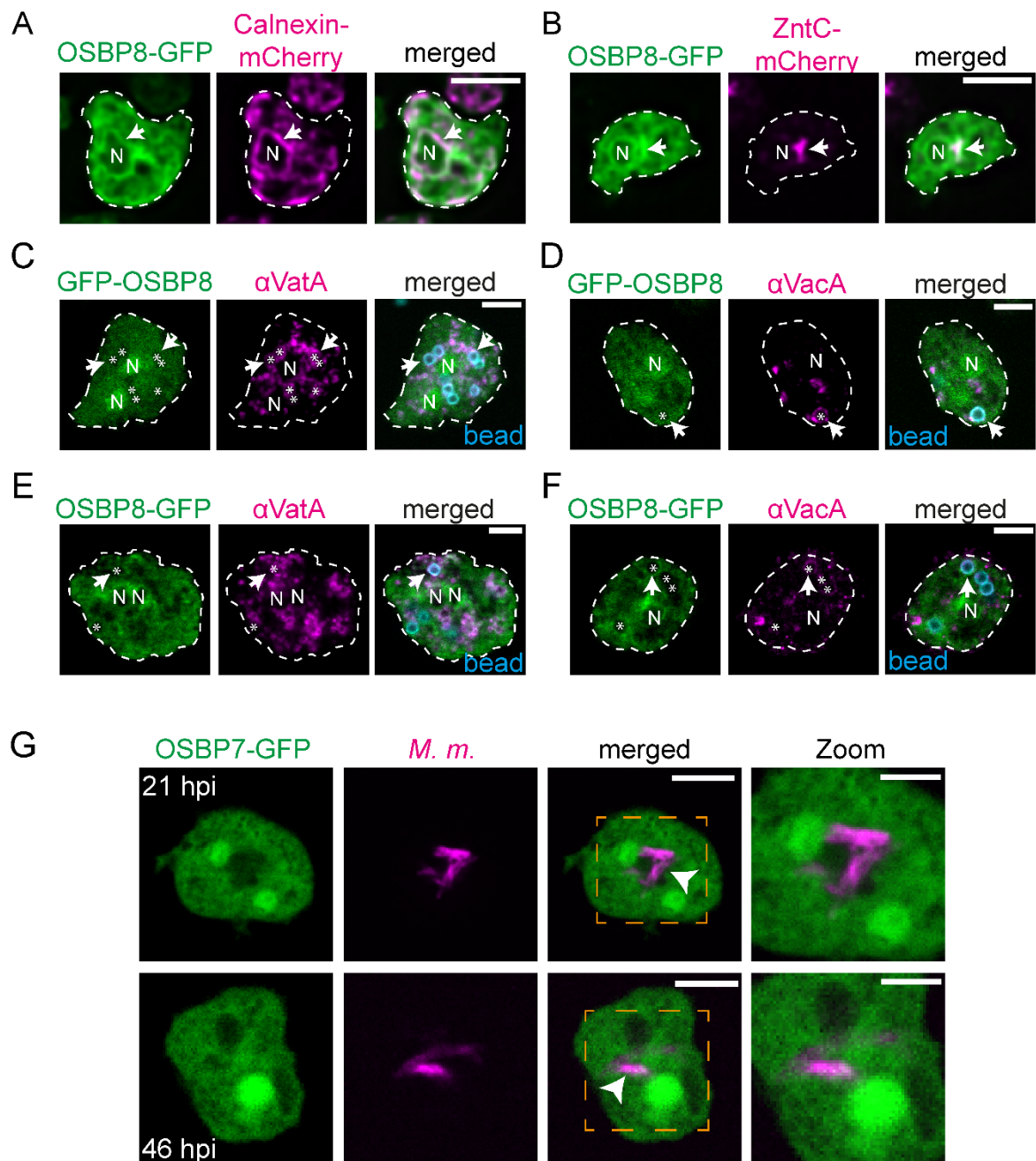
FIG S2 Localization of OSBP8 in non-infected cells and of OSBP7 in infected cells. (A-B) Subcellular localization of OSBP8-GFP. Cells overexpressing OSBP8-GFP/Calnexin-mCherry or OSBP8-GFP/ZntC-mCherry were imaged live by SD microscopy. Arrow points to the juxtanuclear region or the Golgi-apparatus. Scale bars, 5 µm. Images were deconvolved. (C-D) Subcellular localization of GFP-OSBP8. (E-F) OSBP8-GFP localization on BCPs. Cells overexpressing OSBP8-GFP or GFP-OSBP8 were incubated with fluorobeads for 2 hrs, fixed and then stained with αVatA (vATPase subunit A, lysosomes) and αVacA (VacuolinA, post-lysosomes) antibodies. Arrows point to VatA+ or VacA+ BCPs. Asterisks indicate fluorobeads, N: nucleus. Scale bars, 5 µm. (G) Mobilization of OSBP7-GFP upon infection. Cells overexpressing OSBP7-GFP were infected with mCherry-expressing *M. marinum*. At the indicated time points, cells were imaged live by SD microscopy. Arrow heads indicate OSBP7-GFP- mycobacteria. Scale bars, 5 µm; Zoom, 2 µm.
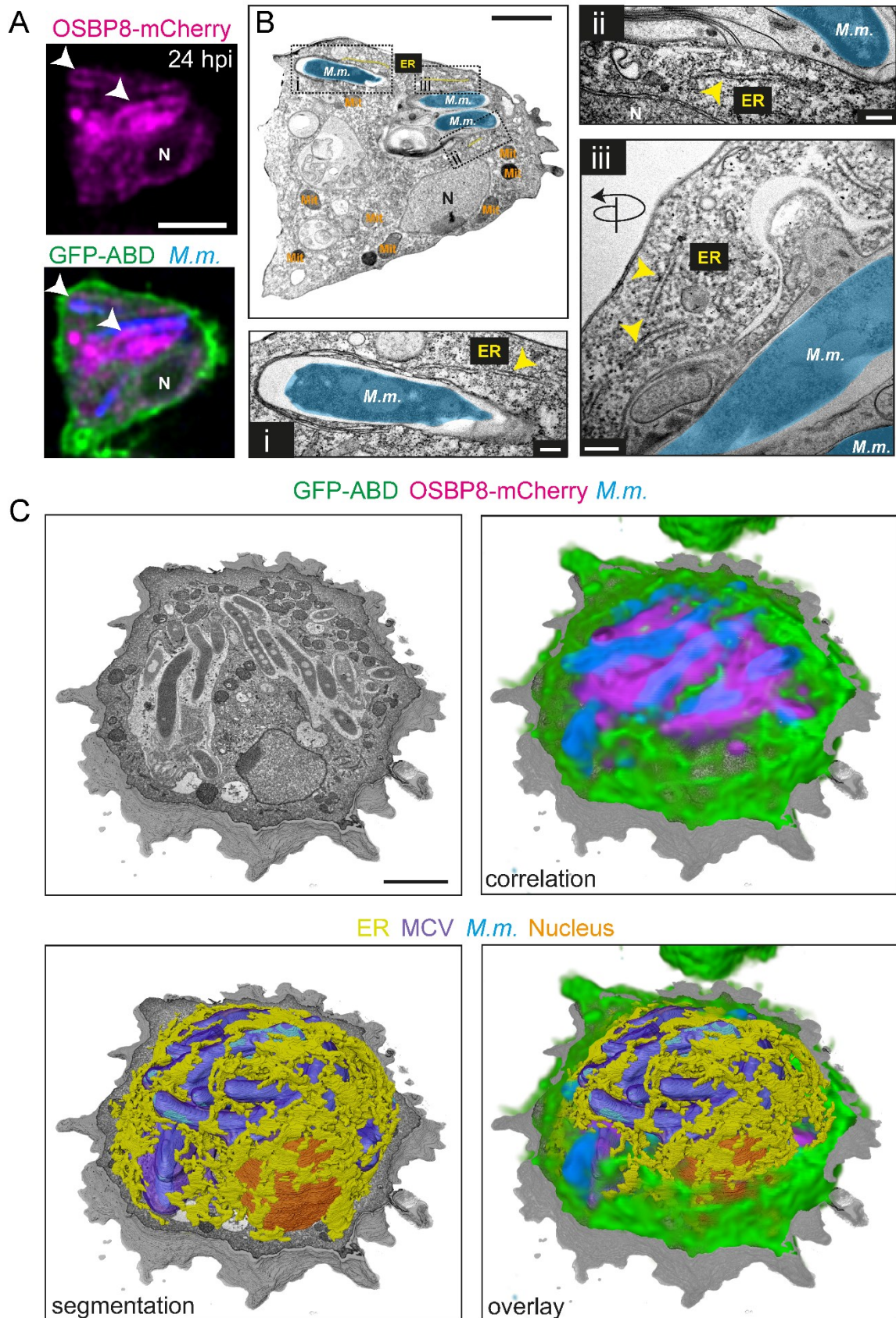
FIG S3 Correlative ultrastructural analysis to monitor OSBP8-mCherry⁺ ER-tubules in close proximity to the MCV. (A-B) CLEM images showing OSBP8-mCherry at ER-MCV contacts (white arrow heads). Cells expressing OSBP8-mCherry/GFP-ABD were infected with eBFP-

FIG S3 legend continued

expressing *M. marinum*. At 24 hpi, cells were imaged after quick fixation by SD microscopy (A), high pressure frozen and prepared for EM (B). Positions of the closeups are indicated. (i - iii) Closeups showing OSBP8-mCherry[+] ER-tubules close to the MCV. Yellow arrowheads point to ER-tubules in the vicinity of *M. marinum*. Mitochondria (Mit) were indicated in orange text, *M. marinum* (*M.m.*) and ER-tubules are pseudo-coloured in cyan and in yellow, respectively. N: nucleus. Scale bars, 5 µm (A); 2 µm (B) and 200 nm (i - iii). SD images were deconvolved. (C) SBF-SEM-derived images illustrate the correlation of the SD images and the volumetric segmentation of the EM data shown in Fig. 2F-G. The MCV is segmented in violet, *M. marinum* (*M.m.*) in cyan, ER-tubules in yellow and the nucleus in orange. Scale bars, 2 µm.
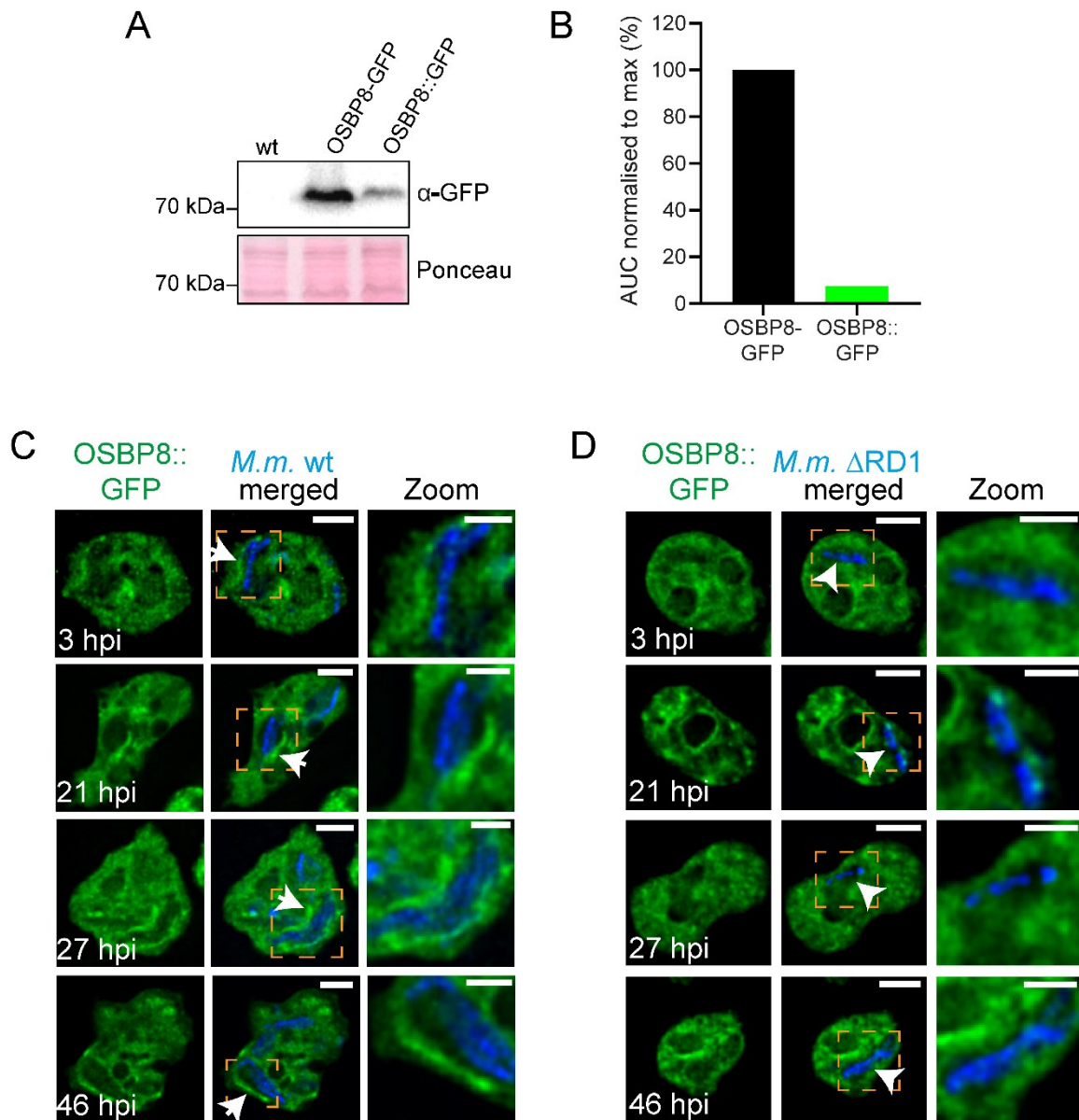
FIG S4 Subcellular localization of endogenous OSBP8::GFP during infection with *M. marinum* wt and ΔRD1. (A) Expression levels of OSBP8-GFP (overexpressed) compared to OSBP8::GFP (endogenous). (B) Quantification of A. Cells expressing OSBP8-GFP as well as OSBP8::GFP were harvested and then prepared for western blotting. The intensity of the bands was measured using ImageJ. AUC: area under the curve. (C-D) OSBP8::GFP mobilization during infection. Cells expressing OSBP8::GFP were infected with eBFP-expressing *M. marinum* wt or ΔRD1. At the indicated time points samples were taken for SD microscopy. Arrows point to OSBP8::GFP[+] intracellular mycobacteria and arrow heads indicate OSBP8::GFP[-] mycobacteria. Scale bars, 5 μm; Zoom, 2,5 μm. Images were deconvolved. *M.m.: M. marinum.*
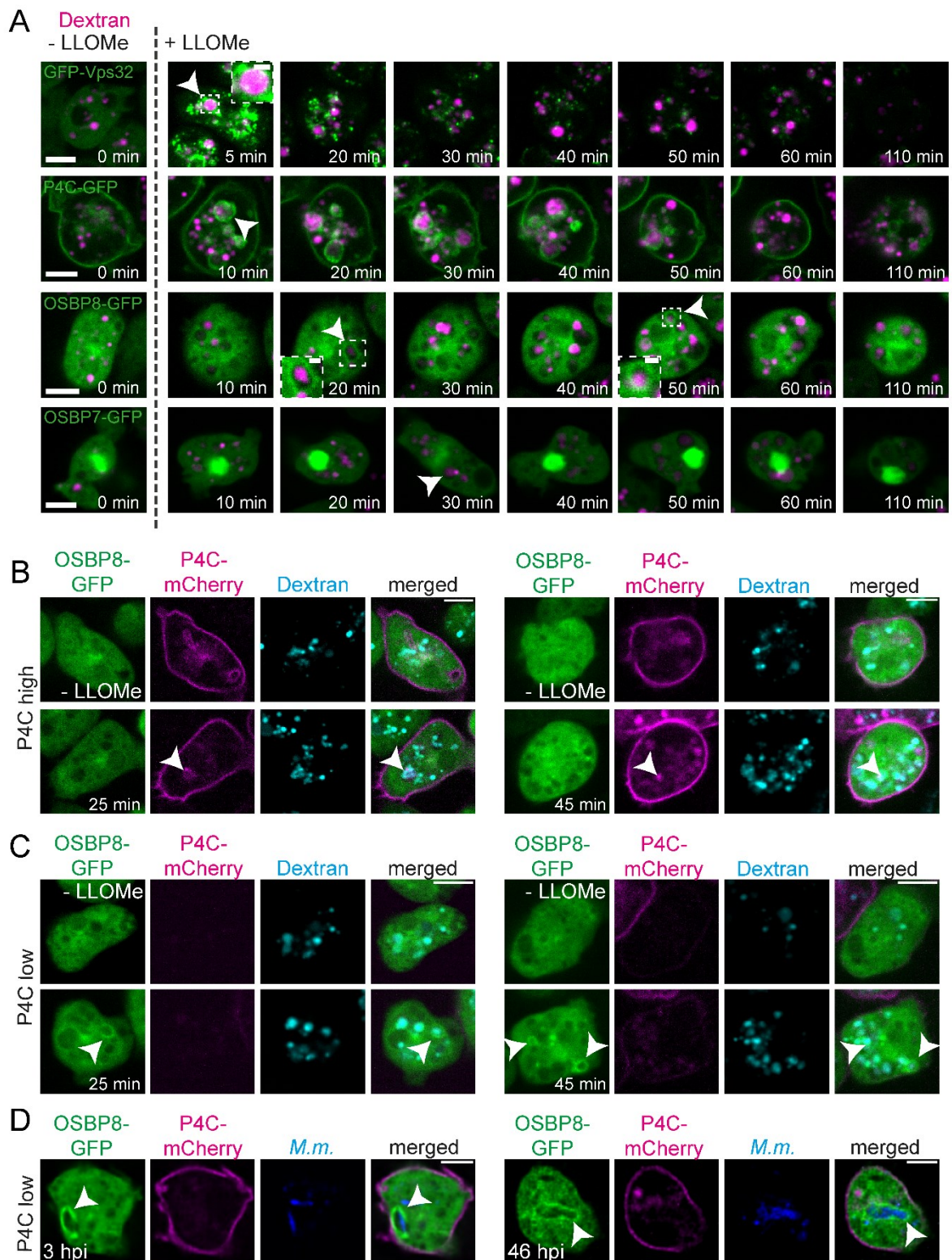
FIG S5 Localization of GFP-Vps32, P4C-GFP, OSBP8-GFP and OSBP7-GFP in non-infected cells. (A) Dynamics of GFP-Vps32, P4C-GFP, OSBP8-GFP and OSBP7-GFP on damaged lysosomes. (B-C) Recruitment of OSBP8-GFP to damaged lysosomes in cells highly expressing P4C-mCherry. Cells expressing GFP-Vps32, P4C-GFP, OSBP8-GFP, OSBP7-GFP or P4C-mCherry/OSBP8-GFP were incubated overnight with 10 kDa fluorescent dextran to label all endosomal compartments and then subjected to LLOMe. Arrow heads point to

FIG S5 legend continued

GFP-Vps32$^+$, P4C-GFP$^+$, P4C-mCherry$^+$, OSBP8-GFP$^+$ or OSBP7-GFP$^-$ lysosomes. Scale bars, 5 µm; Zoom, 1 µm. (D) OSBP8-GFP recruitment to MCVs in cells expressing P4C-mCherry at low levels. Cells overexpressing OSBP8-GFP/P4C-mCherry were infected with eBFP-expressing *M. marinum* wt. Images were taken at 3 and 46 hpi. Arrow heads point to OSBP8-GFP$^+$ *M. marinum*. Scale bars, 5 µm. *M.m.: M. marinum.*
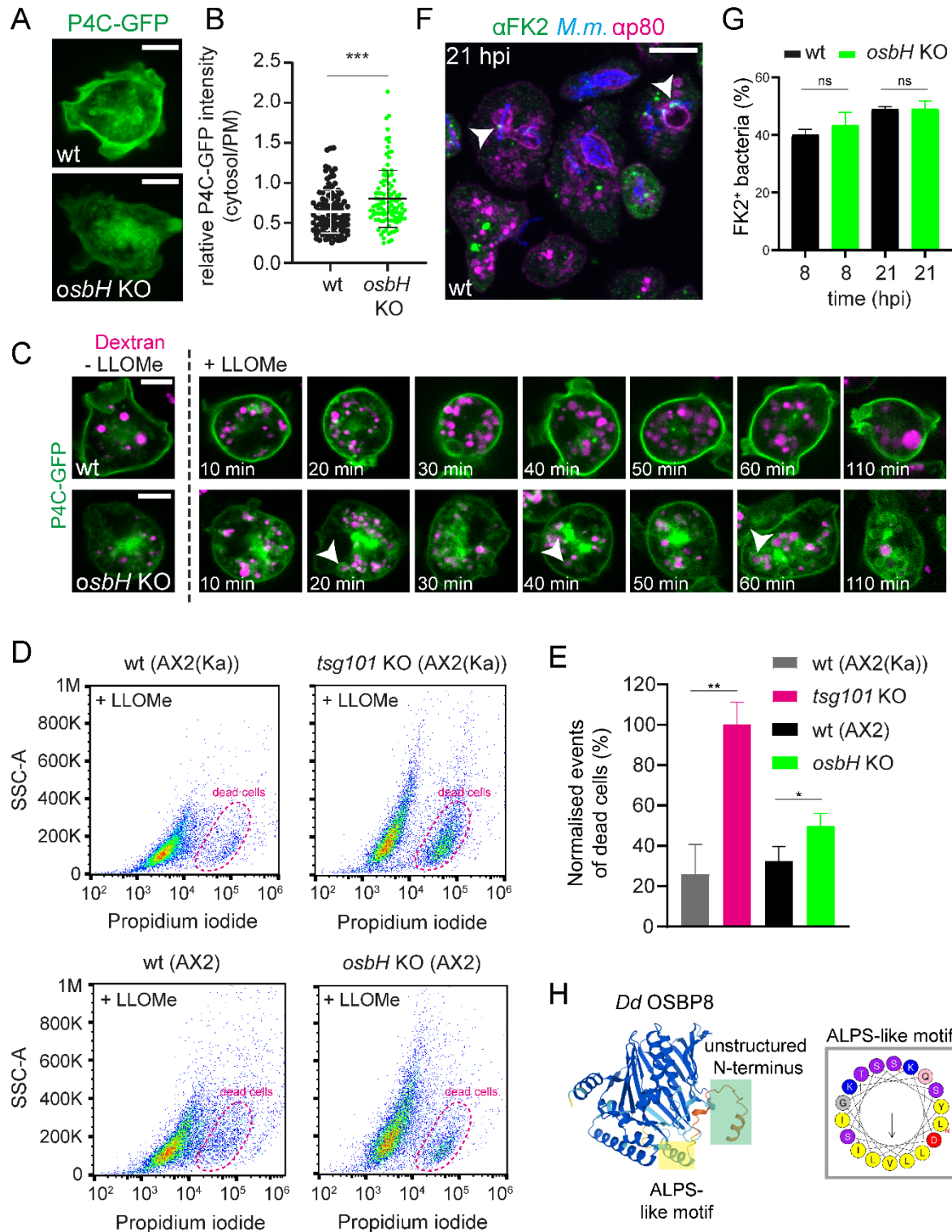
FIG S6 Effect of OSBP8 depletion on PI4P distribution and cell viability during lysosomal damage and on vacuolar escape of mycobacteria during infection. (A) PI4P distribution in non-infected wt and cells lacking OSBP8. (B) Quantification of A. Wt and *osbH* KO cells were imaged live. Shown are maximum z-projections of 15 z-stacks 300 nm apart. Scale bar, 5 μm. To label the PM for the quantification in B, cells were pre-stained with FM4-64. For each condition 108 cells per cell line were quantified using ImageJ. Plots show the mean and standard deviation of three independent experiments. Statistical significance was calculated with an unpaired t-test (***, p < 0.001). (C) P4C-GFP localization on damaged lysosomes in

FIG S6 legend continued

cells lacking OSBP8. Wt and *osbH* KO cells expressing P4C-GFP were incubated overnight with 10 kDa fluorescent dextran to label all endosomal compartments and then treated with LLOMe. Images were recorded every 5 min by SD microscopy. GFP-signal of the *osbH* KO cells was enhanced for better visualization. Scale bars, 5 µm. (D) Cell viability in wt and cells lacking OSBP8 upon LLOMe treatment. Wt, *osbH* or *tsg101* KOs were labelled with propidium iodide (PI) and incubated with LLOMe for 60 min. 10,000 cells were analysed per condition. Graphs are representative for two independent experiments. (E) Quantification of D. Plots were gated as indicated in (D), to reveal the number of dead cells. Plots in (E) show the mean and standard deviation of three independent experiments. Statistical differences were calculated with an unpaired t-test (*, $p < 0.05$; **, $p < 0.01$). (F) Vacuolar escape of mycobacteria in wt and cells lacking OSBP8. (G) Percentage of ubiquitin[+] bacteria in wt and *osbH* KOs at 8 and 21 hpi. Wt and *osbH* KO cells were infected with mCherry-expressing *M. marinum*, fixed and stained against ubiquitin (FK2) (green) and p80 (magenta). Representative maximum projections of 5 z-stacks of 500 nm at 21 hpi is shown in E. White arrowheads label ubiquitinated bacteria. Scale bars, 10 µm; Plots in (G) show the mean and standard deviation of three independent experiments (FK2 8, 21 hpi N=3, 138≤n≤462). Statistical differences were calculated with an unpaired t-test. ns: not significant. *M.m.: M. marinum.* (H) OSBP8 contains an unstructured N-terminus as well as an ALPS-like motif. The OSBP8 structure was derived from AlphaFold (https://alphafold.ebi.ac.uk/entry/Q54QP6) and analysed using HeliQuest (https://heliquest.ipmc. cnrs.fr/).

SUPPLEMENTAL MOVIES

Movie S1 Monitoring OSBP8-GFP recruitment by LLSM. For more information see Fig. 2A-B. [download]

Movie S2 3D rendering of LLSM data. For more information see Fig. 2C. [download]

Movie S3 Correlation and 3D reconstruction of SBF-SEM data. For more information see Fig. 2E-G, Fig. S3C. [download]

3.2.2. Author contributions

Here, I outline the contributions made by each author to this section of the thesis.

Together with Caroline Barisch, I designed the experiments. I generated most of the cell lines, carried out the majority of the OSBP8 infection experiments and imaging, analysed the data and created the final figures. Anna-Carina Mazur carried out the LLOMe assays, generated the OSBP8 knockin strain and used them in infections, analysed the transcriptomics and proteomics data and prepared related figures. Patricia Rosell-Arevalo performed *M. tuberculosis* infections and quantifications. Rico Franzkoch and Leonhard Breitsprecher assisted with 3D-HPF/FS-CLEM and SBF-SEM, respectively. In addition, they prepared related figures. Stevanus A. Listian conducted PI4P localization studies as well as intracellular mycobacterial growth assays in *osbH* KOs. Sylvana V. Hüttel performed the expansion microscopy. Danica Müller executed the cell viability experiments. Deise G. Schäfer generated the OSBP8-GFP cell line. Simone Vormittag and Hubert Hilbi generously provided P4C- and calnexin-harbouring plasmids, helped with suggestions and proofreading the manuscript. Markus Maniak provided the *osbH* KO cell line. In addition to reviewing the manuscript, Maximiliano G. Gutierrez supported and supervised the experiments with *M. tuberculosis*. Caroline Barisch supervised the project, identified the ALPS-like motif of OSBP8 and wrote the final draft of the manuscript.

3.3.1. Extended data

Deciphering the mechanism of OSBP8 mobilisation during mycobacterial infection

OSBP8 decorates cytosolic mycobacteria

Cumulative damage on the MCV membrane leads to the cytosolic translocation of mycobacteria. This occurs during later stages of infection. Strikingly, when cells expressing OSBP8-GFP were infected with mCherry-expressing *M. marinum*, we found OSBP8-GFP in the close vicinity of bacteria that appeared to be escaping from their vacuole or even cytosolic mycobacteria (Fig. 3.1A). Next, to confirm that OSBP8-GFP is indeed recruited to cytosolic mycobacteria, we performed LLSM with cells additionally expressing the MCV marker, AmtA-mCherry (Fig. 3.1B-C, Movie S3.1). This revealed that OSBP8-GFP localizes close to
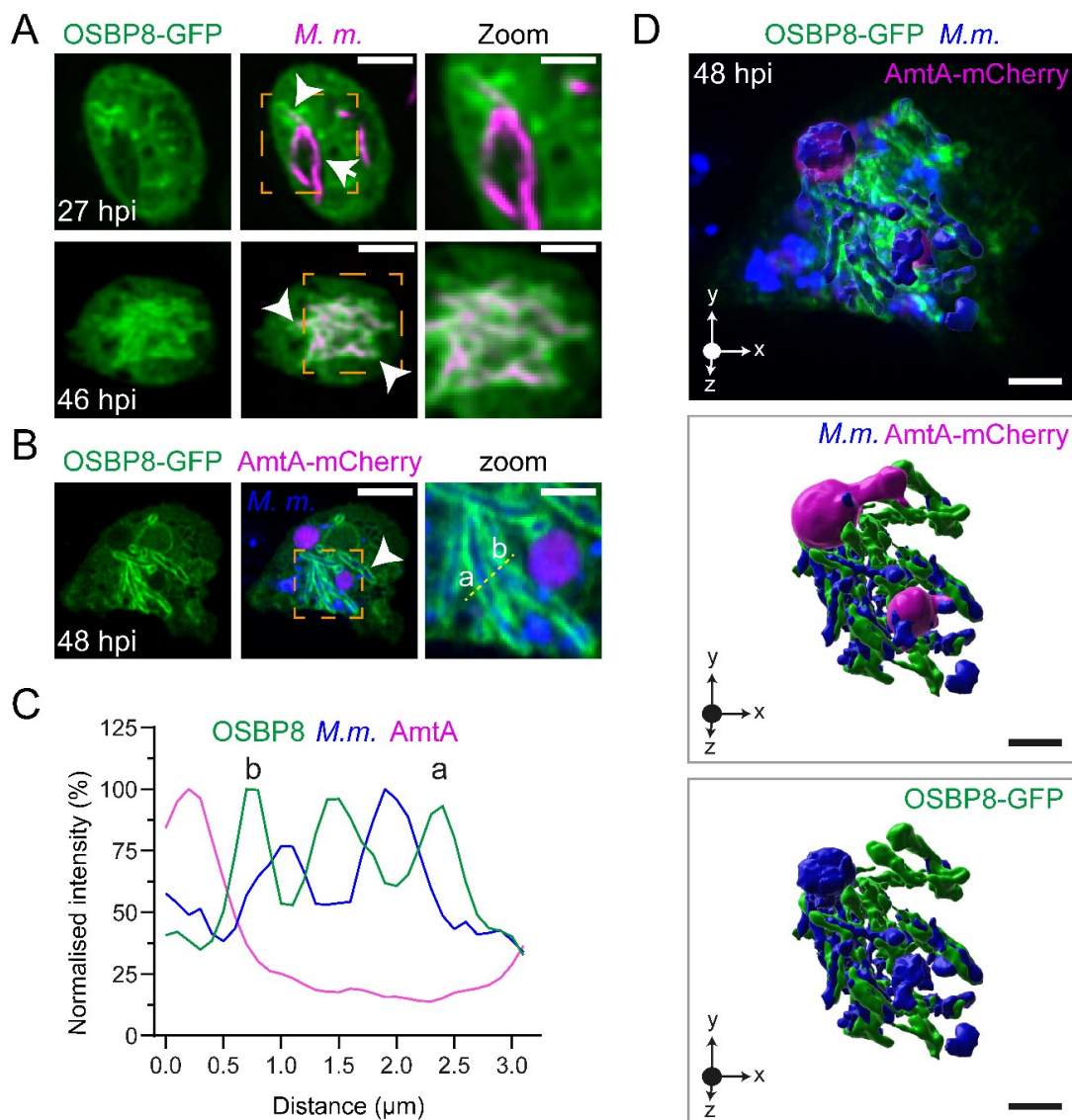

FIG 3.1 Interaction of OSBP8 with cytosolic mycobacteria. (A) Localization of OSBP8 to

FIG 3.1 legend continued

intracellular *M. marinum*. (B) LLSM to visualize OSBP8 in the immediate vicinity of cytosolic mycobacteria. (C) Intensity profile of the line plotted in the zoom of B. (D) 3D-model of the cell shown in (B) illustrating OSBP8-GFP$^+$ membranes wrapping around AmtA-mCherry$^-$ mycobacteria. Cells expressing OSBP8-GFP or co-expressing AmtA-mCherry were infected with mCherry- or eBFP-expressing *M. marinum* and imaged live at the indicated time points by SD microscopy or LLSM. Arrow points to OSBP8-GFP$^-$ MCV and arrow heads indicate OSBP8-GFP$^+$ cytosolic mycobacteria. See Movies S3.1 and S3.2 for more information. Scale bars in A and B, 5 µm; Zoom, 2.5 µm; in D, 2 µm.

AmtA-mCherry$^-$ mycobacteria. Interestingly, 3D-rendering of the infected cell revealed that OSBP8-GFP$^+$-structures fully enclose cytosolic bacteria (Fig. 3.1D, Movie S3.2). This suggests that mycobacteria might also induce the formation of contact sites between their surface and ER-tubules where OSBP8-GFP is localized.

To visualize the morphology of the potential ER-cytosolic mycobacteria contacts, cells expressing OSBP8-GFP were infected with mCherry-expressing *M. marinum* and subjected to conventional CLEM (in collaboration with Rico Franzkoch, EM facility, iBios, Fig. 3.2). Live cell imaging confirmed the recruitment of OSBP8-GFP to the intracellular bacteria (Fig. 3.2A). Strikingly, ultrastructural analyis revealed that these bacteria are cytosolic and are not surrounded by a membrane. Additionally, OSBP8-GFP$^+$ ER-tubules appeared close when LM and EM images were correlated (Fig. 3.2B-C). Altogether, these findings provide the first evidence that the ER and host LTPs might interact with cytosolic mycobacteria.
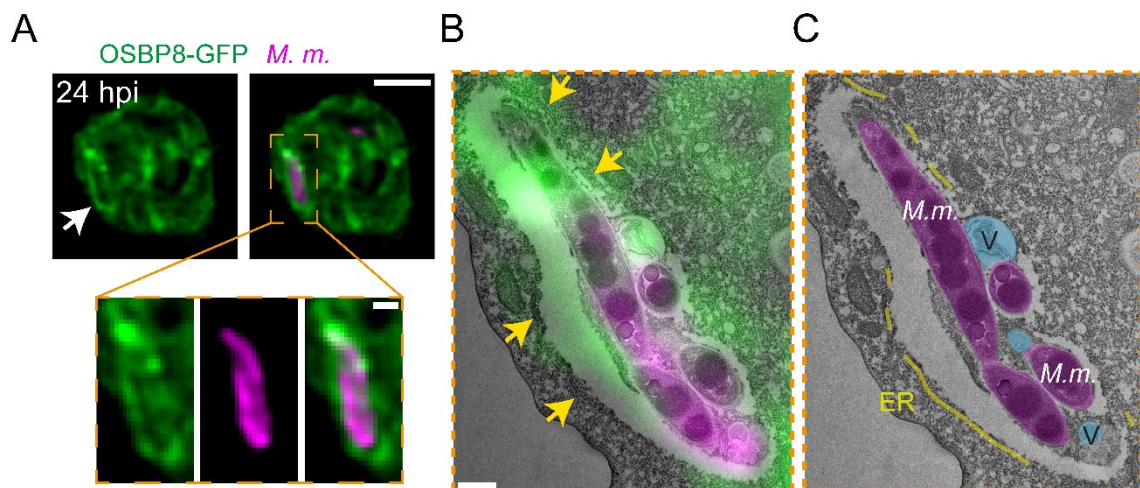

FIG 3.2 CLEM to visualize OSBP8-GFP$^+$-ER-tubules close to cytosolic mycobacteria. (A) SD microscopy to confirm OSBP8-GFP mobilisation. (B-C) EM micrograph showing the cell with correlated GFP and mCherry signals (B) or segmented structures (C). Cells expressing OSBP8-GFP were infected with mCherry-expressing *M. marinum*. At the indicated time point, cells were imaged live by SD microscopy and prepared for EM. Arrows point to OSBP8-GFP$^+$-ER-tubules. In C, ER-tubules were pseudo-coloured in yellow, *M. marinum* (*M.m.*) in purple and vacuoles in cyan. Image in A was deconvolved. Scale bars in A, 5 µm; Zoom in A, 2 µm, in B, 200 nm.

OSBP8 mobilisation appears to be independent on mycobacterial PDIM or phosphatases

Recently, the mycobacterial cell wall lipid PDIM of *M. tuberculosis* and *M. marinum* was shown to enhance the membranolytic activity of EsxA (Augenstreich et al., 2017, Lerner et al., 2018, Osman et al., 2020). To this end, it incorporates into host membranes where it influences membrane stability. In addition, PDIM was proposed to be essential for the recruitment of EsxA (Augenstreich et al., 2017). Altogether, this suggests that PDIM is present on the MCV and also on the cell wall of mycobacteria and might therefore play a role in the recruitment of OSBP8. PDIM and phenolic glycolipids are synthesized amongst others by a type II thioesterase, encoded by *tesA*. A transposon *M. marinum tesA* mutant is devoid of PDIM and attenuated in *D. discoideum* (Alibaud et al., 2011). To test whether the mobilization of OSBP8 is dependent on PDIM, we infected cells overexpressing OSBP8-mCherry with GFP-expressing *M. marinum ΔtesA* (Fig. 3.3A-B). Interestingly, OSBP8-mCherry was still recruited to intracellular mycobacteria.
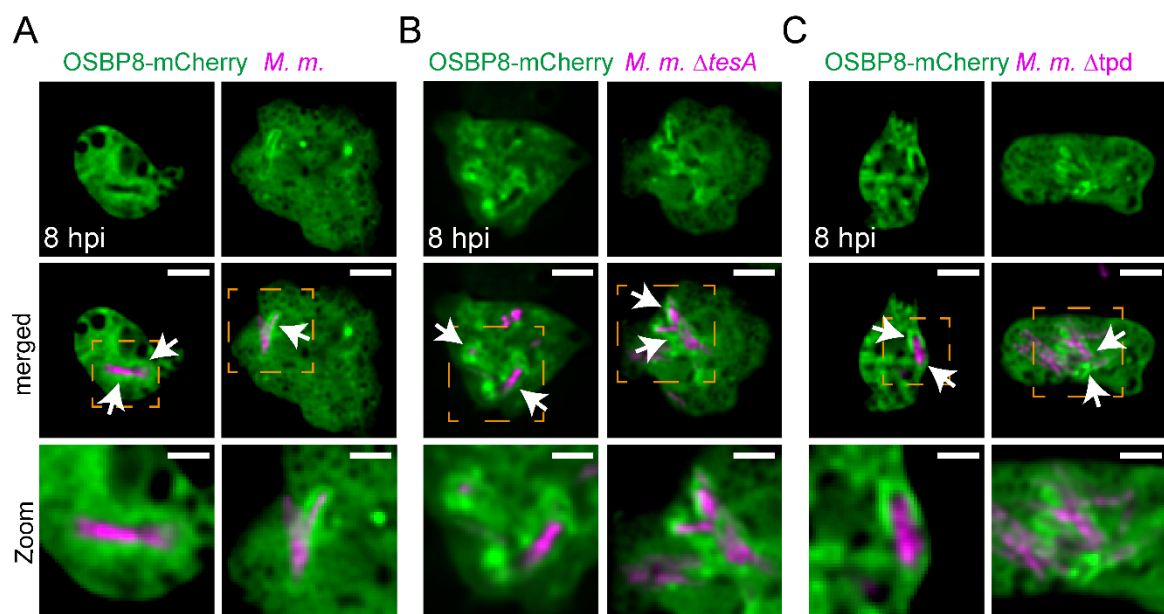

FIG 3.3 OSBP8-mCherry localization during infection with mycobacterial PDIM and phosphatases mutants. (A-C) Recruitment of OSBP8-mCherry to the intracellular mycobacteria. Cells overexpressing OSBP8-mCherry were infected with GFP-expressing *M. marinum* wt, Δ*tesA* or Δtpd. At the indicated time point samples were taken for SD microscopy. Shown are representative images of a single biological replicate. Arrows point to OSBP8-mCherry[+] intracellular mycobacteria. Scale bars, 5 µm; Zoom, 2.5 µm. Images were deconvolved. *M.m.: M. marinum.*

Mycobacterial phosphatases, PtpA, PtpB and SapM, remodel the PIP identity of the MCV in mammalian cells (Wong et al., 2011, Beresford et al., 2007, Vergne et al., 2005). In *D. discoideum*, *M. marinum* triple phosphatase deletion (Δtpd) mutant is severely attenuated.

In addition, an accumulation of PI3P was observed on the MCVs of this mutant (Koliwer-Brandl et al., 2019). Since in many cases OSBPs are recruited by interaction with PIPs (Weber-Boyvat et al., 2015, Sohn et al., 2018), we wanted to investigate whether the secreted mycobacterial phosphatases are involved in OSBP8-mCherry recruitment to the MCV. To this end, cells were infected with the GFP- expressing *M. marinum* Δtpd mutant (Fig. 3.3A, C). Analogous to PDIM-deficient mycobacteria, OSBP8-mCherry recruitment was observed. Since an early infection time point (8 hpi) was chosen, we hypothesize that the mobilisation of OSBP8-mCherry is independent of the secreted phosphatases.

OSBP8 recruitment might be mediated by the ALPS-like motif

Various imaging approaches revealed that OSBP8 is recruited to ER-MCV MCS during infection. However, OSBP8 is localized at ER-Golgi MCS in uninfected cells, similar to its *S. cerevisiae* homologue Osh4. Osh4 has an amphipathic lipid packing sensor (ALPS)-motif at its N-terminus that interacts with membranes (Drin et al., 2007). Interestingly, sequence analysis revealed that OSBP8 has an ALPS-like motif. Based on these similarities, we hypothesized that the ALPS-like motif of OSBP8 might mediate membrane targeting. Consequently, we transformed cells with various truncated versions (C-terminally GFP-tagged) of OSBP8 (Fig. 3.4). Strikingly, the fusion construct containing the ALPS-like motif and the unstructured N-terminus (1 - 57 amino acids) still localized at ER-Golgi MCS, similar to the full length (FL) protein. However, the construct lacking the N-terminus (58 - 401 amino acids) was distributed in the cytosolic and in the nucleus. Altogether, these data suggests that the ALPS-like motif of OSBP8 might be critical for the mobilisation to membranes. If the ALPS-like motif also confers to the recruitment to the MCV or cytosolic bacteria awaits experimental validations.
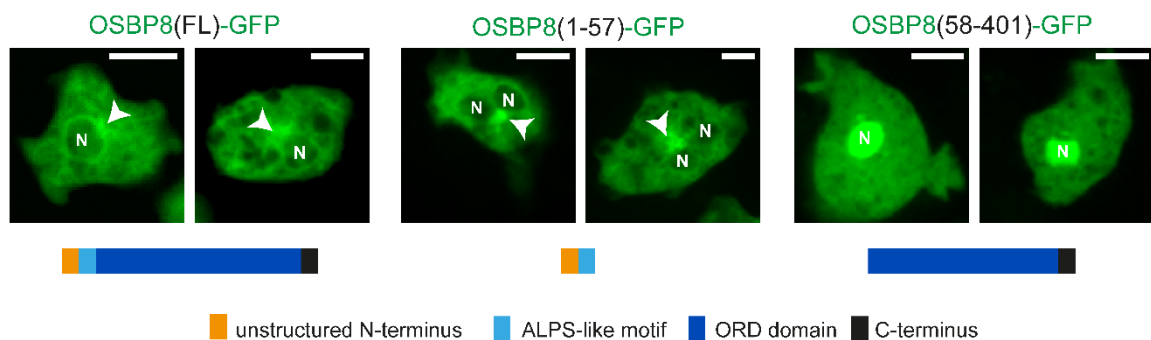

FIG 3.4 Identification of the OSBP8 sequence motifs essential for membrane targeting. Cells were transformed with the indicated C-terminal GFP-tagged truncated versions of OSBP8 and imaged live by SD microscopy. Arrows indicate ER-Golgi MCS. N; nucleus, FL; full length. Scale bars; 5 μm.

Lack of OSBP8 might be compensated by other OSBPs

OSBP8-depletion did not result in a drastic reduction of sterols inside MCVs indicating that other OSBPs might be involved in sterol transport. Sequence analysis showed that OSBP9 and OSBP11 are very close to OSBP8 (Vormittag et al., 2023). In addition, analysis of transcriptomic data (Hanna et al., 2019) revealed that OSBP9 and OSBP11 are upregulated during infection. To study their subcellular localization, we generated cells overexpressing OSBP9-GFP and OSBP11-GFP (C-terminally GFP-tagged) (Fig. 3.5). Interestingly, OSBP9-GFP is cytosolic and is localized on bead-containing phagosomes (BCPs) (Fig. 3.5A-B) that are positive for the lysosomal and post-lysosomal markers VatA and VacA, respectively. In contrast, OSBP11-GFP is localized in the cytosol and at the PM and not on BCPs (Fig. 3.5C-D).
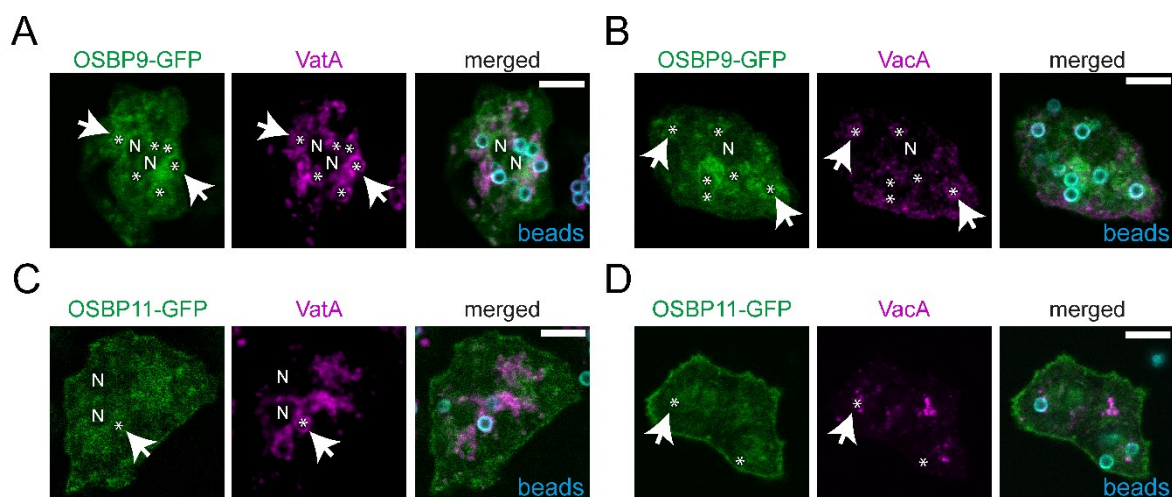

FIG 3.5 Localization of OSBP9-GFP (A-B) and OSBP11-GFP (C-D) in uninfected cells. Cells overexpressing both proteins were incubated with fluorobeads for 2 hrs, fixed and then stained with αVatA (vATPase subunit A, lysosomes) and αVacA (VacuolinA, post-lysosomes) antibodies. Arrows point to OSBP9^{+} or OSBP11^{-} BCPs. Asterisks indicate fluorobeads, N: nucleus, BCP: bead-containing phagosome. Scale bars, 5 μm.

These observations indicate that although these OSBPs are close to OSBP8, they differ in subcellular localization and might have non-redundant functions. Whether they are manipulated by mycobacteria during infection remains to be investigated.

Materials and Methods

D. discoideum plasmids, strains and cell culture
All the *D. discoideum* material is listed in Table S2.

Mycobacteria strains, culture and plasmids
All the *M. marinum* material is listed in Table S2.

Infection assays, live cell imaging, immunofluorescence and CLEM

The infection experiments, live cell imaging, immunostaining and CLEM (conventional TEM) were performed as previously described in the second manuscript of this thesis.

Table S2 Material used in this study

D. discoideum strains	Relevant characteristics	Source/Reference
Ax2	wt, parental strain	
D. discoideum plasmids		
OSBP8-GFP	pDM323-*osbH*, G418^r, Amp^r	This study
AmtA-mCherry	pDM1044-*amtA*, Hyg^r, Amp^r	(Barisch et al., 2015)
OSBP8-mCherry	pDM1210-*osbH*, Hyg^r, Amp^r	This study
OSBP11-GFP	pDM323-*osbK*, G418^r, Amp^r	This study
OSBP9-GFP	pDM1045-*osbI*, Hyg^r, Amp^r	Letourneur Lab, France
OSBP8 (N long)-GFP	pDM323-*osbH*(1-57), G418^r, Amp^r	This study
OSBP8 (C term)-GFP	pDM323-*osbH*(58-401), G418^r, Amp^r	This study
M. marinum strains	Relevant characteristics	Source/Reference
M. marinum M	wt, parental strain	L. Ramakrishnan (University of Cambridge)
M. marinum ∆*tesA*	*Tn5370* transposon inserted	(Alibaud et al., 2011)
M. marinum ∆tpd	triple phosphatase mutant	(Koliwer-Brandl et al., 2019)
M. marinum plasmids		
pTEC18	eBFP2 under control of the MSP promoter, Hyg^r, Amp^r	Addgene #30177, (Takaki et al., 2013)
pCherry10	mCherry under control of the G13 promoter, Hyg^r, Amp^r	Addgene #24664, (Carroll et al., 2010)
pmsp12::GFP	GFP production under control of *M. marinum* msp12 promoter, Kan^r	(Cosma et al., 2004)

SUPPLEMENTAL MOVIES

Movie S3.1: Monitoring OSBP8-GFP recruitment to cytosolic mycobacteria by LLSM. For more information see Fig. 3.1B. [download]

Movie S3.2: 3D rendering of LLSM dataset. For more information see Fig. 3.1D. [download]

3.3.2. Author contributions

Here, I summarise the contributions made by each author to this section of the thesis.

I generated few cell lines, carried out the infection experiments, performed live and fixed imaging and prepared the final figures. Rico Franzkoch performed the transmission electron microscopy and prepared related figures. Deise G. Schäfer generated the OSBP8-GFP cell line. François Letourneur generously provided OSBP9-containing plasmid. Caroline Barisch generated the truncated versions of OSBP8 and prepared related figures.

4. DISCUSSION

To escape killing by professional phagocytes, *M. tuberculosis* has developed a number of strategies. While it causes MCV damage to abrogate the innate immune functions of the vacuole and to translocate to the cytosol, the host fights this process by recruiting machineries for repairing membranes. To envision these processes, new methodologies were required. In this thesis, I, together with the EM facility, established 3D-HPF/FS-CLEM to monitor MCV exit events and organelle interactions in *D. discoideum*. The second aim of my thesis was to test if mycobacterial infection induces an ER-dependent repair pathway as well as to identify the OSBPs involved. We found that the genes encoding Sac1 and PI4Ks, two proteins that are part of ER-dependent repair, were upregulated at late infection stages. Although OSBPs were differentially regulated during infection, proteomics data revealed four OSBPs that might be involved in the process. Remarkably, I found that the ER-Golgi protein OSBP8 is mobilised to the MCV in *D. discoideum* and this mobilisation was dependent on the MCV damage very likely caused by EsxA. Advanced imaging approaches revealed that OSBP8 is localized on the ER-tubules in the vicinity of damaged MCVs.

The next objective was to investigate the function of the ER-dependent repair pathway during infection. Based on the subcellular localization in uninfected cells, I speculated that OSBP8 might be a functional homologue of *H. sapiens* OSBP and *S. cerevisiae* Osh4. Both exchange PI4P for sterols at contact sites. Strikingly, we discovered that the loss of OSBP8 resulted in PI4P retention on MCV/lysosomes and a minor reduction in sterol accumulation in the MCV. Furthermore, I found that the MCV/lysosomes in cells lacking OSBP8 exhibited altered proteolytic and lysosomal function, indicating a repair defect. In line with this, I observed accelerated growth of *M. marinum* in these cells and conversely, a growth reduction in OSBP8-GFP overexpressing cells. Altogether, these findings revealed a new MCV repair pathway, ER-dependent MCV repair, in which OSBP8 balances PI4P levels on the MCV membrane. Additionally, I found that OSBP8 interacts with cytosolic mycobacteria. I hypothesize that this interaction might be important for the delivery of lipids that serve mycobacteria as an important nutrient source during infection. Alternatively, this might be another defense strategy of the host.

Another objective was to test if ER-dependent repair is conserved in the macrophage/ *M. tuberculosis* system. To this end, we collaborated with the Gutierrez lab at the Francis Crick Institute, London, UK. Strikingly, mycobacteria infection of *D. discoideum* and macrophage shared a similar transcriptomic signature. In addition, also in human macrophages the mobilisation of OSBP to intracellular mycobacteria is dependent on the presence of ESX-1.

4.1. 3D-CLEM as a bimodality imaging system to explore vacuole rupture and OSBP8-mediated ER-dependent repair

The cytosolic translocation of *M. tuberculosis* in macrophages (Aylan et al., 2023a, Bernard et al., 2020) or *M. marinum* in *D. discoideum* (Hagedorn and Soldati, 2007) requires ESX-1-dependent vacuole destruction. This host-pathogen battlefield does, in fact, involve complex membrane dynamics and re-organisation, as well as the recruitment of repair pathways. A correlative methodology to investigate phagosomal escape or organelle contacts during *M. marinum* infection in *D. discoideum* was lacking. Consequently, we developed a simple and reproducible 3D-HPF/FS-CLEM method by taking advantage of two imaging modalities. We combined high resolution LM and TEM-tomography and integrated HPF/FS to retain the lipid bilayers in their near-native state (Franzkoch et al., 2023). Improving cell adhesion, including a mild fixation, a customized imaging setup and HPF/FS were essential to acquire 3D-fluorescent images with high resolution for precise correlation. These critical steps ruled out the limitations on z-resolution and intermediate fixation, addressed previously for HPF-CLEM in mammalian cells (Spiegelhalter et al., 2010) and conventional CLEM in *D. discoideum* (Gerstenmaier et al., 2015, Malinovska et al., 2015). Remarkably, using 3D-HPF/FS-CLEM, we resolved MCV exit of *M. marinum* and inter-organelle contacts. The intermediate fixation step reduced the sample transfer delay between modalities and preserved the ultrastructural detail of membranes. However, an alternative for HPF/FS would be cryo-CLEM system with portable cryofixation chambers (Jun et al., 2019). There are also other variants such as an automated cryo-CLEM system that permits automatic correlation of fiducials (Fu et al., 2019) or an integrated microscope that has a LM unit in TEM operating at cryogenic temperatures (Faas et al., 2013). However, the choice of LM units for integrated microscopes is restricted.

TEM-tomography provided ~ 1 nm axial resolution of the sample for volumes less than 250 nm thin sections and allowed 3D reconstructions. For live events with larger 3D volume context, organelle or cell morphology, our fixation step could be paired with FIB-SEM (Struckman et al., 2023, López-Jiménez et al., 2018, Beckwith et al., 2015, Acevedo-Sánchez et al., 2023) or SBF-SEM (Russell et al., 2017, Lerner et al., 2016). In agreement with this, when we adapted the fixation protocol for SBF-SEM, the generated dataset enabled 3D reconstruction and manual ER segmentation to visualise ER-MCV MCS containing OSBP8 in *D. discoideum* (Anand et al., 2023). Overexpressing actin binding domain (ABD) significantly enhanced adherence and allowed to readily overlay LM data on the EM dataset using plasma membrane as a reference. Despite its many advantages, this approach, like other correlative workflows, is time-consuming but has appreciable throughput. However, 3D-HPF/FS-CLEM opens up fresh perspectives on how to comprehend organelle contacts, survival and egress of pathogens in multiple model systems.

4.2. Recruitment of OSBP8 to the contact sites mediates MCV repair

The mycobacterial RD1 locus encodes the T7SS ESX-1 and the secreted peptide EsxA that was hypothesized to inflict vacuole damage (Osman et al., 2022). Strikingly, I found that OSBP8 is immobilised in the absence of ESX-1 (*M. marinum* ΔRD1) and EsxA (*M. marinum* ΔCE) confirming that MCV rupture is essential for OSBP8 recruitment. I further tested if the PIP identity of the MCV conferred by three secreted mycobacterial phosphatases has an impact on OSBP8 mobilisation (Fig. 3.1). Notably, I found that OSBP8 is recruited to the intracellular *M. marinum* Δtpd (phosphatases). Moreover, I tested if OSBP8 has an affinity for PDIM due to its ability to incorporate into host membranes. Interestingly, I found that OSBP8 is recruited to the intracellular *M. marinum* Δ*tesA* (PDIM). However, further experiments with MCV markers are required to verify whether OSBP8 is recruited to vacuoles containing PDIM or phosphatase mutant mycobacteria.

How are OSBP and OSBP8 recruited to ER-MCV MCS? An important finding of this thesis is the ESX-1-dependent recruitment of endogenous OSBP to intracellular *M. tuberculosis* in human macrophages. Presumably, OSBP is recruited to ruptured MCVs in analogy to studies showing that upon sterile damage, OSBP re-localizes from trans-Golgi- to lysosome-ER contacts (Tan and Finkel, 2022, Radulovic et al., 2022). The recruitment of OSBP damaged lysosomes is initiated by the accumulation of PI4P, which leads to contact site induction (Tan and Finkel, 2022, Radulovic et al., 2022). At ER-lysosome contacts, OSBP tethers to VAP through the FFAT motif contributing to the stability of the contacts and fostering lipid exchange (Tan and Finkel, 2022, Radulovic et al., 2022). Consequently, OSBP mobilisation during *M. tuberculosis* infection of human macrophages might also be dependent on PI4P enrichment on the MCV and the same tethers might indeed maintain the ER-MCV MCS (Fig. 4.1A). Besides OSBPs, STARD3 also binds to VAP via phospho-FFAT at ER-lysosome contacts (Di Mattia et al., 2020). STARD3-VAP interaction also mediates the transfer of cholesterol to the endolysosomes from the ER (Wilhelm et al., 2017). This suggests that STARD3 might also play a role during mycobacterial infection in analogy to OSBP (Fig. 4.1A). Another striking finding documented in this thesis is that various advanced imaging approaches such as LLSM, ExM and 3D-CLEM revealed that OSBP8 localizes on the ER-tubules in the proximity of the ruptured MCV. In addition, damaged MCV accumulates PI4P. Unlike OSBP, *D. discoideum* OSBPs lack an FFAT motif to interact with VAP. Preliminary experiments with infected *vap* KO cells show that OSBP8 recruitment to the MCV is abolished when VAP is lacking, however OSBP8 is still recruited to cytosolic mycobacteria (Anna Mazur, unpublished data). This implies that VAP is crucial for the establishment of ER-MCV contacts, whereas it is not required for the induction of ER-cytosolic bacteria contacts. Since OSBP8 does not have an FFAT motif
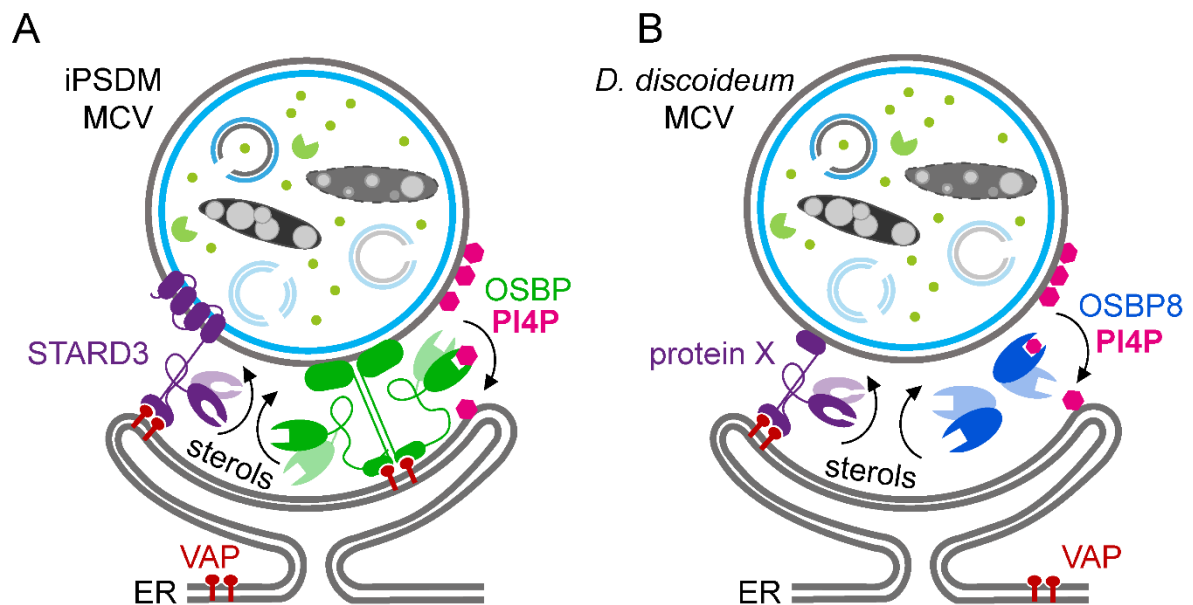
FIG 4.1 Hypothetical model for ER-MCV tethering in macrophages and *D. discoideum* to restore lysosomal function. (A) OSBP and STARD3 binds to VAP in mammalian cells with *M. tuberculosis*. (B) In *D. discoideum* with *M. marinum,* an unknown tether protein X may maintain the contact site where OSBP8 shuttles the lipids. Recovery of MCV integrity may lead to mycobacterial restriction.

to interact with VAP it is tempting to speculate that other LTPs might participate in stabilizing the ER-MCV contact site. Interestingly, the genome of *D. discoideum* encodes two proteins with a STAR-lipid transfer domain (DDB_G0285445, DDB_G0280895). Both proteins are upregulated during mycobacterial infection (Hanna et al., 2019). However, whether they contain an FFAT motif or transmembrane domains remains to be analysed. Consequently, I propose that an unknown tether protein X which binds to VAP might be important to maintain stability of ER-MCV MCS in *D. discoideum* (Fig. 4.1B).

What are the consequences of OSBP8 and OSBP depletion for MCV function? I found that OSBP8 deficiency hampered lysosomal function of MCVs concerning acidification and proteolytic activity. This created a mycobacteria-friendly environment which enhanced their growth suggesting that the MCVs are leaky as the phagosomal escape was unaffected. In agreement with this, LLOMe treatment of OSBP8 depleted cells had an impact on cell viability upon sterile damage. These findings complement recent studies in mammalian cells that showed that cells lacking OSBP were less viable upon sterile damage (Radulovic et al., 2022). This is due to the discharge of intraluminal ions and proteases from ruptured lysosomes indicating a failure in membrane repair. Notably, we observed damage-dependent OSBP mobilisation during *M. tuberculosis* infection. However, additional experiments with MCV markers, for example LAMP2 (Lerner et al., 2020) combined with CLEM are necessary to confirm that OSBP is localized at ER-MCV MCS in human macrophages. To validate the

importance of ER-dependent repair during *M. tuberculosis* infection, monitoring bacterial growth in OSBP deficient cells and experiments with Lysotracker (Aylan et al., 2023b) or DQ-BSA (Bedard et al., 2023) to monitor MCV function are vital.

Interestingly, the similar trend of OSBP recruitment were observed in *Salmonella*-infected HeLa cells (Kolodziejek et al., 2019, Auweter et al., 2012). However, inhibition of OSBP led to an increase in cytosolic *Salmonella* (Kolodziejek et al., 2019). This suggests that OSBP-mediated ER-dependent vacuole repair might be involved also during *Salmonella* infection. Besides OSBP, ORP1L is also localized at ER-endolysosomal (Radulovic et al., 2022) and at ER-*Coxiella*-containing vacuole contacts (Justis et al., 2017, Schuler et al., 2023). Importantly, both OSBP and ORP1L are tethered to VAP on the ER. Collectively, during ER-dependent repair OSBPs, including OSBP and ORP1L, supply adequate lipids to restore the MCV membrane integrity.

4.3. OSBP8 might exchange PI4P for sterols during ER-dependent MCV repair

Production of PI4P on damaged lysosomes is essential for the establishment and extension of contacts with the ER (Tan and Finkel, 2022, Radulovic et al., 2022). PI4P on endolysosomes is synthesized by PI4K2A and PI4K2B (Jani et al., 2022, Balla et al., 2002). While knocking out PI4K2A led to a major impairment of ER-dependent lysosomal repair, knockout of PI4K2B showed only minor effects indicating both proteins might have a functional redundancy (Tan and Finkel, 2022). Strikingly, transcriptomics data analysis revealed that PI4K2B is upregulated in *M. tuberculosis* infected iPSDMs. This implies that PI4K2B rather than PI4K2A might generate PI4P on the *M. tuberculosis*-containing vacuole. Intriguingly in *D. discoideum*, two PI4-kinases, *pi4k* and *pikD,* and PI4-phosphatase, Sac1, were upregulated at late infection stages. Altogether, this suggests that these proteins might be involved in creating the PI4P gradient between the organelles.

Another striking finding of this thesis is that the depletion of OSBP8 led to a slight decrease in sterol accumulation in the MCV and a massive accumulation of PI4P on the MCV. In line with this, live cell imaging of LLOMe treated cells showed a retention of PI4P on lysosomes. However, in cells expressing P4C-mCherry, OSBP8-GFP recruitment was inhibited suggesting P4C might compete with OSBP8 for PI4P on the MCV. These findings suggest that during ER-dependent repair OSBP8 mediates balancing PI4P levels on the MCV membrane in exchange for sterols from the ER as demonstrated for OSBP on damaged lysosomes (Radulovic et al., 2022). Consequently, I speculate that OSBP restores PI4P levels on the MCV during ER-dependent MCV repair in macrophages.

How does OSBP8 mediate lipid transfer? The best- characterized short form so far is

S. cerevisiae Osh4. Based on biochemical assays and *in silico* methods, previous studies have reported that: (i) Osh4 extracts PI4P from membranes in exchange for ergosterol (Mesmin et al., 2017, de Saint-Jean et al., 2011), and (ii) sterol transfer is fuelled by a PI4P gradient established by Sac1 (Moser von Filseck et al., 2015). The polar head group of PI4P interacts electrostatically with the ORD of Osh4 (Antonny et al., 2018). The lid segment of Osh4 packs the ligands in its hydrophobic pocket mediating the shuttling of ergosterol and PI4P at the ER-Golgi MCS (de Saint-Jean et al., 2011). OSBP8 is also a short version with the ORD and is close to Osh4 phylogenetically. Therefore, I speculate that OSBP8 might transfer lipids similar to Osh4.

Additionally, Osh4 contains an ALPS motif that interacts with unsaturated and curved membranes (Drin et al., 2007) and certain regions of the ORD domain interact with membranes that are negatively charged (Schulz et al., 2009). Interestingly, according to the sequence analysis, OSBP8 has a lid and an ALPS-like motif at the N-terminus similar to Osh4. This suggests that the ALPS-like motif of OSBP8 may also mediate its membrane localization. In line with this, I observed that the truncated version of OSBP8 with the ALPS-like motif localizes at ER-Golgi MCS in analogy to its full length (Fig. 3.4). Consequently, I believe that OSBP8 might have a similar function like the Osh4 in maintaining PI4P/sterol exchange at the ER-Golgi MCS (Fig. 4.2A-B). Further validation of the lipid ligands of OSBP8 using donor-acceptor liposome assays (de Saint-Jean et al., 2011) and PIP strip assays (Charman et al., 2014) are essential. An alternative to this would be incubating OSBP8 with photoactivatable lipids (paclipids)-containing liposomes (Haberkant and Holthuis, 2014). Interestingly, preliminary experiments using paclipids indicated that OSBP8 has the highest binding affinity for pacChol, a sterol analogue (Fig. 4.2C-D) (Deise Schäfer, unpublished data). If OSBP8 interacts or transports sterols remains to be established. However, the altered distribution of PI4P in OSBP8 depleted cells is a good indication that OSBP8 function is linked to sterol counter transport.

4.4. OSBP8-mediated ER-dependent repair might interfere with other pathways

Four lysosomal membrane repair machineries including autophagy have been described (Barisch et al., 2023). Presumably, the temporal and spatial distribution of these repair mechanisms might be different. In line with this, we observed that upon sterile damage the recruitment of OSBP8 (20 - 40 min) occurs later than the recruitment of ESCRT-III components (0 - 5 min). This is in agreement with the fact that the enrichment of OSBP foci occurs ~ 20 min following lysosomal damage. However, PI4P accumulation and ESCRT-III recruitment exhibits similar temporal distribution (~ 5 min following damage; (Radulovic et al., 2022, Radulovic et al., 2018)). This suggests that ESCRT-dependent repair might precede ER-dependent repair.
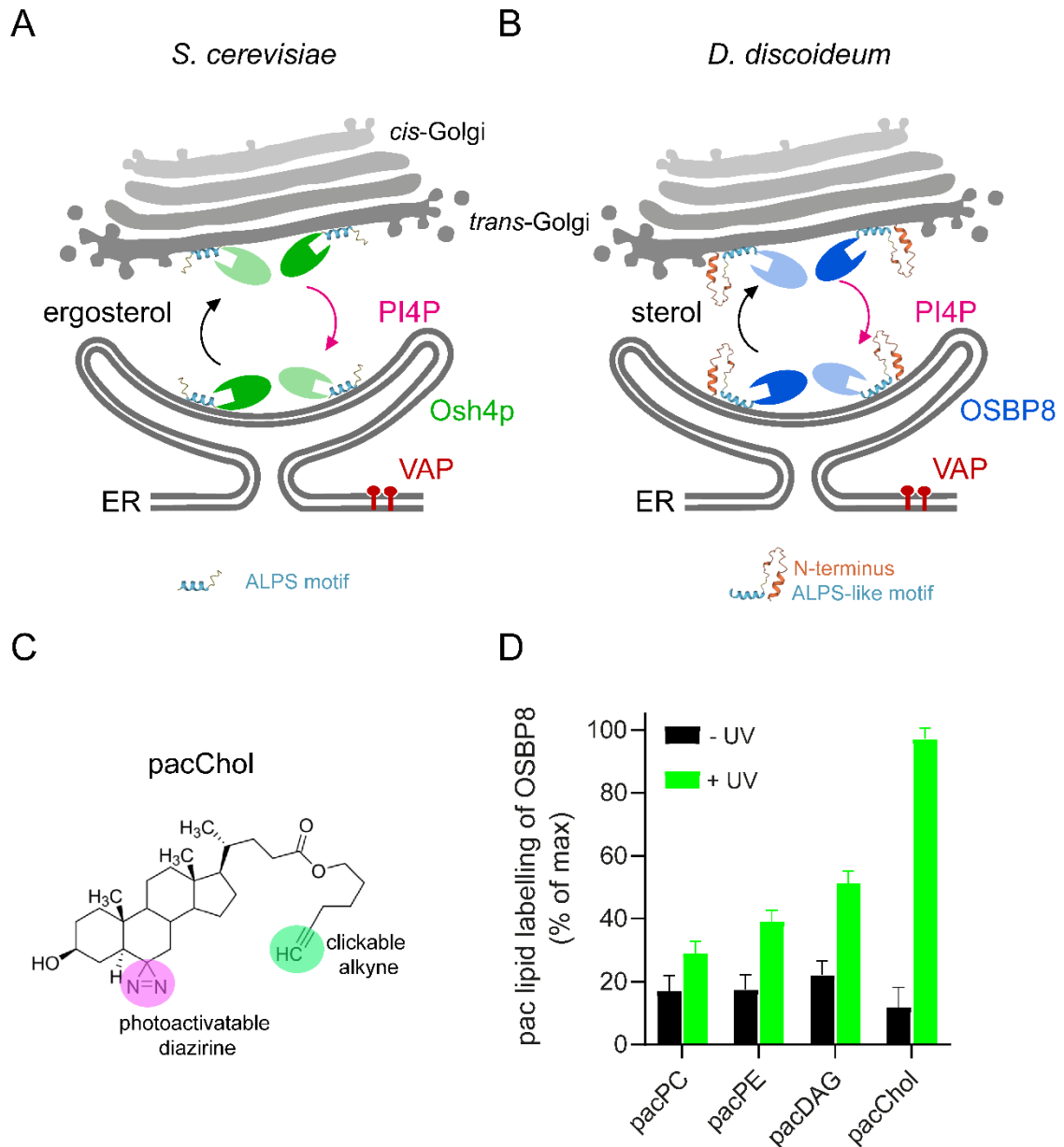
FIG 4.2 Proposed model for lipid transport of OSBP8 at ER-Golgi MCS and its potential ligands. (A) The ALPS motif of Osh4 binds to membranes enabling PI4P/ergosterol exchange. (B) The ALPS-like motif of OSBP8 might interact with membranes prior to PI4P/sterols shuttling at the ER-Golgi interface. (C) Structure of the photoactivatable analogue pacChol. (D) Identification of potential lipid ligands of OSBP8. Purified OSBP8 was incubated with pacPC, pacPE, pacDAC and pacChol containing liposomes. After a UV pulse, samples were click-reacted with AF647-N3, subjected to SDS-PAGE, and analysed by in-gel fluorescence (IGF) and Coomassie staining. Quantification was performed using ImageJ.

In infected *D. discoideum*, the temporal dynamics of OSBP8 enrichment at the MCV exhibit consistency with the recruitment patterns of ESCRT-III (Vps32 and Tsg101) (López-Jiménez et al., 2018) and autophagy components (Atg8a) (Cardenal-Muñoz et al., 2017). However, the ESCRT-III components are localized spatially earlier and at distinct sites of the damaged MCV in contrast to autophagy-related proteins (López-Jiménez et al., 2018). Nonetheless, to gain a comprehensive understanding of the spatial distribution and precise timing of recruitment for ER-dependent repair in comparison to ESCRT- and SM-dependent repair, further experimental investigations are necessary. Still, this strongly implies that cells employ different repair mechanisms, probably depending on the extent of membrane damage. While ESCRT- and SM-dependent pathway repair small lesions, larger lesions might be sealed by membrane patches delivered by autophagy (Cardenal-Muñoz et al., 2017, Niekamp et al., 2022). I hypothesize that the function of ER-dependent repair is to deliver lipids for ESCRT- and SM-dependent repair to remove the damaged area by ILV formation. First evidence comes from the fact that membrane spirals accumulate in the MCV of *D. discoideum* which are rich in sterols (Barisch et al., 2015). Strikingly, I found that the lack of OSBP8 did not drastically alter sterol accumulation inside the MCV. Consequently, it is plausible that sterols might additionally be transferred to the MCV by vesicular trafficking or by other LTPs such as OSBP6, 9, 11 or 12. In case of *M. tuberculosis* infection, ORP5 and ORP9 were upregulated. This is supported by the fact that in mammalian cells, apart from OSBP, ORP9 and ORP11 also assist in the repair of damaged lysosomes by delivering cholesterol and PS (Tan and Finkel, 2022).

A recent study showed that functional lysosomes promote autophagy (Zeng et al., 2023). Autophagy and ESCRT machineries restrict mycobacterial growth in *D. discoideum* and macrophages (Mittal et al., 2018, Aylan et al., 2023b, López-Jiménez et al., 2018). In addition, the observations reported in this thesis suggest that OSBP8-mediated ER-dependent repair also reduces mycobacterial growth in *D. discoideum*. Intriguingly, the proteins involved in ER-dependent MCV/lysosomal repair are localized at ER-autolyososome MCS as well. The absence of PI4P exchange or the deficiency of any protein involved in ER-autolysosome contacts such as OSBP or Sac1 creates autophagy defects (Liu et al., 2023). Whether ER-dependent repair is linked to autophagy remains to be studied. However, preliminary data shows a slight increase of autophagy-related (Atg8a^{+}) structures in uninfected cells lacking OSBP8 (Fig. 4.3A-B). Additionally, I observed the recruitment of Atg8a^{+} structures to intracellular mycobacteria (Fig. 4.3C). Further experiments with MCV markers are critical to differentiate vacuolar mycobacteria from cytosolic mycobacteria. Additionally, whether ER-dependent MCV repair is related to an induction or block of autophagy pathway remains to be studied. These data contribute to the notion that different repair mechanisms act during infection. However, the temporal and spatial crosstalk among various repair pathways are of
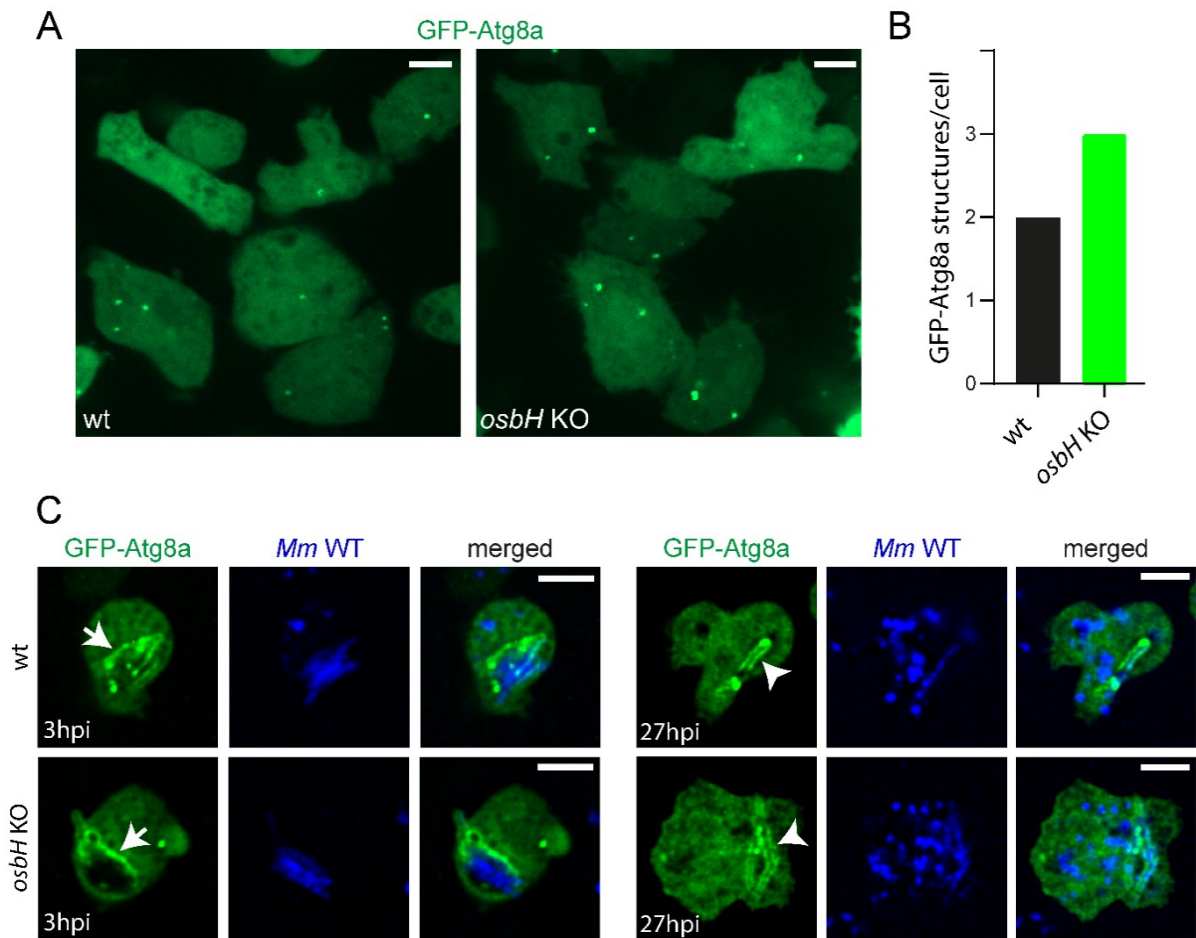
FIG 4.3 Induction of autophagosomes in uninfected (A, B) and recruitment of GFP-Atg8a to intracellular bacteria in infected cells (C). (A) Cells expressing GFP-Atg8a were analysed by SD microscopy. (B) Plots show the data (wt, n=243; *osbH* KO, n=287) of a single experiment. (C) Wt or *osbH* KO cells overexpressing GFP-Atg8a were infected with eBFP-expressing *M. marinum*. At the indicated time points samples were imaged by SD microscopy. Arrows and arrow heads indicate Atg8a⁺ intracellular mycobacteria and seemingly cytosolic mycobacteria, respectively. Shown are representative images of a single experiment. Images in C were deconvolved. Scale bars, 5 µm.

relevance for future research. To this end, experiments could be carried out in cells lacking one or multiple repair pathways.

4.5. A proposed interaction of OSBP8 with cytosolic mycobacteria

Is OSBP8 recruitment to cytosolic mycobacteria beneficial for the host or for the bacteria? Upon infection, mycobacteria undergo a metabolic shift and utilize host lipids such as sterols as a carbon source (Brzostek et al., 2009, Pandey and Sassetti, 2008). Interestingly, in *D. discoideum*, sterols accumulate in the MCV (Barisch et al., 2015b). Strikingly, we found that OSBP8 is mobilised to ER-MCV and ER-cytosolic mycobacteria MCS. Consequently, these contacts might be induced by the bacteria to get access to host sterols. Sterols might be then taken up by the transporter Mce4 (Pandey and Sassetti, 2008) and used to drive the bacterial metabolism.

On the contrary, recent studies in plants suggest that cysteine-rich non-specific LTPs operate as anti-microbial or anti-fungal agents by destroying their cell membranes or by interfering with microbial effectors (Gao et al., 2022). Additionally, previous infection studies in *D. discoideum* showed that a host lipid droplet-associated protein, perilipin (Plin), is mobilised exclusively to cytosolic *M. marinum* (Barisch et al., 2015). It was hypothesized that the amphipathic helices of Plin might interact with the hydrophobic cell wall of mycobacteria (Barisch and Soldati, 2017). In analogy to this, OSBP8 might interact with mycobacteria via its ALPS-like motif (Fig. 4.4) as this motif is crucial for organelle localization (Fig. 3.4). If OSBP8 has antimicrobial effects needs to be shown. To test this hypothesis, *in vitro* experiments with recombinant OSBP8 to monitor mycobacterial growth are required. An alternative strategy might be to generate fluorescent reporters for cytosolic *M. marinum* to monitor the fate of OSBP8 interaction as recently developed for *Salmonella* (Schulte et al., 2021, Röder et al., 2021). However, these techniques remain to be established in the model system. It is tempting to investigate whether OSBP is also recruited to cytosolic *M. tuberculosis*. However, a recent
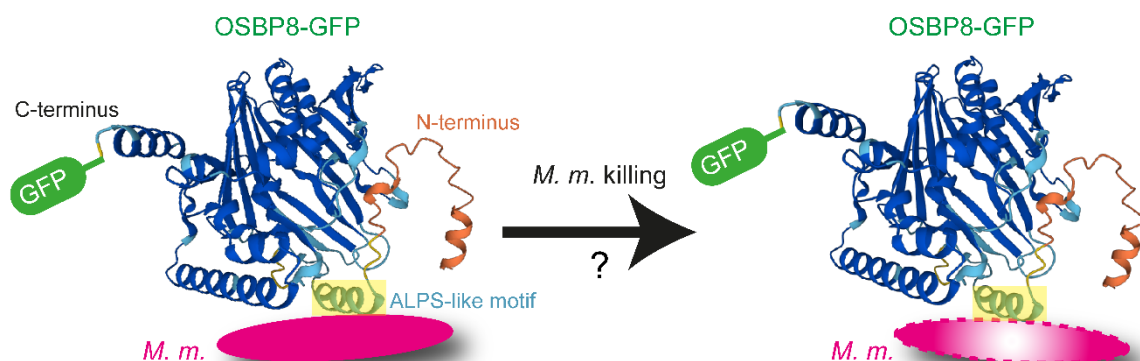

FIG 4.4 Proposed model for the interaction of OSBP8 with *M. marinum*. The ALPS-like motif of OSBP8 may have affinity for mycobacterial cell wall lipids .This interaction might be beneficial for the bacteria or for the host.

study showed that cytosolic *Rickettsia parkeri* forms contacts with the ER and this is mediated by VAP (Acevedo-Sánchez et al., 2023). To test whether VAP interacts with mycobacterial effectors or via host LTPs, pulldowns assays to identity its interacting partners and studies in *vap* KOs are essential. These experiments might provide important insights into the cytosolic stage of mycobacteria and if the contact with the ER is a beneficial interaction for the host or pathogen.

To the best of my knowledge, the recruitment of host LTP to cytosolic bacteria has not been reported so far. Thus, the discovery of OSBP8 adds novelty to this research. Moreover, it would be of great interest to investigate if host OSBPs might serve as therapeutic tools.

4.6. OSBP9 and OSBP11 as potential candidates for future investigations

OSBP9 and OSBP11 are phylogenetically close to OSBP8 (Vormittag et al., 2023). In addition, we observed that the genes encoding these proteins are upregulated during *M. marinum* infection (Hanna et al., 2019). Interestingly, OSBP9 is located on bead-containing phagosomes (Fig. 3.5A-B). It is therefore likely that OSBP9 is present on the MCV. OSBP11 is localized at the plasma membrane and not on BCPs (Fig. 3.5C-D). A recent study reported that OSBP11 mobilises to *Legionella*-containing vacuoles and is essential for intracellular *Legionella* growth in *D. discoideum* (Vormittag et al., 2023). Consequently, it is plausible that OSBP11 might be recruited to the MCV.

I observed a minor reduction in sterol accumulation in the MCV of *D. discoideum* lacking OSBP8. This suggests that OSBP9 and OSBP11 might participate in sterol transport to the MCV. If they are fostering lipid transfer required for ER-dependent repair remains to be investigated. To identify their lipid ligands, the experiments proposed earlier for OSBP8 should be carried out.

5. CONCLUSION AND OUTLOOK

Recent studies revealed that OSBP participates in ER-dependent lysosomal recovery following sterile damage. However, the induction and function of this pathway during mycobacterial infection remained unexplored. The work presented in this thesis uncovers the role of this pathway during *M. marinum* infection of *D. discoideum* and potentially also during *M. tuberculosis* infection in macrophages. 3D-HPF/FS-CLEM allowed us to visualize the morphology of ER-MCV contact sites and in addition, vacuole escape of mycobacteria in *D. discoideum*. Moreover, we found that the damage caused by the T7SS ESX-1 mobilises the ER-Golgi proteins OSBP and OSBP8 to ER-MCV contacts in human macrophages and *D. discoideum*, respectively. Although deletion of OSBP8 does not affect vacuole escape, it causes a massive accumulation of PI4P on MCV/lysosomes. This leads to a repair defect and impairs the lysosomal and proteolytic functions of the MCV promoting mycobacterial growth. Additionally, I found that OSBP8 interacts with cytosolic mycobacteria. We propose that during the cytosolic stage, OSBP8-mediated lipid transport might have the function to deliver nutrients to the bacteria or participate in host resistance.

Considering the data generated in this thesis, ER-dependent vacuole repair contributes to host resistance against intracellular pathogens such as *M. tuberculosis*. However, as discussed in the previous section, further experiments are vital to gain deeper insights of this mechanism. Firstly, *in vitro* experiments such as donor-acceptor liposome assays with recombinant OSBP8 to validate PI4P and sterols as its ligands should be performed. Secondly, testing the proposed interaction of the ALPS-like motif of OSBP8 and the mycobacterial surface could be carried out by monitoring the impact on mycobacterial growth with recombinant truncated versions of OSBP8. Thirdly, infection experiments with cells expressing OSBP9 or OSBP11 could be performed to study alternative lipid exchange routes. Fourthly, employing GFP-pull down assays or studies in *vap* KO will be helpful to challenge the proposed model for ER-MCV MCS stability and to uncover the role of VAP and its binding partner/s. Finally, unraveling the crosstalk between ER-dependent repair with other pathways and how this impacts *M. tuberculosis* growth in autophagy- or ESCRT-mutant backgrounds would also be beneficial. Collectively, this study is important to gain insights to eradicate tuberculosis in the future by providing basis for the development of host-directed therapeutics.

6. APPENDIX

6.1. List of *D. discoideum* and mammalian cells used in this study

D. discoideum strains	Relevant characteristics	Source/Reference
Ax2	wt, parental strain of *osbH* KO, *osbH* KI	
Ax2 *osbH* KO	Bsr[r]	This study
Ax2(Ka)	wt, parental strain of *tsg101* KO	
Ax2(Ka) *tsg101* KO	Bsr[r]	(Blanc et al., 2009)
Mammalian cells		
Human induced pluripotent stem cell-derived macrophages (iPSDMs)	iPSDMs were generated from human induced pluripotent stem cell line KOLF2	Public Health England Culture Collections (catalogue number 77650100)

Abbreviations: Bsr[r]: Blasticidin S resistant

6.2. List of *D. discoideum* plasmids used in this study

D. discoideum plasmids	pMIB number	Relevant characteristics	Source/Reference
OSBP8-GFP	89	pDM323-*osbH*, G418^r, Amp^r	This study
GFP-OSBP8	49	pDM317-*osbH*, G418^r, Amp^r	This study
Calnexin-mCherry	91	pDM1044-*Calnx*, Hyg^r, Amp^r	(Steiner et al., 2017)
ZntD-mCherry	57	pDM1044-*zntD*, Hyg^r, Amp^r	(Barisch et al., 2018)
AmtA-mCherry	8	pDM1044-*amtA*, Hyg^r, Amp^r	(Barisch et al., 2015)
OSBP8-mCherry	82	pDM1210-*osbH*, Hyg^r, Amp^r	This study
OSBP7-GFP	88	pDM323-*osbG*, G418^r, Amp^r	This study
P4C-mCherry		pDM1044-*p4c*, Hyg^r, Amp^r	(Vormittag et al., 2023, Steiner et al., 2017)
P4C-GFP	12	pDM323-*p4c*, G418^r, Amp^r	(Welin et al., 2018)
GFP-Vps32		pDM317-*vps32*, G418^r, Amp^r	(López-Jiménez et al., 2018)
OSBP8::GFP	173	pPI183-osbH, Hyg^r, Amp^r	This study
GFP-ABD		pDXA-GFP-ABD120, G418^r, Amp^r	(Pang et al., 1998)
OSBP11-GFP	40	pDM323-*osbK*, G418^r, Amp^r	This study
OSBP9-GFP	94	pDM1045-*osbl*, Hyg^r, Amp^r	Letourneur Lab, France
GFP-Atg8a	99	pDM1043-*atg8a*, Hyg^r, Amp^r	(López-Jiménez et al., 2018)
OSBP8 (1-57)-GFP	132	pDM323-*osbH*(1-57), G418^r, Amp^r	This study
OSBP8 (58-401)-GFP	133	pDM323-*osbH*(58-401), G418^r, Amp^r	This study

Abbreviations: Amp^r: Ampicillin resistant, Hyr^r: Hygromycin resistant, G418^r: G418 resistant

6.3. List of *D. discoideum* primers used in this study

Name	oMIB number	Sequence	Source/Reference
*osbH*_fwd	21	5'–CG AGATCT AAAATGTTTTCAGGAGCATTG–3'	This study
*osbH*_rev without stop	22	5'–CC ACTAGT ATTTGAAGCTGCTGCTTTAAC–3'	This study
*osbH*_rev with stop	23	5'–CC ACTAGT TTAATTTGAAGCTGCTGC–3'	This study
*osbG*_fwd	20	5'–CG AGATCT AAAATGGAGGCCGATCCG–3'	This study
*osbG*_rev without stop	19	5'–CC ACTAGT ATTACTACCACTTGCAGC–3'	This study
*osbG*_rev with stop	18	5'–CC ACTAGT TTAATTACTACCACTTGCAGC–3'	This study
osbH LA_fwd	56	5'–CGA GAT CTG GTT GGT TAG GTG CCG GTC G–3'	This study
osbH LA_rev	57	5'–GGA CTA GTA TTT GAA GCT GCT GCT TTA ACT CTT TCT TCT C–3'	This study
osbH RA_fwd	101	5'–CGGTCGACTAAAAACAATAATAATTATATATT TTAATC GTAAACAATTTATTCATTCAATTTCC–3'	This study
osbH RA_Rev	102	5'–GCGAGCTCGGAAATCTTGTTGGAGG–3'	This study
*osbK*_fwd	38	5'–CGT CCG GAA AAA TGT CAA ATT TTT TCA AAA AGT TAG–3'	This study
*osbK*_rev with stop	39	5'–CCA CTA GTT TAT CTA CCA CTA TGA CCA ATT G–3'	This study
*osbK*_fwd	42	5'–CGA CTA GTA AAA TGT CAA ATT TTT TCA AAA AGT TAG–3'	This study
*osbK*_rev without stop	43	5'–CCA CTA GTT CTA CCA CTA TGA CCA ATT GTA G–3'	This study
pDM317_seq fwd	40	5'–CTT GAG TTT GTA ACA GCT GCT GGG–3'	This study
pDM317_seq rev	41	5'–GAA AAT ATT AGA TTA TTA CAA CAA TTT G–3'	This study
pDM323_seq fwd	44	5'–TTC AGA TTG CAT AAA AAG–3'	This study

Name	oMIB number	Sequence	Source/Reference
pDM323_seq rev	45	5'–ATC ACC TTC ACC CTC TCC AC–3'	This study
osbH 1-57_fwd	130	5'–CGA GAT CTA AAA TGT TTT CAG GAG CAT TGA ATT ATA–3'	This study
osbH 1-57_rev without stop	132	5'–GGA CTA GTT AAT GAG ATT AAA GAT GTA ATA TCT T–3'	This study
osbH 58-401_fwd	133	5'–CGA GAT CTA AAA TGC CAG TTT GGA TTT TCG AAC CAG–3'	This study
osbH 58-401_rev without stop	134	5'–GGA CTA GTA TTT GAA GCT GCT GCT TTA ACT C–3'	This study

6.4. List of antibodies used in this study

Primary Antibody	Working concentration	Target	Host	Source, reference number
p80 (H161)	1:50	endosomes	mouse (mAb)	Geneva antibody facility, AJ154-M2a
anti-VatA (α-H+-ATPase)	1:50	lysosomes, contractile vacuole	human (mAb)	Geneva antibody facility, AJ520-H1
α-Protein-disulfidisomerase (PDI)	undiluted	endoplasmic reticulum	mouse (mAb)	Maniak lab (University of Kassel) Monnat et al., 1997
p80 (H161)	1:50	endosomes	human (mAb)	Geneva antibody facility, AJ154-H1
anti-vacA (Vacuolin A)	1:50	endosomes	mouse (mAb)	Geneva antibody facility, RB256-M2a
anti-GFP	1:500	-	rabbit (pAb)	BIOZOL/MBL, MBL-598
Mono- and poly-ubiquitinylated conjugates (FK2)	1:1000	ubiquitin	mouse (mAb)	Enzo, ENZ-ABS840

Secondary Antibody	Working concentration	Target	Host	Source, reference number
CF488A IgG (H+L)	1:500	mouse	goat	Biotium, BOT-20018
CF568 IgG (H+L)	1:500	mouse	goat	Biotium, BOT-20101
CF640R IgG (H+L)	1:500	human	goat	Biotium, BOT-20081-1
CF488A IgG (H+L)	1:500	rabbit	goat	Biotium, BOT-20019
CF640R IgG (H+L)	1:500	mouse	goat	Biotium, BOT-20175

6.5. List of mycobacteria strains used in this study

M. marinum strains	Relevant characteristics	Source/Reference
M. marinum M	wt, parental strain	L. Ramakrishnan (University of Cambridge)
M. marinum ΔRD1	RD1 locus deletion mutant	L. Ramakrishnan (University of Cambridge)
M. marinum ΔCE	*esxA* and *esxB* deletion mutant	T. Soldati (University of Geneva)
M. marinum Δ*tesA*	*Tn5370* transposon inserted	(Alibaud et al., 2011)
M. marinum Δtpd	triple phosphatase mutant	(Koliwer-Brandl et al., 2019)

M. tuberculosis strains		
M. tuberculosis	H37Rv	Douglas Young (The Francis Crick Institute, London, UK)
M. tuberculosis ΔRD1	H37Rv ΔRD1	Suzie Hingley-Wilson (University of Surrey, Guilford, UK),

6.6. List of mycobacteria plasmids used in this study

Mycobacteria Plasmids	Relevant characteristics	Source/Reference
pTEC18	eBFP2 under control of the MSP promoter, Hyg[r], Amp[r]	Addgene #30177, (Takaki et al., 2013)
pCherry10	mCherry under control of the G13 promoter, Hyg[r], Amp[r]	Addgene #24664, (Carroll et al., 2010)
pTEC19	E2-Crimson under the control of the MSP promotor, Hyg[r], Amp[r]	Addgene #30178, (Takaki et al., 2013)
pmsp12::GFP	GFP production under control of *M. marinum* msp12 promoter, Kan[r]	(Cosma et al., 2004)

Abbreviations: Amp[r]: Ampicillin resistant, Hyr[r]: Hygromycin resistant, Kan[r]: Kanamycin resistant

6.7. List of figures

6.8. Abbreviations

ABD- actin-binding-domain
ALPS- amphipathic lipid packing sensor
AmtA- ammonium transporter
Atg- autophagy
AX- axenic
BCP- bead-containing phagosome
BSL- biosafety level
Bsr^r: blasticidin S resistant
Ca^{2+}- calcium ion
CLEM- correlative light and electron microscopy
DQ-BSA- dye-quenched-bovine serum albumin
EM- electron microscopy
ER- endoplasmic reticulum
ESCRT- endosomal sorting complex required for transport
EsxA- early secreted antigenic target 1 (ESAT-6)
EsxB- culture filtrate protein 10 (CFP10)
ET- electron tomography
ExM- expansion microscopy
FFAT- two phenylalanines in an acidic tract
FIB-SEM- focused ion beam scanning electron microscopy
FS- freeze substitution
GFP- green fluorescent protein
HPF- high pressure freezing
ILVs- intraluminal vesicles
iPSDMs- induced pluripotent stem cell (iPSC)-derived macrophages
KIs- knockins
KOs- knockouts
LAM- lipoarabinomannan
LDs- lipid droplets
LLOMe- L-leucyl-L-leucine methyl ester
LLSM- lattice light sheet microscopy
LM- light microscopy
LTPs- lipid transfer proteins
MCS- membrane contact sites
MCV- *Mycobacterium*-containing vacuole
ORD- OSBP-related domain
ORP- oxysterol binding protein related protein
OSBP- oxysterol binding protein
Osh- oxysterol binding protein homologue
PDIM- phthiocerol dimycoserosate
PH- pleckstrin homology
PI4K- PI4-kinase
PI4K2A- PI4-kinase type 2-alpha
PI4P- phosphatidylinositol 4-phosphate
PIM- phosphatidylinositol mannoside
PIP- phosphatidylinositol phosphate
PLIN- perilipin
PLL- poly-l-lysine
PS- phosphatidylserine
PtpA- protein tyrosine phosphatase A
RD1- region of difference 1
SapM- secreted acid phosphatase
SBF-SEM- serial block face-scanning electron microscopy
SM- sphingomyelin
SMase- sphingomyelinase
STARD- steroidogenic Acute Regulatory Protein-related Lipid Transfer Domain
T7SS- type VII secretion systems
TB- tuberculosis
TDM- mycobacterial trehalose-6, 6- dimycolate
TEM- transmission electron microscopy
VAP- vesicle-associated membrane protein (VAMP)-associated protein
Vps- vacuolar protein-sorting
wt- wild type

6.9. List of publications

VORMITTAG, S., HÜSLER, D., HANEBURGER, I., KRONIGER, T., **ANAND, A**., PRANTL, M., BARISCH, C., MAAß, S., BECHER, D., LETOURNEUR, F. & HILBI, H. 2023. Legionella- and host-driven lipid flux at LCV-ER membrane contact sites promotes vacuole remodeling. *EMBO Rep,* 24**,** e56007.

ANAND, A., MAZUR, A.-C., ROSELL-AREVALO, P., FRANZKOCH, R., BREITSPRECHER, L., LISTIAN, S. A., HÜTTEL, S. V., MÜLLER, D., SCHÄFER, D. G., VORMITTAG, S., HILBI, H., MANIAK, M., GUTIERREZ, M. G. & BARISCH, C. 2023. ER-dependent membrane repair of mycobacteria-induced vacuole damage. *bioRxiv***,** 2023.04.17.537276. (in press @*mbio*)

FRANZKOCH, R., **ANAND, A.**, BREITSPRECHER, L., PSATHAKI, O. E. & BARISCH, C. 2023. Resolving exit strategies of mycobacteria by combining high-pressure freezing with 3D-correlative light and electron microscopy. *bioRxiv***,** 2023.04.24.538041. (under revision @*Mol Micro*)

7. REFERENCES

ACEVEDO-SÁNCHEZ, Y., WOIDA, P. J., KRAEMER, S. & LAMASON, R. L. 2023. An obligate intracellular bacterial pathogen forms a direct, interkingdom membrane contact site. *bioRxiv*, 2023.06.05.543771.

ALIBAUD, L., ROMBOUTS, Y., TRIVELLI, X., BURGUIÈRE, A., CIRILLO, S. L., CIRILLO, J. D., DUBREMETZ, J. F., GUÉRARDEL, Y., LUTFALLA, G. & KREMER, L. 2011. A Mycobacterium marinum TesA mutant defective for major cell wall-associated lipids is highly attenuated in Dictyostelium discoideum and zebrafish embryos. *Mol Microbiol,* 80**,** 919-34.

AMARAL, E. P., COSTA, D. L., NAMASIVAYAM, S., RITEAU, N., KAMENYEVA, O., MITTEREDER, L., MAYER-BARBER, K. D., ANDRADE, B. B. & SHER, A. 2019. A major role for ferroptosis in Mycobacterium tuberculosis-induced cell death and tissue necrosis. *J Exp Med,* 216**,** 556-570.

ANAND, A., MAZUR, A.-C., ROSELL-AREVALO, P., FRANZKOCH, R., BREITSPRECHER, L., LISTIAN, S. A., HÜTTEL, S. V., MÜLLER, D., SCHÄFER, D. G., VORMITTAG, S., HILBI, H., MANIAK, M., GUTIERREZ, M. G. & BARISCH, C. 2023. ER-dependent membrane repair of mycobacteria-induced vacuole damage. *bioRxiv*, 2023.04.17.537276.

ANTONNY, B., BIGAY, J. & MESMIN, B. 2018. The Oxysterol-Binding Protein Cycle: Burning Off PI(4)P to Transport Cholesterol. *Annu Rev Biochem,* 87**,** 809-837.

ARAFAH, S., KICKA, S., TROFIMOV, V., HAGEDORN, M., ANDREU, N., WILES, S., ROBERTSON, B. & SOLDATI, T. 2013. Setting up and monitoring an infection of Dictyostelium discoideum with mycobacteria. *Methods Mol Biol,* 983**,** 403-17.

ARMSTRONG, J. A. & HART, P. D. 1971. Response of cultured macrophages to Mycobacterium tuberculosis, with observations on fusion of lysosomes with phagosomes. *J Exp Med,* 134**,** 713-40.

AUGENSTREICH, J., ARBUES, A., SIMEONE, R., HAANAPPEL, E., WEGENER, A., SAYES, F., LE CHEVALIER, F., CHALUT, C., MALAGA, W., GUILHOT, C., BROSCH, R. & ASTARIE-DEQUEKER, C. 2017. ESX-1 and phthiocerol dimycocerosates of Mycobacterium tuberculosis act in concert to cause phagosomal rupture and host cell apoptosis. *Cell Microbiol,* 19.

AUGENSTREICH, J. & BRIKEN, V. 2020. Host Cell Targets of Released Lipid and Secreted Protein Effectors of Mycobacterium tuberculosis. *Front Cell Infect Microbiol,* 10**,** 595029.

AUGENSTREICH, J., HAANAPPEL, E., FERRÉ, G., CZAPLICKI, G., JOLIBOIS, F., DESTAINVILLE, N., GUILHOT, C., MILON, A., ASTARIE-DEQUEKER, C. & CHAVENT, M. 2019. The conical shape of DIM lipids promotes Mycobacterium tuberculosis infection of macrophages. *Proc Natl Acad Sci U S A,* 116**,** 25649-25658.

AUGENSTREICH, J., HAANAPPEL, E., SAYES, F., SIMEONE, R., GUILLET, V., MAZERES, S., CHALUT, C., MOUREY, L., BROSCH, R., GUILHOT, C. & ASTARIE-DEQUEKER, C. 2020. Phthiocerol Dimycocerosates From Mycobacterium tuberculosis Increase the Membrane Activity of Bacterial Effectors and Host Receptors. *Front Cell Infect Microbiol,* 10**,** 420.

AUWETER, S. D., YU, H. B., ARENA, E. T., GUTTMAN, J. A. & FINLAY, B. B. 2012. Oxysterol-binding protein (OSBP) enhances replication of intracellular Salmonella and binds the Salmonella SPI-2 effector SseL via its N-terminus. *Microbes Infect,* 14**,** 148-54.

AW, Y. C., BROWN, A. J., WU, J.-W. & YANG, H. 2020. ORP1L, ORP1S, and ORP2: Lipid Sensors and Transporters. *Contact,* 3**,** 2515256420956818.

AYLAN, B., BERNARD, E. M., PELLEGRINO, E., BOTELLA, L., FEARNS, A., ATHANASIADI, N., BUSSI, C., SANTUCCI, P. & GUTIERREZ, M. G. 2023a. ATG7 and ATG14 restrict cytosolic and phagosomal Mycobacterium tuberculosis replication in human macrophages. *Nat Microbiol,* 8**,** 803-818.

AYLAN, B., BERNARD, E. M., PELLEGRINO, E., BOTELLA, L., FEARNS, A., ATHANASIADI, N., BUSSI, C., SANTUCCI, P. & GUTIERREZ, M. G. 2023b. ATG7 and ATG14 restrict cytosolic and phagosomal Mycobacterium tuberculosis replication in human macrophages. *Nat Microbiol*.

BALLA, A., TUYMETOVA, G., BARSHISHAT, M., GEISZT, M. & BALLA, T. 2002. Characterization of type II phosphatidylinositol 4-kinase isoforms reveals association of the enzymes with endosomal vesicular compartments. *J Biol Chem,* 277**,** 20041-50.

BARISCH, C., HOLTHUIS, J. C. M. & COSENTINO, K. 2023. Membrane damage and repair: a thin line between life and death. *Biol Chem*.

BARISCH, C., KALININA, V., LEFRANÇOIS, L. H., APPIAH, J., LÓPEZ-JIMÉNEZ, A. T. & SOLDATI, T. 2018. Localization of all four ZnT zinc transporters in Dictyostelium and impact of ZntA and ZntB knockout on bacteria killing. *J Cell Sci,* 131.

BARISCH, C., LÓPEZ-JIMÉNEZ, A. T. & SOLDATI, T. 2015a. Live imaging of Mycobacterium marinum infection in Dictyostelium discoideum. *Methods Mol Biol,* 1285**,** 369-85.

BARISCH, C., PASCHKE, P., HAGEDORN, M., MANIAK, M. & SOLDATI, T. 2015b. Lipid droplet dynamics at early stages of Mycobacterium marinum infection in Dictyostelium. *Cell Microbiol,* 17**,** 1332-49.

BARISCH, C. & SOLDATI, T. 2017a. Breaking fat! How mycobacteria and other intracellular pathogens manipulate host lipid droplets. *Biochimie,* 141**,** 54-61.

BARISCH, C. & SOLDATI, T. 2017b. Mycobacterium marinum Degrades Both Triacylglycerols and Phospholipids from Its Dictyostelium Host to Synthesise Its Own Triacylglycerols and Generate Lipid Inclusions. *PLoS Pathog,* 13**,** e1006095.

BECKWITH, M. S., BECKWITH, K. S., SIKORSKI, P., SKOGAKER, N. T., FLO, T. H. & HALAAS, Ø. 2015. Seeing a Mycobacterium-Infected Cell in Nanoscale 3D: Correlative Imaging by Light Microscopy and FIB/SEM Tomography. *PLoS One,* 10**,** e0134644.

BEDARD, M., VAN DER NIET, S., BERNARD, E. M., BABUNOVIC, G., CHENG, T. Y., AYLAN, B., GROOTEMAAT, A. E., RAMAN, S., BOTELLA, L., ISHIKAWA, E., O'SULLIVAN, M. P., O'LEARY, S., MAYFIELD, J. A., BUTER, J., MINNAARD, A. J., FORTUNE, S. M., MURPHY, L. O., ORY, D. S., KEANE, J., YAMASAKI, S., GUTIERREZ, M. G., VAN DER WEL, N. & MOODY, D. B. 2023. A terpene nucleoside from M. tuberculosis induces lysosomal lipid storage in foamy macrophages. *J Clin Invest,* 133.

BERESFORD, N., PATEL, S., ARMSTRONG, J., SZÖOR, B., FORDHAM-SKELTON, A. P. & TABERNERO, L. 2007. MptpB, a virulence factor from Mycobacterium tuberculosis, exhibits triple-specificity phosphatase activity. *Biochem J,* 406**,** 13-8.

BERNARD, E. M., FEARNS, A., BUSSI, C., SANTUCCI, P., PEDDIE, C. J., LAI, R. J., COLLINSON, L. M. & GUTIERREZ, M. G. 2020. M. tuberculosis infection of human iPSC-derived macrophages reveals complex membrane dynamics during xenophagy evasion. *J Cell Sci,* 134.

BLANC, C., CHARETTE, S. J., MATTEI, S., AUBRY, L., SMITH, E. W., COSSON, P. & LETOURNEUR, F. 2009. Dictyostelium Tom1 participates to an ancestral ESCRT-0 complex. *Traffic,* 10**,** 161-71.

BOTTAI, D., DI LUCA, M., MAJLESSI, L., FRIGUI, W., SIMEONE, R., SAYES, F., BITTER, W., BRENNAN, M. J., LECLERC, C., BATONI, G., CAMPA, M., BROSCH, R. & ESIN, S. 2012. Disruption of the ESX-5 system of Mycobacterium tuberculosis causes loss of PPE protein secretion, reduction of cell wall integrity and strong attenuation. *Mol Microbiol,* 83**,** 1195-209.

BOULAIS, J., TROST, M., LANDRY, C. R., DIECKMANN, R., LEVY, E. D., SOLDATI, T., MICHNICK, S. W., THIBAULT, P. & DESJARDINS, M. 2010. Molecular characterization of the evolution of phagosomes. *Mol Syst Biol,* 6**,** 423.

BRÖCKER, C., KUHLEE, A., GATSOGIANNIS, C., BALDERHAAR, H. J., HÖNSCHER, C., ENGELBRECHT-VANDRÉ, S., UNGERMANN, C. & RAUNSER, S. 2012. Molecular architecture of the multisubunit homotypic fusion and vacuole protein sorting (HOPS) tethering complex. *Proc Natl Acad Sci U S A,* 109**,** 1991-6.

BRZOSTEK, A., PAWELCZYK, J., RUMIJOWSKA-GALEWICZ, A., DZIADEK, B. & DZIADEK, J. 2009. Mycobacterium tuberculosis is able to accumulate and utilize cholesterol. *J Bacteriol,* 191**,** 6584-91.

BUSSI, C. & GUTIERREZ, M. G. 2019. Mycobacterium tuberculosis infection of host cells in space and time. *FEMS Microbiol Rev,* 43**,** 341-361.

CARDENAL-MUÑOZ, E., ARAFAH, S., LÓPEZ-JIMÉNEZ, A. T., KICKA, S., FALAISE, A., BACH, F., SCHAAD, O., KING, J. S., HAGEDORN, M. & SOLDATI, T. 2017a. Mycobacterium marinum antagonistically induces an autophagic response while repressing the autophagic flux in a TORC1- and ESX-1-dependent manner. *PLoS Pathog,* 13**,** e1006344.

CARDENAL-MUÑOZ, E., BARISCH, C., LEFRANÇOIS, L. H., LÓPEZ-JIMÉNEZ, A. T. & SOLDATI, T. 2017b. When Dicty Met Myco, a (Not So) Romantic Story about One Amoeba and Its Intracellular Pathogen. *Front Cell Infect Microbiol,* 7**,** 529.

CARROLL, P., SCHREUDER, L. J., MUWANGUZI-KARUGABA, J., WILES, S., ROBERTSON, B. D., RIPOLL, J., WARD, T. H., BANCROFT, G. J., SCHAIBLE, U. E. & PARISH, T. 2010. Sensitive detection of gene expression in mycobacteria under replicating and non-replicating conditions using optimized far-red reporters. *PLoS One,* 5**,** e9823.

COSMA, C. L., HUMBERT, O. & RAMAKRISHNAN, L. 2004. Superinfecting mycobacteria home to established tuberculous granulomas. Nat Immunol, 5, 828-35.

CHANDRA, P., GRIGSBY, S. J. & PHILIPS, J. A. 2022. Immune evasion and provocation by Mycobacterium tuberculosis. *Nat Rev Microbiol,* 20**,** 750-766.

CHARMAN, M., COLBOURNE, T. R., PIETRANGELO, A., KREPLAK, L. & RIDGWAY, N. D. 2014. Oxysterol-binding protein (OSBP)-related protein 4 (ORP4) is essential for cell proliferation and survival. *J Biol Chem,* 289**,** 15705-17.

CHATTERJEE, A. 2023. Mycobacterium tuberculosis and its secreted tyrosine phosphatases. *Biochimie,* 212**,** 41-47.

CHEN, B. C., LEGANT, W. R., WANG, K., SHAO, L., MILKIE, D. E., DAVIDSON, M. W., JANETOPOULOS, C., WU, X. S., HAMMER, J. A., 3RD, LIU, Z., ENGLISH, B. P., MIMORI-KIYOSUE, Y., ROMERO, D. P., RITTER, A. T., LIPPINCOTT-SCHWARTZ, J., FRITZ-LAYLIN, L., MULLINS, R. D., MITCHELL, D. M., BEMBENEK, J. N., REYMANN, A. C., BÖHME, R., GRILL, S. W., WANG, J. T., SEYDOUX, G., TULU, U. S., KIEHART, D. P. & BETZIG, E. 2014. Lattice light-sheet microscopy: imaging molecules to embryos at high spatiotemporal resolution. *Science,* 346**,** 1257998.

CHISHOLM, R. L., GAUDET, P., JUST, E. M., PILCHER, K. E., FEY, P., MERCHANT, S. N. & KIBBE, W. A. 2006. dictyBase, the model organism database for Dictyostelium discoideum. *Nucleic Acids Res,* 34**,** D423-7.

COOKE, I. R. & DESERNO, M. 2006. Coupling between lipid shape and membrane curvature. *Biophys J,* 91**,** 487-95.

COSMA, C. L., HUMBERT, O. & RAMAKRISHNAN, L. 2004. Superinfecting mycobacteria home to established tuberculous granulomas. *Nat Immunol,* 5**,** 828-35.

DE BRITO, O. M. & SCORRANO, L. 2008. Mitofusin 2 tethers endoplasmic reticulum to mitochondria. *Nature,* 456**,** 605-10.

DE JONGE, M. I., PEHAU-ARNAUDET, G., FRETZ, M. M., ROMAIN, F., BOTTAI, D., BRODIN, P., HONORÉ, N., MARCHAL, G., JISKOOT, W., ENGLAND, P., COLE, S. T. & BROSCH, R. 2007. ESAT-6 from Mycobacterium tuberculosis dissociates from its putative chaperone CFP-10 under acidic conditions and exhibits membrane-lysing activity. *J Bacteriol,* 189**,** 6028-34.

DE SAINT-JEAN, M., DELFOSSE, V., DOUGUET, D., CHICANNE, G., PAYRASTRE, B., BOURGUET, W., ANTONNY, B. & DRIN, G. 2011. Osh4p exchanges sterols for phosphatidylinositol 4-phosphate between lipid bilayers. *J Cell Biol,* 195**,** 965-78.

DECOSTERE, A., HERMANS, K. & HAESEBROUCK, F. 2004. Piscine mycobacteriosis: a literature review covering the agent and the disease it causes in fish and humans. *Vet Microbiol,* 99**,** 159-66.

DESJARDINS, M. 1995. Biogenesis of phagolysosomes: the 'kiss and run' hypothesis. *Trends Cell Biol,* 5**,** 183-6.

DI MATTIA, T., MARTINET, A., IKHLEF, S., MCEWEN, A. G., NOMINÉ, Y., WENDLING, C., POUSSIN-COURMONTAGNE, P., VOILQUIN, L., EBERLING, P., RUFFENACH, F., CAVARELLI, J., SLEE, J., LEVINE, T. P., DRIN, G., TOMASETTO, C. & ALPY, F. 2020. FFAT motif phosphorylation controls formation and lipid transfer function of inter-organelle contacts. *Embo j,* 39**,** e104369.

DRIN, G., CASELLA, J. F., GAUTIER, R., BOEHMER, T., SCHWARTZ, T. U. & ANTONNY, B. 2007. A general amphipathic alpha-helical motif for sensing membrane curvature. *Nat Struct Mol Biol,* 14**,** 138-46.

EICHINGER, L., PACHEBAT, J. A., GLÖCKNER, G., RAJANDREAM, M. A. , SUCGANG, R., BERRIMAN, M., SONG, J., OLSEN, R., SZAFRANSKI, K., XU, Q., TUNGGAL, B., KUMMERFELD, S., MADERA, M., KONFORTOV, B. A., RIVERO, F., BANKIER, A. T., LEHMANN, R., HAMLIN, N., DAVIES, R., GAUDET, P., FEY, P., PILCHER, K., CHEN, G., SAUNDERS, D., SODERGREN, E., DAVIS, P., KERHORNOU, A., NIE, X., HALL, N., ANJARD, C., HEMPHILL, L., BASON, N., FARBROTHER, P., DESANY, B., JUST, E., MORIO, T., ROST, R., CHURCHER, C., COOPER, J., HAYDOCK, S., VAN DRIESSCHE, N., CRONIN, A., GOODHEAD, I., MUZNY, D., MOURIER, T., PAIN, A., LU, M., HARPER, D., LINDSAY, R., HAUSER, H., JAMES, K., QUILES, M., MADAN BABU, M., SAITO, T., BUCHRIESER, C., WARDROPER, A., FELDER, M., THANGAVELU, M., JOHNSON, D., KNIGHTS, A., LOULSEGED, H., MUNGALL, K., OLIVER, K., PRICE, C., QUAIL, M. A., URUSHIHARA, H., HERNANDEZ, J., RABBINOWITSCH, E., STEFFEN, D., SANDERS, M., MA, J., KOHARA, Y., SHARP, S., SIMMONDS, M., SPIEGLER, S., TIVEY, A., SUGANO, S., WHITE, B., WALKER, D., WOODWARD, J., WINCKLER, T., TANAKA, Y., SHAULSKY, G., SCHLEICHER, M., WEINSTOCK, G., ROSENTHAL, A., COX, E. C., CHISHOLM, R. L., GIBBS, R., LOOMIS, W. F., PLATZER, M., KAY, R. R., WILLIAMS, J., DEAR, P. H., NOEGEL, A. A., BARRELL, B. & KUSPA, A. 2005. The genome of the social amoeba Dictyostelium discoideum. *Nature,* 435**,** 43-57.

FAAS, F. G., BÁRCENA, M., AGRONSKAIA, A. V., GERRITSEN, H. C., MOSCICKA, K. B., DIEBOLDER, C. A., VAN DRIEL, L. F., LIMPENS, R. W., BOS, E., RAVELLI, R. B., KONING, R. I. & KOSTER, A. J. 2013. Localization of fluorescently labeled structures in frozen-hydrated samples using integrated light electron microscopy. *J Struct Biol,* 181**,** 283-90.

FLANNAGAN, R. S., JAUMOUILLÉ, V. & GRINSTEIN, S. 2012. The cell biology of phagocytosis. *Annu Rev Pathol,* 7**,** 61-98.

FOUNTAIN, A., INPANATHAN, S., ALVES, P., VERDAWALA, M. B. & BOTELHO, R. J. 2021. Phagosome maturation in macrophages: Eat, digest, adapt, and repeat. *Adv Biol Regul,* 82**,** 100832.

FRANZKOCH, R., ANAND, A., BREITSPRECHER, L., PSATHAKI, O. E. & BARISCH, C. 2023. Resolving exit strategies of mycobacteria by combining high-pressure freezing with 3D-correlative light and electron microscopy. *bioRxiv,* 2023.04.24.538041.

FRATTI, R. A., BACKER, J. M., GRUENBERG, J., CORVERA, S. & DERETIC, V. 2001. Role of phosphatidylinositol 3-kinase and Rab5 effectors in phagosomal biogenesis and mycobacterial phagosome maturation arrest. *J Cell Biol,* 154**,** 631-44.

FU, X., NING, J., ZHONG, Z., AMBROSE, Z., CHARLES WATKINS, S. & ZHANG, P. 2019. AutoCLEM: An Automated Workflow for Correlative Live-Cell Fluorescence Microscopy and Cryo-Electron Tomography. *Sci Rep,* 9**,** 19207.

GALMES, R., TEN BRINK, C., OORSCHOT, V., VEENENDAAL, T., JONKER, C., VAN DER SLUIJS, P. & KLUMPERMAN, J. 2015. Vps33B is required for delivery of endocytosed cargo to lysosomes. *Traffic,* 16**,** 1288-305.

GAO, H., MA, K., JI, G., PAN, L. & ZHOU, Q. 2022. Lipid transfer proteins involved in plant-pathogen interactions and their molecular mechanisms. *Mol Plant Pathol,* 23**,** 1815-1829.

GAO, L. Y., GUO, S., MCLAUGHLIN, B., MORISAKI, H., ENGEL, J. N. & BROWN, E. J. 2004. A mycobacterial virulence gene cluster extending RD1 is required for cytolysis, bacterial spreading and ESAT-6 secretion. *Mol Microbiol,* 53**,** 1677-93.

GERSTENMAIER, L., PILLA, R., HERRMANN, L., HERRMANN, H., PRADO, M., VILLAFANO, G. J., KOLONKO, M., REIMER, R., SOLDATI, T., KING, J. S. & HAGEDORN, M. 2015. The autophagic machinery ensures nonlytic transmission of mycobacteria. *Proc Natl Acad Sci U S A,* 112**,** E687-92.

GOTTHARDT, D., WARNATZ, H. J., HENSCHEL, O., BRÜCKERT, F., SCHLEICHER, M. & SOLDATI, T. 2002. High-resolution dissection of phagosome maturation reveals distinct membrane trafficking phases. *Mol Biol Cell,* 13**,** 3508-20.

GREENWOOD, D. J., DOS SANTOS, M. S., HUANG, S., RUSSELL, M. R. G., COLLINSON, L. M., MACRAE, J. I., WEST, A., JIANG, H. & GUTIERREZ, M. G. 2019. Subcellular antibiotic visualization reveals a dynamic drug reservoir in infected macrophages. *Science,* 364**,** 1279-1282.

GUTIERREZ, M. G., MASTER, S. S., SINGH, S. B., TAYLOR, G. A., COLOMBO, M. I. & DERETIC, V. 2004. Autophagy is a defense mechanism inhibiting BCG and Mycobacterium tuberculosis survival in infected macrophages. *Cell,* 119**,** 753-66.

HABERKANT, P. & HOLTHUIS, J. C. 2014. Fat & fabulous: bifunctional lipids in the spotlight. *Biochim Biophys Acta,* 1841**,** 1022-30.

HAGEDORN, M., ROHDE, K. H., RUSSELL, D. G. & SOLDATI, T. 2009. Infection by tubercular mycobacteria is spread by nonlytic ejection from their amoeba hosts. *Science,* 323**,** 1729-33.

HAGEDORN, M. & SOLDATI, T. 2007. Flotillin and RacH modulate the intracellular immunity of Dictyostelium to Mycobacterium marinum infection. *Cell Microbiol,* 9**,** 2716-33.

HANNA, N., BURDET, F., MELOTTI, A., BOSMANI, C., KICKA, S., HILBI, H., COSSON, P., PAGNI, M. & SOLDATI, T. 2019. Time-resolved RNA-seq profiling of the infection of Dictyostelium discoideum by Mycobacterium marinum reveals an integrated host response to damage and stress. *bioRxiv***,** 590810.

HANNA, N., KOLIWER-BRANDL, H., LEFRANÇOIS, L. H., KALININA, V., CARDENAL-MUÑOZ, E., APPIAH, J., LEUBA, F., GUEHO, A., HILBI, H., SOLDATI, T. & BARISCH, C. 2021. Zn(2+) Intoxication of Mycobacterium marinum during Dictyostelium discoideum Infection Is Counteracted by Induction of the Pathogen Zn(2+) Exporter CtpC. *mBio,* 12.

HE, N., DEPTA, L., ROSSETTI, C., CIGLER, M., MICHON, M., DAN, O. R., HOOCK, J., BARBIER, J., GILLET, D., FORRESTER, A., WINTER, G. E. & LARAIA, L. 2023. Selective inhibition of OSBP blocks retrograde trafficking by inducing partial Golgi degradation. *bioRxiv***,** 2023.04.01.534865.

HENMI, Y., MORIKAWA, Y., OE, N., IKEDA, N., FUJITA, A., TAKEI, K., MINOGUE, S. & TANABE, K. 2016. PtdIns4KIIα generates endosomal PtdIns(4)P and is required for receptor sorting at early endosomes. *Mol Biol Cell,* 27**,** 990-1001.

HUYNH, K. K., ESKELINEN, E. L., SCOTT, C. C., MALEVANETS, A., SAFTIG, P. & GRINSTEIN, S. 2007. LAMP proteins are required for fusion of lysosomes with phagosomes. *Embo j,* 26**,** 313-24.

INDRIGO, J., HUNTER, R. L. & ACTOR, J. K. 2003. Cord factor trehalose 6,6'-dimycolate (TDM) mediates trafficking events during mycobacterial infection of murine macrophages. *Microbiology (Reading),* 149**,** 2049-2059.

JANI, R. A., DI CICCO, A., KEREN-KAPLAN, T., VALE-COSTA, S., HAMAOUI, D., HURBAIN, I., TSAI, F. C., DI MARCO, M., MACÉ, A. S., ZHU, Y., AMORIM, M. J., BASSEREAU, P., BONIFACINO, J. S., SUBTIL, A., MARKS, M. S., LÉVY, D., RAPOSO, G. & DELEVOYE, C. 2022. PI4P and BLOC-1 remodel endosomal membranes into tubules. *J Cell Biol,* 221.

JIA, K., THOMAS, C., AKBAR, M., SUN, Q., ADAMS-HUET, B., GILPIN, C. & LEVINE, B. 2009. Autophagy genes protect against Salmonella typhimurium infection and mediate insulin signaling-regulated pathogen resistance. *Proc Natl Acad Sci U S A,* 106**,** 14564-9.

JOHANSSON, M., BOCHER, V., LEHTO, M., CHINETTI, G., KUISMANEN, E., EHNHOLM, C., STAELS, B. & OLKKONEN, V. M. 2003. The two variants of oxysterol binding protein-related protein-1 display different tissue expression patterns, have different intracellular localization, and are functionally distinct. *Mol Biol Cell,* 14**,** 903-15.

JUN, S., RO, H. J., BHARDA, A., KIM, S. I., JEOUNG, D. & JUNG, H. S. 2019. Advances in Cryo-Correlative Light and Electron Microscopy: Applications for Studying Molecular and Cellular Events. *Protein J,* 38**,** 609-615.

JUSTIS, A. V., HANSEN, B., BEARE, P. A., KING, K. B., HEINZEN, R. A. & GILK, S. D. 2017. Interactions between the Coxiella burnetii parasitophorous vacuole and the endoplasmic reticulum involve the host protein ORP1L. *Cell Microbiol,* 19.

KATZMANN, D. J., STEFAN, C. J., BABST, M. & EMR, S. D. 2003. Vps27 recruits ESCRT machinery to endosomes during MVB sorting. *J Cell Biol,* 162**,** 413-23.

KIM, G. H., DAYAM, R. M., PRASHAR, A., TEREBIZNIK, M. & BOTELHO, R. J. 2014. PIKfyve inhibition interferes with phagosome and endosome maturation in macrophages. *Traffic,* 15**,** 1143-63.

KIRSTEN, J. H., XIONG, Y., DAVIS, C. T. & SINGLETON, C. K. 2008. Subcellular localization of ammonium transporters in Dictyostelium discoideum. *BMC Cell Biol,* 9**,** 71.

KOLIWER-BRANDL, H., KNOBLOCH, P., BARISCH, C., WELIN, A., HANNA, N., SOLDATI, T. & HILBI, H. 2019. Distinct Mycobacterium marinum phosphatases determine pathogen vacuole phosphoinositide pattern, phagosome maturation, and escape to the cytosol. *Cell Microbiol,* 21**,** e13008.

KOLODZIEJEK, A. M., ALTURA, M. A., FAN, J., PETERSEN, E. M., COOK, M., BRZOVIC, P. S. & MILLER, S. I. 2019. Salmonella Translocated Effectors Recruit OSBP1 to the Phagosome to Promote Vacuolar Membrane Integrity. *Cell Rep,* 27**,** 2147-2156.e5.

KOMMNICK, C., LEPPER, A. & HENSEL, M. 2019. Correlative light and scanning electron microscopy (CLSEM) for analysis of bacterial infection of polarized epithelial cells. *Sci Rep,* 9**,** 17079.

LEE, H. J., WOO, Y., HAHN, T. W., JUNG, Y. M. & JUNG, Y. J. 2020. Formation and Maturation of the Phagosome: A Key Mechanism in Innate Immunity against Intracellular Bacterial Infection. *Microorganisms,* 8.

LEHTO, M., LAITINEN, S., CHINETTI, G., JOHANSSON, M., EHNHOLM, C., STAELS, B., IKONEN, E. & OLKKONEN, V. M. 2001. The OSBP-related protein family in humans. *J Lipid Res,* 42**,** 1203-13.

LERNER, T. R., DE SOUZA CARVALHO-WODARZ, C., REPNIK, U., RUSSELL, M. R., BOREL, S., DIEDRICH, C. R., ROHDE, M., WAINWRIGHT, H., COLLINSON, L. M., WILKINSON, R. J., GRIFFITHS, G. & GUTIERREZ, M. G. 2016. Lymphatic endothelial cells are a replicative niche for Mycobacterium tuberculosis. *J Clin Invest,* 126**,** 1093-108.

LERNER, T. R., QUEVAL, C. J., FEARNS, A., REPNIK, U., GRIFFITHS, G. & GUTIERREZ, M. G. 2018. Phthiocerol dimycocerosates promote access to the cytosol and intracellular burden of Mycobacterium tuberculosis in lymphatic endothelial cells. *BMC Biol,* 16**,** 1.

LERNER, T. R., QUEVAL, C. J., LAI, R. P., RUSSELL, M. R., FEARNS, A., GREENWOOD, D. J., COLLINSON, L., WILKINSON, R. J. & GUTIERREZ, M. G. 2020. Mycobacterium tuberculosis cords within lymphatic endothelial cells to evade host immunity. *JCI Insight,* 5.

LIU, H., SHAO, W., LIU, W., SHANG, W., LIU, J. P., WANG, L. & TONG, C. 2023. PtdIns4p exchange at endoplasmic reticulum-autolysosome contacts is essential for autophagy and neuronal homeostasis. *Autophagy***,** 1-20.

LÓPEZ-JIMÉNEZ, A. T., CARDENAL-MUÑOZ, E., LEUBA, F., GERSTENMAIER, L., BARISCH, C., HAGEDORN, M., KING, J. S. & SOLDATI, T. 2018. The ESCRT and autophagy machineries cooperate to repair ESX-1-dependent damage at the Mycobacterium-containing vacuole but have opposite impact on containing the infection. *PLoS Pathog,* 14**,** e1007501.

LÓPEZ-JIMÉNEZ, A. T. & MOSTOWY, S. 2021. Emerging technologies and infection models in cellular microbiology. *Nat Commun,* 12**,** 6764.

MALINOVSKA, L., PALM, S., GIBSON, K., VERBAVATZ, J. M. & ALBERTI, S. 2015. Dictyostelium discoideum has a highly Q/N-rich proteome and shows an unusual resilience to protein aggregation. *Proc Natl Acad Sci U S A,* 112**,** E2620-9.

MARCELIĆ, M., MAHMUTEFENDIĆ LUČIN, H., JURAK BEGONJA, A., BLAGOJEVIĆ ZAGORAC, G. & LUČIN, P. 2022. Early Endosomal Vps34-Derived Phosphatidylinositol-3-Phosphate Is Indispensable for the Biogenesis of the Endosomal Recycling Compartment. *Cells,* 11.

MEKONNEN, D., DERBIE, A., MIHRET, A., YIMER, S. A., TØNJUM, T., GELAW, B., NIBRET, E., MUNSHAE, A., WADDELL, S. J. & ASEFFA, A. 2021. Lipid droplets and the transcriptome of Mycobacterium tuberculosis from direct sputa: a literature review. *Lipids Health Dis,* 20**,** 129.

MESMIN, B., BIGAY, J., MOSER VON FILSECK, J., LACAS-GERVAIS, S., DRIN, G. & ANTONNY, B. 2013. A four-step cycle driven by PI(4)P hydrolysis directs sterol/PI(4)P exchange by the ER-Golgi tether OSBP. *Cell,* 155**,** 830-43.

MESMIN, B., BIGAY, J., POLIDORI, J., JAMECNA, D., LACAS-GERVAIS, S. & ANTONNY, B. 2017. Sterol transfer, PI4P consumption, and control of membrane lipid order by endogenous OSBP. *Embo j,* 36**,** 3156-3174.

MITTAL, E., SKOWYRA, M. L., UWASE, G., TINAZTEPE, E., MEHRA, A., KÖSTER, S., HANSON, P. I. & PHILIPS, J. A. 2018. Mycobacterium tuberculosis Type VII Secretion System Effectors Differentially Impact the ESCRT Endomembrane Damage Response. *mBio,* 9.

MONNAT, J., HACKER, U., GEISSLER, H., RAUCHENBERGER, R., NEUHAUS, E. M., MANIAK, M. & SOLDATI, T. 1997. Dictyostelium discoideum protein disulfide isomerase, an endoplasmic reticulum resident enzyme lacking a KDEL-type retrieval signal. FEBS Lett, 418, 357-62.

MOSER VON FILSECK, J., VANNI, S., MESMIN, B., ANTONNY, B. & DRIN, G. 2015. A phosphatidylinositol-4-phosphate powered exchange mechanism to create a lipid gradient between membranes. *Nat Commun,* 6**,** 6671.

MUKAI, A., ICHIRAKU, A. & HORIKAWA, K. 2016. Reliable handling of highly A/T-rich genomic DNA for efficient generation of knockin strains of Dictyostelium discoideum. *BMC Biotechnol,* 16**,** 37.

MYRVIK, Q. N., LEAKE, E. S. & WRIGHT, M. J. 1984. Disruption of phagosomal membranes of normal alveolar macrophages by the H37Rv strain of Mycobacterium tuberculosis. A correlate of virulence. *Am Rev Respir Dis,* 129**,** 322-8.

NAKATSU, F. & KAWASAKI, A. 2021. Functions of Oxysterol-Binding Proteins at Membrane Contact Sites and Their Control by Phosphoinositide Metabolism. *Front Cell Dev Biol,* 9**,** 664788.

NGUYEN, J. A. & YATES, R. M. 2021. Better Together: Current Insights Into Phagosome-Lysosome Fusion. *Front Immunol,* 12**,** 636078.

NIEKAMP, P., SCHARTE, F., SOKOYA, T., VITTADELLO, L., KIM, Y., DENG, Y., SÜDHOFF, E., HILDERINK, A., IMLAU, M., CLARKE, C. J., HENSEL, M., BURD, C. G. & HOLTHUIS, J. C. M. 2022. Ca(2+)-activated sphingomyelin scrambling and turnover mediate ESCRT-independent lysosomal repair. *Nat Commun,* 13**,** 1875.

OLKKONEN, V. M. 2015. OSBP-Related Protein Family in Lipid Transport Over Membrane Contact Sites. *Lipid Insights,* 8**,** 1-9.

OSMAN, M. M., PAGÁN, A. J., SHANAHAN, J. K. & RAMAKRISHNAN, L. 2020. Mycobacterium marinum phthiocerol dimycocerosates enhance macrophage phagosomal permeabilization and membrane damage. *PLoS One,* 15**,** e0233252.

OSMAN, M. M., SHANAHAN, J. K., CHU, F., TAKAKI, K. K., PINCKERT, M. L., PAGÁN, A. J., BROSCH, R., CONRAD, W. H. & RAMAKRISHNAN, L. 2022. The C terminus of the mycobacterium ESX-1 secretion system substrate ESAT-6 is required for phagosomal membrane damage and virulence. *Proc Natl Acad Sci U S A,* 119**,** e2122161119.

PANDEY, A. K. & SASSETTI, C. M. 2008. Mycobacterial persistence requires the utilization of host cholesterol. *Proc Natl Acad Sci U S A,* 105**,** 4376-80.

PANG, K. M., LEE, E. & KNECHT, D. A. 1998. Use of a fusion protein between GFP and an actin-binding domain to visualize transient filamentous-actin structures. *Curr Biol,* 8**,** 405-8.

PASCHKE, P., KNECHT, D. A., SILALE, A., TRAYNOR, D., WILLIAMS, T. D., THOMASON, P. A., INSALL, R. H., CHUBB, J. R., KAY, R. R. & VELTMAN, D. M. 2018. Rapid and efficient genetic engineering of both wild type and axenic strains of Dictyostelium discoideum. *PLoS One,* 13**,** e0196809.

PASCHKE, P., KNECHT, D. A., WILLIAMS, T. D., THOMASON, P. A., INSALL, R. H., CHUBB, J. R., KAY, R. R. & VELTMAN, D. M. 2019. Genetic Engineering of Dictyostelium discoideum Cells Based on Selection and Growth on Bacteria. *J Vis Exp*.

PAUWELS, A. M., TROST, M., BEYAERT, R. & HOFFMANN, E. 2017. Patterns, Receptors, and Signals: Regulation of Phagosome Maturation. *Trends Immunol,* 38**,** 407-422.

PEYRON, P., VAUBOURGEIX, J., POQUET, Y., LEVILLAIN, F., BOTANCH, C., BARDOU, F., DAFFÉ, M., EMILE, J. F., MARCHOU, B., CARDONA, P. J., DE CHASTELLIER, C. & ALTARE, F. 2008. Foamy macrophages from tuberculous patients' granulomas constitute a nutrient-rich reservoir for M. tuberculosis persistence. *PLoS Pathog,* 4**,** e1000204.

PFITZNER, A. K., MERCIER, V., JIANG, X., MOSER VON FILSECK, J., BAUM, B., ŠARIĆ, A. & ROUX, A. 2020. An ESCRT-III Polymerization Sequence Drives Membrane Deformation and Fission. *Cell,* 182**,** 1140-1155.e18.

QUIGLEY, J., HUGHITT, V. K., VELIKOVSKY, C. A., MARIUZZA, R. A., EL-SAYED, N. M. & BRIKEN, V. 2017. The Cell Wall Lipid PDIM Contributes to Phagosomal Escape and Host Cell Exit of Mycobacterium tuberculosis. *mBio,* 8.

RADULOVIC, M., SCHINK, K. O., WENZEL, E. M., NÄHSE, V., BONGIOVANNI, A., LAFONT, F. & STENMARK, H. 2018. ESCRT-mediated lysosome repair precedes lysophagy and promotes cell survival. Embo j, 37.

RADULOVIC, M., WENZEL, E. M., GILANI, S., HOLLAND, L. K., LYSTAD, A. H., PHUYAL, S., OLKKONEN, V. M., BRECH, A., JÄÄTTELÄ, M., MAEDA, K., RAIBORG, C. & STENMARK, H. 2022. Cholesterol transfer via endoplasmic reticulum contacts mediates lysosome damage repair. *Embo j,* 41**,** e112677.

RAVICHANDRAN, K. S. & LORENZ, U. 2007. Engulfment of apoptotic cells: signals for a good meal. *Nat Rev Immunol,* 7**,** 964-74.

RAYCHAUDHURI, S. & PRINZ, W. A. 2010. The diverse functions of oxysterol-binding proteins. *Annu Rev Cell Dev Biol,* 26**,** 157-77.

RENSHAW, P. S., LIGHTBODY, K. L., VEVERKA, V., MUSKETT, F. W., KELLY, G., FRENKIEL, T. A., GORDON, S. V., HEWINSON, R. G., BURKE, B., NORMAN, J., WILLIAMSON, R. A. & CARR, M. D. 2005. Structure and function of the complex formed by the tuberculosis virulence factors CFP-10 and ESAT-6. *Embo j,* 24**,** 2491-8.

RIZZUTO, R., PINTON, P., CARRINGTON, W., FAY, F. S., FOGARTY, K. E., LIFSHITZ, L. M., TUFT, R. A. & POZZAN, T. 1998. Close contacts with the endoplasmic reticulum as determinants of mitochondrial Ca2+ responses. *Science,* 280**,** 1763-6.

ROBERTS, E. A., CHUA, J., KYEI, G. B. & DERETIC, V. 2006. Higher order Rab programming in phagolysosome biogenesis. *J Cell Biol,* 174**,** 923-9.

RÖDER, J., FELGNER, P. & HENSEL, M. 2021. Comprehensive Single Cell Analyses of the Nutritional Environment of Intracellular Salmonella enterica. *Front Cell Infect Microbiol,* 11**,** 624650.

RUSSELL, M. R., LERNER, T. R., BURDEN, J. J., NKWE, D. O., PELCHEN-MATTHEWS, A., DOMART, M. C., DURGAN, J., WESTON, A., JONES, M. L., PEDDIE, C. J., CARZANIGA, R., FLOREY, O., MARSH, M., GUTIERREZ, M. G. & COLLINSON, L. M. 2017. 3D correlative light and electron microscopy of cultured cells using serial blockface scanning electron microscopy. *J Cell Sci,* 130**,** 278-291.

SAHARAN, O. & KAMAT, S. S. 2023. Mapping lipid pathways during phagocytosis. *Biochem Soc Trans,* 51**,** 1279-1287.

SAINI, N. K., BAENA, A., NG, T. W., VENKATASWAMY, M. M., KENNEDY, S. C., KUNNATH-VELAYUDHAN, S., CARREÑO, L. J., XU, J., CHAN, J., LARSEN, M. H., JACOBS, W. R., JR. & PORCELLI, S. A. 2016. Suppression of autophagy and antigen presentation by Mycobacterium tuberculosis PE_PGRS47. *Nat Microbiol,* 1**,** 16133.

SCHLAM, D., BAGSHAW, R. D., FREEMAN, S. A., COLLINS, R. F., PAWSON, T., FAIRN, G. D. & GRINSTEIN, S. 2015. Phosphoinositide 3-kinase enables phagocytosis of large particles by terminating actin assembly through Rac/Cdc42 GTPase-activating proteins. *Nat Commun,* 6**,** 8623.

SCHNETTGER, L., RODGERS, A., REPNIK, U., LAI, R. P., PEI, G., VERDOES, M., WILKINSON, R. J., YOUNG, D. B. & GUTIERREZ, M. G. 2017. A Rab20-Dependent Membrane Trafficking Pathway Controls M. tuberculosis Replication by Regulating Phagosome Spaciousness and Integrity. *Cell Host Microbe,* 21**,** 619-628.e5.

SCHULER, B., SLADEK, M. & GILK, S. D. 2023. Host Lipid Transport Protein ORP1 Is Necessary for Coxiella burnetii Growth and Vacuole Expansion in Macrophages. *mSphere***,** e0010423.

SCHULTE, M., OLSCHEWSKI, K. & HENSEL, M. 2021. Fluorescent protein-based reporters reveal stress response of intracellular Salmonella enterica at level of single bacterial cells. *Cell Microbiol,* 23**,** e13293.

SCHULZ, T. A., CHOI, M. G., RAYCHAUDHURI, S., MEARS, J. A., GHIRLANDO, R., HINSHAW, J. E. & PRINZ, W. A. 2009. Lipid-regulated sterol transfer between closely apposed membranes by oxysterol-binding protein homologues. *J Cell Biol,* 187**,** 889-903.

SCORRANO, L., DE MATTEIS, M. A., EMR, S., GIORDANO, F., HAJNÓCZKY, G., KORNMANN, B., LACKNER, L. L., LEVINE, T. P., PELLEGRINI, L., REINISCH, K., RIZZUTO, R., SIMMEN, T., STENMARK, H., UNGERMANN, C. & SCHULDINER, M. 2019. Coming together to define membrane contact sites. *Nat Commun,* 10**,** 1287.

SERAFINI, A., BOLDRIN, F., PALÙ, G. & MANGANELLI, R. 2009. Characterization of a Mycobacterium tuberculosis ESX-3 conditional mutant: essentiality and rescue by iron and zinc. *J Bacteriol,* 191**,** 6340-4.

SERAFINI, A., PISU, D., PALÙ, G., RODRIGUEZ, G. M. & MANGANELLI, R. 2013. The ESX-3 secretion system is necessary for iron and zinc homeostasis in Mycobacterium tuberculosis. *PLoS One,* 8**,** e78351.

SIEGRIST, M. S., STEIGEDAL, M., AHMAD, R., MEHRA, A., DRAGSET, M. S., SCHUSTER, B. M., PHILIPS, J. A., CARR, S. A. & RUBIN, E. J. 2014. Mycobacterial Esx-3 requires multiple components for iron acquisition. *mBio,* 5**,** e01073-14.

SIMEONE, R., BOBARD, A., LIPPMANN, J., BITTER, W., MAJLESSI, L., BROSCH, R. & ENNINGA, J. 2012. Phagosomal rupture by Mycobacterium tuberculosis results in toxicity and host cell death. *PLoS Pathog,* 8**,** e1002507.

SIMEONE, R., SAYES, F., SONG, O., GRÖSCHEL, M. I., BRODIN, P., BROSCH, R. & MAJLESSI, L. 2015. Cytosolic access of Mycobacterium tuberculosis: critical impact of phagosomal acidification control and demonstration of occurrence in vivo. *PLoS Pathog,* 11**,** e1004650.

SINGH, V., JAMWAL, S., JAIN, R., VERMA, P., GOKHALE, R. & RAO, K. V. 2012. Mycobacterium tuberculosis-driven targeted recalibration of macrophage lipid homeostasis promotes the foamy phenotype. *Cell Host Microbe,* 12**,** 669-81.

SOHN, M., KORZENIOWSKI, M., ZEWE, J. P., WILLS, R. C., HAMMOND, G. R. V., HUMPOLICKOVA, J., VRZAL, L., CHALUPSKA, D., VEVERKA, V., FAIRN, G. D., BOURA, E. & BALLA, T. 2018. PI(4,5)P(2) controls plasma membrane PI4P and PS levels via ORP5/8 recruitment to ER-PM contact sites. *J Cell Biol,* 217**,** 1797-1813.

SOLOMON, J. M., LEUNG, G. S. & ISBERG, R. R. 2003. Intracellular replication of Mycobacterium marinum within Dictyostelium discoideum: efficient replication in the absence of host coronin. *Infect Immun,* 71**,** 3578-86.

SØRENSEN, A. L., NAGAI, S., HOUEN, G., ANDERSEN, P. & ANDERSEN, A. B. 1995. Purification and characterization of a low-molecular-mass T-cell antigen secreted by Mycobacterium tuberculosis. *Infect Immun,* 63**,** 1710-7.

SPIEGELHALTER, C., TOSCH, V., HENTSCH, D., KOCH, M., KESSLER, P., SCHWAB, Y. & LAPORTE, J. 2010. From dynamic live cell imaging to 3D ultrastructure: novel integrated methods for high pressure freezing and correlative light-electron microscopy. *PLoS One,* 5**,** e9014.

SRINIVASAN, L., GURSES, S. A., HURLEY, B. E., MILLER, J. L., KARAKOUSIS, P. C. & BRIKEN, V. 2016. Identification of a Transcription Factor That Regulates Host Cell Exit and Virulence of Mycobacterium tuberculosis. *PLoS Pathog,* 12**,** e1005652.

STEINER, B., SWART, A. L., WELIN, A., WEBER, S., PERSONNIC, N., KAECH, A., FREYRE, C., ZIEGLER, U., KLEMM, R. W. & HILBI, H. 2017. ER remodeling by the large GTPase atlastin promotes vacuolar growth of Legionella pneumophila. *EMBO Rep,* 18**,** 1817-1836.

STEINERT, M. 2011. Pathogen-host interactions in Dictyostelium, Legionella, Mycobacterium and other pathogens. *Semin Cell Dev Biol,* 22**,** 70-6.

STINEAR, T. P., SEEMANN, T., HARRISON, P. F., JENKIN, G. A., DAVIES, J. K., JOHNSON, P. D., ABDELLAH, Z., ARROWSMITH, C., CHILLINGWORTH, T., CHURCHER, C., CLARKE, K., CRONIN, A., DAVIS, P., GOODHEAD, I., HOLROYD, N., JAGELS, K., LORD, A., MOULE, S., MUNGALL, K., NORBERTCZAK, H., QUAIL, M. A., RABBINOWITSCH, E., WALKER, D., WHITE, B., WHITEHEAD, S., SMALL, P. L., BROSCH, R., RAMAKRISHNAN, L., FISCHBACH, M. A., PARKHILL, J. & COLE, S. T. 2008. Insights from the complete genome sequence of Mycobacterium marinum on the evolution of Mycobacterium tuberculosis. *Genome Res,* 18**,** 729-41.

STRONG, E. J., JURCIC SMITH, K. L., SAINI, N. K., NG, T. W., PORCELLI, S. A. & LEE, S. 2020. Identification of Autophagy-Inhibiting Factors of Mycobacterium tuberculosis by High-Throughput Loss-of-Function Screening. *Infect Immun,* 88.

STRUCKMAN, H. L., MOISE, N., VANSLEMBROUCK, B., ROTHACKER, N., CHEN, Z., HENGEL, J. V., WEINBERG, S. H. & VEERARAGHAVAN, R. 2023. Indirect Correlative Light and Electron Microscopy (iCLEM): A Novel Pipeline for Multiscale Quantification of Structure from Molecules to Organs. *bioRxiv,* 2023.05.15.540853.

SUN, J., SIROY, A., LOKAREDDY, R. K., SPEER, A., DOORNBOS, K. S., CINGOLANI, G. & NIEDERWEIS, M. 2015. The tuberculosis necrotizing toxin kills macrophages by hydrolyzing NAD. *Nat Struct Mol Biol,* 22**,** 672-8.

TÁBARA, L. C. & ESCALANTE, R. 2016. VMP1 Establishes ER-Microdomains that Regulate Membrane Contact Sites and Autophagy. *PLoS One,* 11**,** e0166499.

TAKAKI, K., DAVIS, J. M., WINGLEE, K. & RAMAKRISHNAN, L. 2013. Evaluation of the pathogenesis and treatment of Mycobacterium marinum infection in zebrafish. *Nat Protoc,* 8**,** 1114-24.

TAN, J. X. & FINKEL, T. 2022. A phosphoinositide signalling pathway mediates rapid lysosomal repair. *Nature,* 609**,** 815-821.

THIELE, D. L. & LIPSKY, P. E. 1990a. The action of leucyl-leucine methyl ester on cytotoxic lymphocytes requires uptake by a novel dipeptide-specific facilitated transport system and dipeptidyl peptidase I-mediated conversion to membranolytic products. *J Exp Med,* 172**,** 183-94.

THIELE, D. L. & LIPSKY, P. E. 1990b. Mechanism of L-leucyl-L-leucine methyl ester-mediated killing of cytotoxic lymphocytes: dependence on a lysosomal thiol protease, dipeptidyl peptidase I, that is enriched in these cells. *Proc Natl Acad Sci U S A,* 87**,** 83-7.

URIBE-QUEROL, E. & ROSALES, C. 2017. Control of Phagocytosis by Microbial Pathogens. *Front Immunol,* 8**,** 1368.

VAN DER WEL, N., HAVA, D., HOUBEN, D., FLUITSMA, D., VAN ZON, M., PIERSON, J., BRENNER, M. & PETERS, P. J. 2007. M. tuberculosis and M. leprae translocate from the phagolysosome to the cytosol in myeloid cells. *Cell,* 129**,** 1287-98.

VAUGHN, B. & ABU KWAIK, Y. 2021. Idiosyncratic Biogenesis of Intracellular Pathogens-Containing Vacuoles. *Frontiers in Cellular and Infection Microbiology,* 11.

VELTMAN, D. M., AKAR, G., BOSGRAAF, L. & VAN HAASTERT, P. J. 2009a. A new set of small, extrachromosomal expression vectors for Dictyostelium discoideum. *Plasmid,* 61**,** 110-8.

VELTMAN, D. M., KEIZER-GUNNINK, I. & HAASTERT, P. J. 2009b. An extrachromosomal, inducible expression system for Dictyostelium discoideum. *Plasmid,* 61**,** 119-25.

VERGNE, I., CHUA, J., LEE, H. H., LUCAS, M., BELISLE, J. & DERETIC, V. 2005. Mechanism of phagolysosome biogenesis block by viable Mycobacterium tuberculosis. *Proc Natl Acad Sci U S A,* 102**,** 4033-8.

VERGNE, I., FRATTI, R. A., HILL, P. J., CHUA, J., BELISLE, J. & DERETIC, V. 2004. Mycobacterium tuberculosis phagosome maturation arrest: mycobacterial phosphatidylinositol analog phosphatidylinositol mannoside stimulates early endosomal fusion. *Mol Biol Cell,* 15**,** 751-60.

VIETRI, M., RADULOVIC, M. & STENMARK, H. 2020. The many functions of ESCRTs. *Nat Rev Mol Cell Biol,* 21**,** 25-42.

VINES, J. H., MAIB, H., BUCKLEY, C. M., GUEHO, A., ZHU, Z., SOLDATI, T., MURRAY, D. H. & KING, J. S. 2023. A PI(3,5)P2 reporter reveals PIKfyve activity and dynamics on macropinosomes and phagosomes. *J Cell Biol,* 222.

VORMITTAG, S., HÜSLER, D., HANEBURGER, I., KRONIGER, T., ANAND, A., PRANTL, M., BARISCH, C., MAAß, S., BECHER, D., LETOURNEUR, F. & HILBI, H. 2023. Legionella- and host-driven lipid flux at LCV-ER membrane contact sites promotes vacuole remodeling. *EMBO Rep,* 24**,** e56007.

WANG, Y. J., WANG, J., SUN, H. Q., MARTINEZ, M., SUN, Y. X., MACIA, E., KIRCHHAUSEN, T., ALBANESI, J. P., ROTH, M. G. & YIN, H. L. 2003. Phosphatidylinositol 4 phosphate regulates targeting of clathrin adaptor AP-1 complexes to the Golgi. *Cell,* 114**,** 299-310.

WASSIE, A. T., ZHAO, Y. & BOYDEN, E. S. 2019. Expansion microscopy: principles and uses in biological research. *Nat Methods,* 16**,** 33-41.

WATTS, D. J. & ASHWORTH, J. M. 1970. Growth of myxameobae of the cellular slime mould Dictyostelium discoideum in axenic culture. *Biochem J,* 119**,** 171-4.

WEBER-BOYVAT, M., KENTALA, H., PERÄNEN, J. & OLKKONEN, V. M. 2015. Ligand-dependent localization and function of ORP-VAP complexes at membrane contact sites. *Cell Mol Life Sci,* 72**,** 1967-87.

WEBER, S., WAGNER, M. & HILBI, H. 2014. Live-cell imaging of phosphoinositide dynamics and membrane architecture during Legionella infection. *mBio,* 5**,** e00839-13.

WELIN, A., WEBER, S. & HILBI, H. 2018. Quantitative Imaging Flow Cytometry of Legionella-Infected Dictyostelium Amoebae Reveals the Impact of Retrograde Trafficking on Pathogen Vacuole Composition. *Appl Environ Microbiol,* 84.

WIEGAND, S., KRUSE, J., GRONEMANN, S. & HAMMANN, C. 2011. Efficient generation of gene knockout plasmids for Dictyostelium discoideum using one-step cloning. *Genomics,* 97**,** 321-5.

WILHELM, L. P., WENDLING, C., VÉDIE, B., KOBAYASHI, T., CHENARD, M. P., TOMASETTO, C., DRIN, G. & ALPY, F. 2017. STARD3 mediates endoplasmic reticulum-to-endosome cholesterol transport at membrane contact sites. *Embo j,* 36**,** 1412-1433.

WONG, D., BACH, H., SUN, J., HMAMA, Z. & AV-GAY, Y. 2011. Mycobacterium tuberculosis protein tyrosine phosphatase (PtpA) excludes host vacuolar-H+-ATPase to inhibit phagosome acidification. *Proc Natl Acad Sci U S A,* 108**,** 19371-6.

WU, Y., WHITEUS, C., XU, C. S., HAYWORTH, K. J., WEINBERG, R. J., HESS, H. F. & DE CAMILLI, P. 2017. Contacts between the endoplasmic reticulum and other membranes in neurons. *Proc Natl Acad Sci U S A,* 114**,** E4859-e4867.

ZENG, J., ACIN-PEREZ, R., ASSALI, E. A., MARTIN, A., BROWNSTEIN, A. J., PETCHERSKI, A., FERNÁNDEZ-DEL-RIO, L., XIAO, R., LO, C. H., SHUM, M., LIESA, M., HAN, X., SHIRIHAI, O. S. & GRINSTAFF, M. W. 2023. Restoration of lysosomal acidification rescues autophagy and metabolic dysfunction in non-alcoholic fatty liver disease. *Nat Commun,* 14**,** 2573.

8. STATEMENT OF AUTHORSHIP

Erklärung über die Eigenständigkeit der erbrachten wissenschaftlichen Leistung

Ich erkläre hiermit, dass ich die vorliegende Arbeit ohne unzulässige Hilfe Dritter und ohne Benutzung anderer als der angegebenen Hilfsmittel angefertigt habe. Die aus anderen Quellen direkt oder indirekt übernommenen Daten und Konzepte sind unter Angabe der Quelle gekennzeichnet. Alle beteiligten Personen sind unter Angabe ihres Beitrages aufgeführt.

Weitere Personen waren an der inhaltlichen materiellen Erstellung der vorliegenden Arbeit nicht beteiligt. Insbesondere habe ich hierfür nicht die entgeltliche Hilfe von Vermittlungs- bzw. Beratungsdiensten (Promotionsberater oder andere Personen) in Anspruch genommen. Niemand hat von mir unmittelbar oder mittelbar geldwerte Leistungen für Arbeiten erhalten, die im Zusammenhang mit dem Inhalt der vorgelegten Dissertation stehen, Die Arbeit wurde bisher weder im In- noch Ausland in gleicher oder ähnlicher Form einer anderen Prüfungsbehörde vorgelegt.

_____

(Ort, Datum)   (Unterschrift)

9. ACKNOWLEDGMENTS